Ground-based remote sensing of Antarctic and Alpine solid precipitation

Claudio Durán Alárcon

Communauté
UNIVERSITÉ Grenoble Alpes

THÈSE

Pour obtenir le grade de

DOCTEUR DE L'UNIVERSITÉ DE GRENOBLE

Spécialité : **Sciences de la Terre, de l'Univers, et de l'Environnement**

Arrêté ministériel du 25 mai 2016

Présentée par

Claudio Durán-Alarcón

Thèse dirigée par **Brice Boudevillain** et **Alexis Berne**

préparée au sein du **Institut des Géosciences de l'Environnement (IGE)**
et de l'École Doctorale **Terre Univers Environnement (TUE)**

Ground-based remote sensing of Antarctic and Alpine solid precipitation

Thèse soutenue publiquement le **23 octobre 2019**,
devant le jury composé de :

Julien Delanoë
Maître de Conférences à l'Université de Versailles-Saint-Quentin, LATMOS, Rapporteur

Joël Van Baelen
Directeur de Recherche CNRS, Laboratoire de l'Atmosphère et des Cyclones (LACy), Saint-Denis (La Réunion), Rapporteur

Marielle Gosset
Chargée de Recherche IRD, Géosciences Environnement Toulouse (GET), Toulouse, Examinatrice

Remko Uijlenhoet
Professeur à l'Université de Wageningen, Pays-Bas, Examinateur

Christophe Genthon
Directeur de Recherche CNRS, Laboratoire de Météorologie Dynamique (LMD), Paris, Invité

Guy Delrieu
Directeur de Recherche CNRS, IGE, Grenoble, Président

Brice Boudevillain
Physicien-adjoint CNAP à l'Université Grenoble Alpes, IGE, Grenoble, Directeur de thèse

Alexis Berne
Professeur Associé à l'Ecole Polytechnique Fédérale de Lausanne (EPFL), Suisse, Co-Directeur de thèse

Abstract

Solid precipitation plays an important role in the Earth's climate system, as well as for the maintenance of ecosystems and the development of human society. The large uncertainty in precipitation estimates and the discrepancies within climate model projections make this component of the hydrological cycle important as a research topic. Satellite remote sensing allows to monitor precipitation and clouds in regions where in-situ observations are scarce and scattered, but with limited temporal resolution and a blind zone close to the ground level for spaceborne sensors, and limited visibility in the lower atmosphere in complex terrain for ground-based radars. The objectives of this dissertation are the following: 1) to characterize cloud and precipitation in Antarctica, detecting the presence of supercooled liquid and ice particles near the ground level using a ground-based 532-nm depolarization lidar; 2) to characterize the vertical structure of the precipitation in two contrasted but important regions of the cryosphere, Antarctica and the Alps, in the low troposphere using ground-based radars.

In this study, a cloud and precipitation hydrometeor detection method is proposed using lidar data, complemented with a K-band micro rain radar (MRR) to improve the detection of precipitation, both instruments deployed at the Dumont d'Urville (DDU) station in East Antarctica. A method based on lidar depolarization and attenuated backscattering coefficient and the use of k-means clustering is developed for the particle classification. The classification of cloud and precipitation particles provides the vertical distribution of supercooled liquid water, as well as planar oriented ice and randomly oriented ice particles. The comparison between ground-based and satellite-derived classifications shows consistent patterns for the vertical distribution of supercooled liquid water in clouds.

The vertical structure of precipitation near the surface is analyzed using the Doppler moments derived from three MRR profiles at DDU, the Princess Elisabeth (PE) station, at the interior of East Antarctica, and at the Col de Porte (CDP) station, in the French Alps. These analyses demonstrate that local climate plays an important role in the vertical structure of the precipitation. In Antarctica, the strong katabatic winds blowing from the high plateau down to the coast decrease the radar reflectivity factor near the surface due to the sublimation of the snowfall particles. Doppler moments also provide rich information to understand precipitation processes, such as aggregation and riming, as observed at DDU and CDP.

The results also show that in the interior of the Antarctic continent a significant part (47%) of the precipitation profiles completely sublimate before reaching the surface, due to the dry atmospheric conditions, while in the coast of Antarctica it corresponds to about the third part (36%). In the Alps, this percentage is reduced to 15%. The major occurrence of particle sublimation is observed below the altitude where CloudSat profiles are contaminated by ground clutter. Therefore, this phenomenon cannot be fully captured from space with the current generation of sensors.

This dissertation contributes to the study of the vertical structure of snowfall in the low troposphere, useful for the evaluation of precipitation remote sensing products, which may have severe limitations in the vicinity of the surface.

Résumé

Les précipitations solides jouent un rôle crucial dans le système climatique terrestre, ainsi que dans le maintien des écosystèmes et le développement des activités humaines. Les incertitudes associées aux estimations quantitatives des précipitations ainsi que celles concernant les projections des modèles climatiques font de cette composante du cycle hydrologique un sujet de recherche important. La télédétection permet de suivre les précipitations et les nuages dans des régions où les observations in situ sont rares et dispersées, mais avec une résolution temporelle limitée ainsi qu'une zone aveugle près du sol pour les capteurs spatiaux, et une visibilité limitée dans la basse atmosphère en terrain complexe pour les radars au sol. Les objectifs de cette thèse sont les suivants : 1) caractériser les nuages et les précipitations en Antarctique, en détectant la présence d'eau liquide surfondue et de particules de glace près du sol à l'aide d'un lidar 532-nm, polarisé, au sol ; 2) caractériser la structure verticale des précipitations dans deux régions contrastées mais importantes de la cryosphère, l'Antarctique et les Alpes, dans la basse troposphère, en utilisant des radars au sol.

Dans cette étude, une méthode de détection des hydrométéores dans les nuages et les précipitations est proposée à l'aide de données lidar complétées par celles d'un *micro rain radar* (MRR) en bande K pour améliorer la détection des précipitations, ces deux instruments étant déployés à la station Dumont d'Urville (DDU) en Antarctique de l'Est. Une méthode fondée sur le facteur de dépolarisation lidar, le coefficient de rétrodiffusion atténué et l'utilisation d'un partitionnement en k-moyennes est développée. La classification des particules des nuages et des précipitations permet de documenter la distribution verticale de l'eau liquide surfondue, ainsi que des particules de glace sous différentes formes. La comparaison entre les classifications obtenues depuis le sol et celles obtenues à partir des données satellitaires montre des formes similaires pour la distribution verticale de l'eau liquide surfondue dans les nuages.

La structure verticale des précipitations près de la surface est analysée à l'aide des moments Doppler obtenus à partir de trois MRRs situés à DDU, à la station Princess Elisabeth à l'intérieur de l'Antarctique de l'Est, et à la station du Col de Porte dans les Alpes françaises. Ces analyses montrent que le climat local joue un rôle important dans la structure verticale des précipitations. En Antarctique, les forts vents catabatiques soufflant du haut plateau jusqu'à la côte diminuent le facteur de réflectivité radar près de la surface en raison de la sublimation des flocons de neige. Les moments Doppler fournissent aussi de riches informations pour comprendre les processus liés aux précipitations, tels que l'agrégation et le givrage, observés notamment à DDU et au Col de Porte.

Les résultats montrent également qu'à l'intérieur du continent Antarctique, une partie significative (47%) des profils de précipitations présentent une sublimation complète avant la surface en raison des conditions atmosphériques sèches, alors que sur la côte de l'Antarctique, cela ne concerne qu'environ un tiers des profils (36%). Dans les Alpes, ce pourcentage est réduit à 15%. La majeure partie de la sublimation est observée en dessous de l'altitude où les profils de CloudSat sont contaminés par la proximité du sol. Par conséquent, ce phénomène ne peut pas être entièrement décelé depuis l'espace avec

les capteurs actuels.

Cette thèse contribue à l'étude de la structure verticale des précipitations neigeuses dans la basse troposphère ; elle est utile pour l'évaluation des produits de télédétection concernant les précipitations qui peuvent présenter de fortes limitations à la proximité de la surface.

Acknowledgments

Many people have contributed with the rocks that support the construction of this doctoral work. I am deeply grateful to all of them, because without their collaboration this outcome would simply not be the same. For logistical reasons, it is difficult for me to mention all their names, but believe me that as I write these words, I remember them along the entire route until this very moment.

I would like to start by thanking my supervisors, Brice Boudevillain and Alexis Berne, for all the support they have given me throughout this thesis work. They have not only provided a significant guidance and great examples as researchers, but also they always create a nice atmosphere that made every moment we shared very enjoyable.

I would like to thank Christophe Genthon, for all the support and motivation. For the wonderful time we spent during the mission in Antarctica. His original interest in the investigation of precipitation in the great white continent is the basis on which this project is sustained.

Thanks so much for the interesting and useful question and comments that the Rapporteurs Julien Delanoë and Joël Van Baelen, and the Examinateurs Marielle Gosset and Remko Uijlenhoet provided in the process of evaluation of this PhD work. Thank you very much to Guy Delrieu for all the support, specially in the difficult period of the PhD.

I thank the APRES3 team, with whom we exchanged our interesting results of the project, and also good convivial moments. I also thank to the ANR-APRES3 project for the fully supported this research.

Thank you very much to IGE and their members, who hosted me for this long time, even before I started the PhD, when I worked in my master's internship. A special thanks to the HMCIS team, with whom I shared most of the scientific discussions in the laboratory.

A big thanks to IPEV and their members that make possible the working of the instruments at DDU, Antarctica, especially to Etienne, Gauthier and Mervyn, whom I bothered continuously to check the radar and other instruments. Thank you very much to all Meteo-France members that took care of the snow gauge and disdrometers at DDU.

Thanks to the SPICE-Project for providing the valuable data to study precipitation in the Alpine region. Thank you so much to the support of CNES-EECLAT for

the design of the lidar that we deployed at DDU, providing rich information from clouds and precipitation.

I would like to thank to all the coauthors that contributed with their knowledge and different points of view to improve every single step in the analysis and discussion of the results.

I want to strongly thank my wife, Ninoska Gajardo, because she supports all my crazy ideas and she let me support hers. Thank you for giving meaning to all the decisions we have to take in our lives.

Thanks to my mother, Sara Alarcón, for her strength and endurance. Thank you for being a great example of a person, and forgive me for my long assent. Thanks to my brother, Camilo Durán, for teaching me to be passionate about the ideals, to be firm in our choices.

Thank you very much to Cristian Mattar for inspiring and motivating me to continue on the path of science and to the LAB's Members, Luis Olivera and Andrés Santamaría, for being one of the first firm rocks in this construction. Thank you my friends.

Thank you very much to all my friends in Chile who have always supported me from the distance. I miss you a lot.

Many thanks to the great friends I made during my stay at Grenoble, they have become an extended family for me.

Finally, thank you very much to God, for making the thinks possible and thanks for this interesting and mysterious Universe.

Thank you all.

Claudio Durán-Alarcón

Contents

List of Figures

List of Tables

List of Abbreviations

2C-PRECIP-COLUMN	CloudSat 2C Precipitation Column product
2C-SNOW-PROFILE	CloudSat 2C Snow Profile product
AIS	Antarctic Ice Sheet
APRES3	Antarctic Precipitation Remote Sensing from Surface
CALIOP	Cloud-Aerosol Lidar with Orthogonal Polarization
CALIPSO	Cloud-Aerosol Lidar and Infrared Pathfinder Satellite Observation
CDP	Col de Porte
CFSR	Climate Forecast System Reanalysis
CloudSat	Cloud Satellite
CMIP5	Coupled Model Intercomparison Project Phase 5
CPR	Cloud Profiling Radar
DARDAR	raDAR/liDAR
DDU	Dumont d'Urville
EAIS	East Antarctic Ice Sheet
ECMWF	European Centre for Medium-range Weather Forecasts
ERA Interim	Interim Reanalysis
FFT	Fast Fourier Transform
FMCW	Frequency-modulated continuous-wave
GHG	Green House Gas
GPCP	Global Precipitation Climatology Project
GPM	Global Precipitation Measurement
HF	High Frequency
HYDRANT	HYDRological cycle of ANTarctica
LF	Low Frequency
Lidar	LIght Detection and Ranging
m.a.s.l.	Meters above sea level
MF	Medium Frequency
MRR	Micro Rain Radar
NCEP	National Centers for Environmental Prediction
PE	Princess Elisabeth
Radar	RAdio Detection And Ranging
RCP8.5	Representative Concentration Pathway 8.5
SLW	Supercooled liquid water
SMB	Surface Mass Balance
SPICE-project	Solid Precipitation Intercomparison Experiment
TRMM	Tropical Rainfall Measurement Mission

UHF	Ultra High Frequency
UV	Ultraviolet radiation
VHF	Very High Frequency
WAIS	West Antarctic Ice Sheet
WMO	World Meteorological Organization

Nomenclature

A	Amplitude
A_e	Effective area of the antenna or telescope
c	Speed of the light
C_r	Radar calibration constant
D	Particle diameter
D_R	Antenna size
ϵ_r	Relative permittivity or dielectric constant
ϵ_r''	Imaginary part of the relative permittivity
ϵ_r'	Real part of the relative permittivity
η	Radar reflectivity
G	Antenna gain
K	Dielectric factor
$\|K\|^2$	Square of the absolute value of dielectric factor
κ	Proportionality factor in the equation of ϕ
K_w	Dilectric factor of water
λ	Wavelenght
m	Complex refractive index
$N(D)$	Particle/Drop size distribution
N_s	Number density of molecules at standard conditions
ν	Wave frequency
O	Overlapping function
ϕ	Half power beam-width
P	Power received by the lidar telescope
P_r	Power received by the radar antenna
P_s	Standard Pressure
P_t	Transmitted power
$\overline{P_t}$	Average power from the contibuting region
r	Distance between target and the receiver/transmitter system
RH	Relative humidity
RH_i	Relative humidity with respect to ice
ρ_0	Air density at the surface
ρ_a	Air density
RH_w	Relative humidity with respect to liquid water
S	Snowfall rate
S_i	Power flux density of the wave incident on a target
σ	Radar cross-section

σ_v	Spectral width
$\overline{\sigma}$	Total radar cross-section
S_r	Power flux density of the scattered wave at the receiving antenna
τ	Pulse length
T_s	Standard temperature
V_c	Contributing region or sampling volume
v_r	Radial velocity
$\overline{v}_r$	Averaged radial velocity
V_t	Terminal velocity
W	Mean Doppler velocity
x	Dimensionless size parameter
Z	Radar reflectivity factor
Z_e	Equivalent radar reflectivity factor

General Introduction

Precipitation at high latitudes and altitudes

In a warming climate, precipitation is expected to change not only in terms of duration, frequency and intensity (Trenberth et al., 2003; Stephens and Ellis, 2008; Behrangi et al., 2016), but also in terms of total precipitation amount (Trenberth et al., 2007; Behrangi et al., 2014, 2016). Under a scenario of rising greenhouse gas (GHG) emissions without a mitigation target, with an expected radiative forcing of 8.5 Wm^{-2} by the end of the 21^{st} century (known as the representative concentration pathway 8.5 scenario, RCP8.5) (IPCC, 2007; Riahi et al., 2011; Giorgi et al., 2014), most of the global precipitation model projections of the Coupled Model Intercomparison Project, Phase 5 (CMIP5), show a progressive increase of annual precipitation over the current century, as a consequence of the increase of global surface evaporation due to the warming of the land and sea (Trenberth et al., 2007; Lau et al., 2013; Giorgi et al., 2019). At mid and high latitudes, the general pattern of precipitation is expected to increase significantly due to an increase in the moisture transported from the tropical troposphere to the poles under the RCP8.5 scenario, produced by a poleward shift of the storm track and the expansion of the Hadley cell, which in turn is caused by a maximum warming in the tropical region and a poleward shift in the location of the jet stream (IPCC, 2013; Giorgi et al., 2019).

Despite the general agreement among models on the increase in precipitation, they present a large uncertainty with a number of discrepancies on the regional and seasonal scales (Behrangi et al., 2016). Regarding the representation of the current state of global precipitation in models, large biases are present (Stephens et al., 2010), induced mainly by the large uncertainties in observational precipitation products (Behrangi et al., 2012), especially in high-latitude and mountainous regions, where ground-based observations are scarce with poor spatial coverage (Adler et al., 2012). Moreover, as hydrology in high-altitude (e.g. Alps and Andes mountains

during winter time) and high-latitude (e.g. Antarctica, Arctic) regions is dominated by precipitation in form of snow, the available gauge observations present significant uncertainties, larger than 100% (Yang et al., 2005; Fuchs et al., 2001), due to different factors such as wind-induced under catch (Goodison et al., 1998), miss-detection of light snowfall and the presence of blowing snow events that spoil the measurements. Therefore, the accurate quantification of solid precipitation is key to understand its current state, in terms of amount and spatio/temporal distribution (Trenberth et al., 2007; Stephens et al., 2012; Behrangi et al., 2016), in order to evaluate the impacts on the hydrological cycle of high altitude and latitude regions (Andrews et al., 2009; Ye et al., 2014).

The phase of precipitation is also projected to change due to the increase in temperature, especially in mid-latitude mountainous regions, where a shortening of the period with temperatures below 0 °C is expected, as well as a vertical shift of the limit between solid and liquid precipitation, leading to a reduction in the number of solid precipitation events (Diaz et al., 2003; IPCC, 2013; Wang et al., 2014). In the case of the Alpine regions, during the last decades the proportion between the number of snowfall days to the number of rainfall days has experienced a downward trend connected to increasing temperatures (Hantel and Hirtl-Wielke, 2007; Marty, 2008), with a stronger decrease in the lower elevation areas, close to the freezing level (Scherrer et al., 2004; Serquet et al., 2011). The change from solid to liquid precipitation leads to changes in the distribution of snow cover, mountain glacier areas (IPCC, 2013) and in freshwater discharge (Dyurgerov and Carter, 2006; Beniston and Stoffel, 2016; Würzer et al., 2016), favoring the reduction of the freshwater storage capacity and the increase of risks of winter and spring flooding (Knowles et al., 2001). These changes have serious implications in the regional hydrology, producing severe impacts at the socio-economic level (Fehlmann et al., 2018; Giorgi et al., 2019).

Concerning solid precipitation at high latitudes, Antarctica takes significant relevance. The Antarctic ice sheet is the single largest land water storage in the world (van Wessem et al., 2014, 2018), which may contribute in the long-term to an eustatic sea level change between 60 and 72 m, in the case that all southern polar ice melts (Drewry, 1992). Fortunately, such an extreme scenario is not happening in the near future, in fact IPCC (2013) reported no significant changes on surface melting on the Antarctic ice sheet during the current century, while snowfall is expected to increase, but with a low level of confidence. In general terms, this means that the surface mass balance (SMB, i.e. sum of precipitation, sublimation/evaporation,

melt water, and blowing snow) of Antarctica is expected to increase (Palerme et al., 2017a), but with a strong dependence on the uncertainty associated with precipitation projections. As mentioned before, accurate observations of the current state of the precipitation are fundamental to the evaluation and validation of the current climate models and to determine the best future projections. This represents a great observational challenge in Antarctica, where the stations are scarce and scattered, moreover there is a reduced number of stations equipped with specialized instruments for monitoring precipitation in this region. Antarctica is a continent of difficult access and the environmental conditions are sufficiently hostile to hinder the deployment of long-duration missions, thus, due to the lack of information and the difficulties associated with its collection, there is a long way to go to understand the climatology of precipitation in this remote region of the world.

In the following subsections, more detailed information on precipitation, methods of observation, previous investigations and major challenges in the context of Antarctica and the Alps is provided.

Antarctic context

The Antarctic continent is located south of the 60° S parallel, covering an area equivalent to 10% of the surface of the Earth. The Antarctic ice sheet (AIS) can be divided in three regions, the East Antarctic ice sheet (EAIS), West Antarctic ice sheet (WAIS) and the Antarctic Peninsula (see Figure 1). EAIS is the biggest region and it is dominated by the Antarctic Plateau, which reaches the highest average elevation in the continent, with altitudes higher than 4000 m above sea level and the coldest mean air temperatures in winter below -60 °C (Bromwich and Stearns, 1993; King and Turner, 1997). AIS contains a volume of ice between 24 and 29 million km^3 (Drewry, 1992) and during last decades it has contributed at a rate of 0.27 (0.16-0.38) mm yr^{-1} to the sea level rise, corresponding to ∼10% of the total sea level rise (i.e. sum of the contribution to sea level rise due to thermal expansion of the sea, glacier changes, Greenland ice sheet and other water storages) (IPCC, 2013).

Antarctica is a harsh environment for precipitation monitoring, due to the presence of strong wind in the coastal regions and extremely cold temperature and very limited precipitation amount in the interior, and also to the remoteness and isolation that make operation on site expensive. In this environment, traditional snow gauges provide unreliable measurements (Turner et al., 1998; Genthon et al., 2003; Balsamo

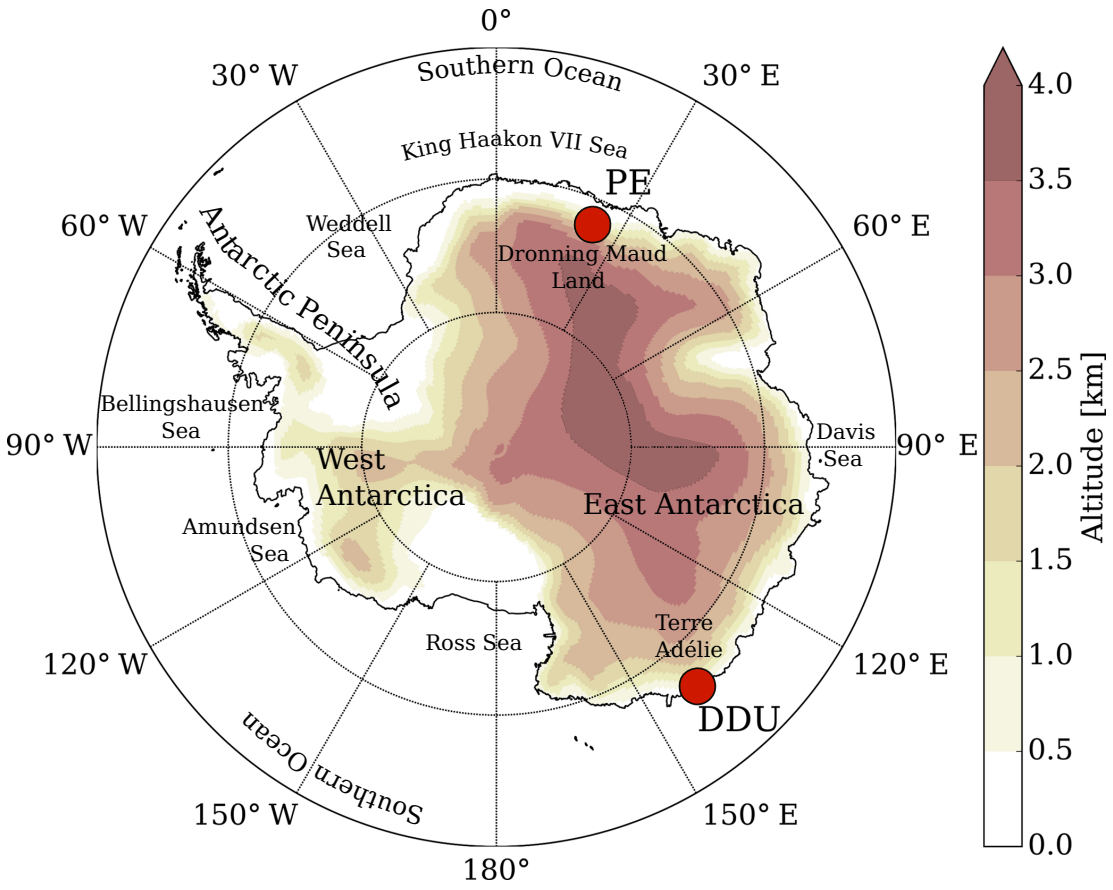

Figure 1: Antarctica overview map. The red dots correspond to the location of Dumont d'Urville (DDU) and Princess Elisabeth (PE) stations.

et al., 2015), hence the most commonly used monitoring methods have been carried out in an indirect way, such as snow pits and ice cores to estimate accumulation, which provided the first approaches to obtain SMB maps in most of the Antarctic region (Vaughan et al., 1999). Although these local observations provide valuable information, they are strongly affected by the wind-borne snow redistribution, due to the high frequency of moderate (e.g. Antarctic Plateau) to strong (e.g. Antarctic coast) winds, producing an underrepresentation of the spatial variability of the precipitation distribution (Braaten, 2000; King et al., 2004).

Traditionally, researchers have used coupled ocean-atmosphere climate models (e.g. models of CMIP5 and previous versions) and global reanalyses (e.g. the European Centre for Medium-range Weather Forecasts (ECMWF) Interim reanalysis (ERA Interim) and ERA-5, the National Centers for Environmental Prediction (NCEP), Climate Forecast System Reanalysis (CFSR)) to evaluate precipitation in Antarctica at regional scale (Genthon et al., 2009; Bromwich et al., 2011). However,

these datasets contain different levels of uncertainty due the lack in observational data (Tang et al., 2018) and to the fact that certain microphysical properties of Antarctic precipitation are not well understood and represented (Listowski et al., 2019). The closest approach to obtain an observational product to evaluate precipitation in Antarctica, at the continental scale, is using satellite data. Genthon et al. (2003) analyzed the temporal variability of precipitation using reanalyses, models and the Global Precipitation Climatology Project (GPCP) monthly products, which combines passive microwaves and infrared data with gauge observations (Adler et al., 2012). GPCP products are known to have large errors in high latitude regions because of the lack of in-situ observations and difficulties of passive-microwave instruments to detect the complex scattering signal from falling snow. However, Genthon et al. (2003) found that GPCP satellite products are more reliable after 1988 and can be used to characterize Antarctic precipitation variability, using it in combination with other datasets.

Recently, new satellite missions have been launched with the objective of monitoring precipitation at large scale, using the advantage of active remote sensing to measure hydrometeor microwave scattering properties, such is the case of the Tropical Rainfall Measurement Mission (TRMM), the Global Precipitation Measuring (GPM) mission and the Cloud Satellite (CloudSat) mission (Tapiador, 2017; Wood, 2011). From these three different data sources of precipitation, only CloudSat can provide information in most of Antarctica, while TRMM and GPM only cover up to the latitudes 35° and 65° south, respectively. Palerme et al. (2014) performed the first model-independent climatology of Antarctic precipitation using two snowfall products derived from the Cloud Profiling Radar (CPR) on board of CloudSat: 2C-PRECIP-COLUMN to assess precipitation phase (Haynes et al., 2009) and 2C-SNOW-PROFILE to obtain snowfall rate (Wood, 2011; Wood et al., 2013), covering most of the AIS (latitude $< 82°$ S) with a spatial resolution of 1° of latitude by 2° of longitude. This new precipitation dataset has a great potential to evaluate current precipitation models as shown by Palerme et al. (2017a), but still presents a significant uncertainty associated to the lack of in-situ observations and the assumptions about particle size distribution, microphysical and scattering properties of the hydrometeors, used to establish the relationships between radar reflectivity factor (Z) and the snowfall rate (S). Additionally CloudSat observations near the surface are contaminated by ground clutter interference (1200 m closest to the surface), which leads to systematic errors with respect to ground precipitation, that are difficult to assess (Maahn et al., 2014).

Understanding cloud and precipitation properties is key to improve the satellite products and the representation of precipitation in regional and global models, in order to reduce biases in the current and future predictions (Gorodetskaya et al., 2015). Simulation of cloud cover is one of the main reasons of the large biases observed in the prediction of surface radiation derived from mesoscale high-resolution models (Bromwich et al., 2013), together with occurrence of supercooled liquid water (SLW) clouds (King et al., 2015; Listowski and Lachlan-Cope, 2017). It is fundamental to understand the microphysical processes that govern the fraction of SLW with respect to ice particles within the mixed-phase clouds, in order to reduce surface radiative biases in high resolution models (Listowski et al., 2019). The presence of SLW in top of clouds is an important component in the solar radiation budget, representing between 27% and 38% of the total reflected solar radiation between the pallarel 40° and 70° S (Bodas-Salcedo et al., 2016). The monitoring of SLW bearing clouds takes great importance for the improvement of the cloud microphysics modelling in Antarctica. Lidar observations provide useful information to characterize cloud hydrometeors, based on light scattering properties (Listowski et al., 2019). In the case of lidar systems capable of polarization detection, it is possible to assess the phase and habit of the particles (Sassen, 1977). In this context, spaceborne lidar systems, as CALIOP (Cloud-Aerosol Lidar with Orthogonal Polarization), on board of CALIPSO (Cloud-Aerosol Lidar and Infrared Pathfinder Satellite Observation) represent a useful tool for cloud and precipitation monitoring (Stephens et al., 2002).Other optical instruments such as the Atmospheric Laser Doppler Instrument (Aladin), part of the resent Aeolus of the ESA (European Space Agency), and The ATmospheric LIDar (ATLID) on board of the coming mission EarthCARE (Earth Clouds, Aerosols and Radiation Explorer), represent important contributions to the research of cloud, aerosols and precipitation (Schillinger et al., 2003; Hélière et al., 2007, 2016).

The spaceborne products, derived from CloudSat and CALIPSO represent unique tools to study the vertical and horizontal structure of the precipitation in Antarctica, like none that has previously existed. However, both source of information present important limitations (Mace and Zhang, 2014) that have to be taken into account. The radar instrument on board of CloudSat cannot detect hydrometeors in the lowest ∼1.2 km near the surface (Marchand et al., 2008; Maahn et al., 2014); small-scale clouds or precipitation processes may be potentially not captured by CPR due to the coarse spatial resolution (2 km in the track direction, 1 km in the cross-track and 480 m in the vertical); despite the high sensitivity of CPR

(minimum detectable signal: ∼-30 dBZ), very small non-precipitating liquid water clouds and optically thin and cold cirrus are not detected (Sassen et al., 2009; Mace and Zhang, 2014); in the case of CALIOP, it is strongly affected by the attenuation of optically thick clouds and precipitation, losing the signal near the surface when it occurs. Both instruments presents problems due to power limitation, CPR can observed only during the daytime, since late 2009 a soft-short circuit in a power cell produced a lost of nighttime data for a full month and then the complete failure on the battery on April 2011 stopped all night observations (Nayak et al., 2012), which means that CPR cannot provide polar winter profiles (Souverijns et al., 2018b). On the other hand, the sensitivity of CALIOP is reduced during daylight (Mace and Zhang, 2014).

During the last years, long-term observations of precipitation and microphysical properties of clouds have been established to provide in-situ data for calibration and validation of models and satellite data, deploying different instruments in two sites in Antarctica. Observatories are deployed in Dumont d'Urville (DDU) station located on Adélie Land, and in Princess Elisabeth (PE) station located in Droming Maud Land, both in the EAIS. Observations at DDU are supported by the French project APRES3 (Antarctic Precipitation Remote Sensing from Surface, Grazioli et al. (2017a)) and and CALVA (Antartic field data for CALibration and VAlidation of meteorological and climate models and satellite retrievals, Antarctic Coast to Dome C). The observations at PE ar supported by the Belgian project HYDRANT (HYDRological cycle of ANTarctica, Gorodetskaya et al. (2015)) and its follow up AEROCLOUD project. Both sites were equipped with vertical-pointing K-band micro rain radars (MRR) that document the vertical structure of precipitations. Moreover, a polarization lidar was implemented at DDU, that allowed a complementary observation of the composition of clouds.

Alpine context

The Alps are the most important mountain range located in Central Europe, with approximately 800 km of length, an average width of 200 km, and the highest elevation located in the summit of the Mont Blanc, at 4810 meters above sea level (m a.s.l.) (Schär et al., 1998; Ravanel et al., 2013). In the valley areas, below 1000 m a.s.l., a tempered climate predominates, with short periods of snow falls in winter, which persist at the surface for a few weeks. In the Alpine areas, between 1000 and 3000 m a.s.l., the seasonal snow cover predominates, starting from

November with the first snow falls, until the beginning of summer, when the snow cover has completely melted (Schär et al., 1998). Above the climatological snow line (∼3000±1100 m.a.s.l.), temperatures remain close to the freezing point and precipitation dominates in the form of snow throughout the year (Hantel et al., 2012).

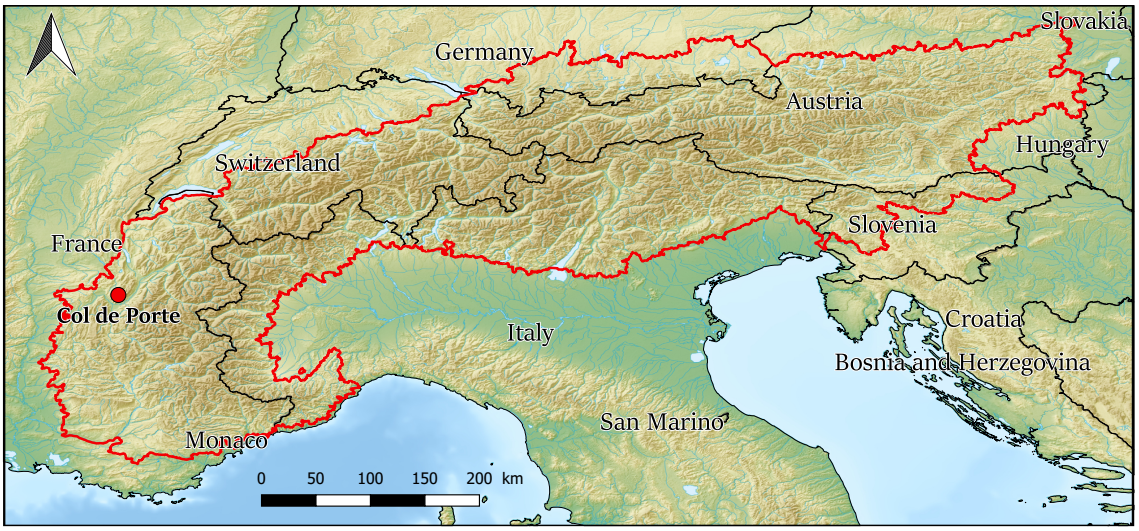

Figure 2: Alpine region map. Red line delimits the Alpine mountain range, the black lines correspond to the borders between countries anf the red dot corresponds to the location of Col de Porte station.

The Alpine region is characterized by presenting different bodies of water storage in solid state, such as seasonal snow, permanent snow fields in the high alps, glaciers and permafrost, which are fundamental for the conservation of ecosystems, the development of human settlements and infrastructure, playing an important role in the regional climate system (Schär et al., 1998; IPCC, 2013). These Alpine components are very sensitive to the primary climate elements, such as precipitation and temperature. In fact, the Alpine glaciers have shown an accelerated retreat during the last decades, and further accelerated glacier disintegration is expected for the coming years due to warming trends (Paul et al., 2007). Moreover, from a practical point of view, the quantities precipitated in the Alps, largely in the form of snow, are not sufficiently well estimated to manage risk and especially manage water resources (for agriculture, tourism, hydropower) which are likely to become more and more fluctuant in the future. Even if the observations are based on much more developed networks than in the polar regions, they are still difficult to carry out. Quantitative estimates are based on a combination of in-situ measurements and ground-based radar remote sensing estimation. But mountains complicate 1)

the structure of precipitation systems, 2) the implementation of monitoring networks and 3) the interpretation of the collected observations. Therefore, studying solid precipitation is key to understanding how this element of the climate is related to the Alpine components, society and the environment, in order to deliver useful and timely information to decision makers.

In the framework of the WMO SPICE project (see Nitu et al. (2018)), a micro rain radar, same as in the Antarctic stations (DDU and PE), was deployed in the French station Col de Porte (CDP) to monitor solid precipitation during the winter period. The Col de Porte experimental site is located near Grenoble (see Figure 2), in the Chartreuse massif at an elevation of 1325 m. At this mountain site, on the flat measurements field, meteorological and snow observations are carried out since 1961. The Col de Porte site has been widely used to evaluate snowpack models (e.g. Crocus) and to test new instruments for meteorological measurements. All these measurements are crucial inputs to assess the effects of climate on Alpine snow cover.

Objectives and outline

The objectives of this thesis, focused on the study of solid precipitation using ground based remote sensing, were the following: 1) to document the composition of clouds in Antarctica especially to describe the different ice types and to detect the presence of supercooled liquid water, and that from the first meters to the first kilometers above the ground where satellite products are not available. 2) to characterize the vertical structure of the precipitation in Antarctica and the Alps. For both environments, it is needed to understand the main microphysical processes controlling precipitation variability. For Antarctica, this knowledge is necessary for the calibration and the validation of satellite observations and modelling purposes. For the Alps, this documentation is useful for the ground radar-based precipitation estimation. The first aspect of the study concerns the processing and analysis of observations collected by a vertically profiling single-wavelength (532 nm) elastic lidar system and its polarization capacity for the detection of clouds and precipitation and discrimination of different types of hydrometeors. The lidar system was developed in the framework of the project APRES3 with support by CNES (program EECLAT), deployed at DDU station and the main objective is to establish an operational and automatic classification of cloud and precipitation hydrometeors, in order to assess the occurrence of supercooled liquid water (SLW) in mixed-phase clouds, analyzing

the temporal and vertical distribution of the various types of hydrometeors during the period of observation. Such information is relevant for comparison with similar satellite-derived products, like the DARDAR (standing for raDAR/liDAR, Delanoë and Hogan (2010)) algorithm from CloudSat/CALIPSO observations.

The second aspect of the work is devoted to the study of the vertical structure of precipitation in Antarctica and in the Alps using micro rain radar (MRR) observations, analyzing the vertical distribution of the equivalent radar reflectivity (Ze), the mean Doppler vertical velocity (W) and the spectral width (σ) to understand the main microphysical processes involved in its variability. This knowledge represents an important contribution to the study of precipitation at the levels closest to the surface, where satellite remote sensors often present a lack of information. To achieve this objective, MRR observations were used in Antarctica and Alps. In Antarctica, the observations come from the DDU and PE stations, including two uninterrupted years in DDU and mainly multiple summer observations in PE. In the Alps, a shorter period of observations, corresponding to two winter seasons with MRR was used, coming from the Col de Porte station, in the French Alps.

This doctoral dissertation is structured in five chapters after the introduction. In Chapter 1 the instruments and datasets are presented, providing the background of the principles of remote sensing from surface, including the detection of microwave scattering properties of the hydrometeors using radar and the optical properties using lidar systems. Chapter 2 is the study of the cloud and precipitation particle classification using lidar at DDU. Chapter 3 provides the study of the vertical structure of precipitation at two stations in East Antarctica using micro rain radars, while Chapter 4 presents the analysis of the vertical structure of the Alpine station. In Chapter 5, the conclusions of the work and perspectives are summarized.

Chapter 1

Instruments and datasets

1.1 Introduction

Clouds have a significant impact on the atmospheric radiation budget and hydrological cycle. The interaction of different types of clouds with incoming solar radiation and with outgoing radiation emitted by the Earth influence the global energy balance (Hartmann et al., 1992; Bony et al., 2015). On the other hand, clouds play an important role in the formation and transport of precipitation, affecting the water cycle (Andronache, 2014).

Nowadays, the use of remote sensing techniques to study clouds and precipitation is crucial in order to obtain relevant and timely information. Radar and lidar are both remote sensing systems that cover an import portion of the electromagnetic spectrum, in the radiowaves and optical regions (see Figure 1.1), which allows them to provide a broad range of high spatial and temporal resolution applications associated with cloud and precipitation monitoring, the research of atmospheric constituents and the understanding of complex physical processes (Wandinger, 2005).

This chapter is divided in three main sections: (1) the radar principles, where the scattering regime and the relation between radar reflectivity factor and snowfall rate are presented, together with the description of the micro rain radar system (MRR) used in this work; (2) the lidar principles, specifically on the lidar equation, calibration and linear depolarization; and (3) the description of the datasets, separated into study sites and instruments and data.

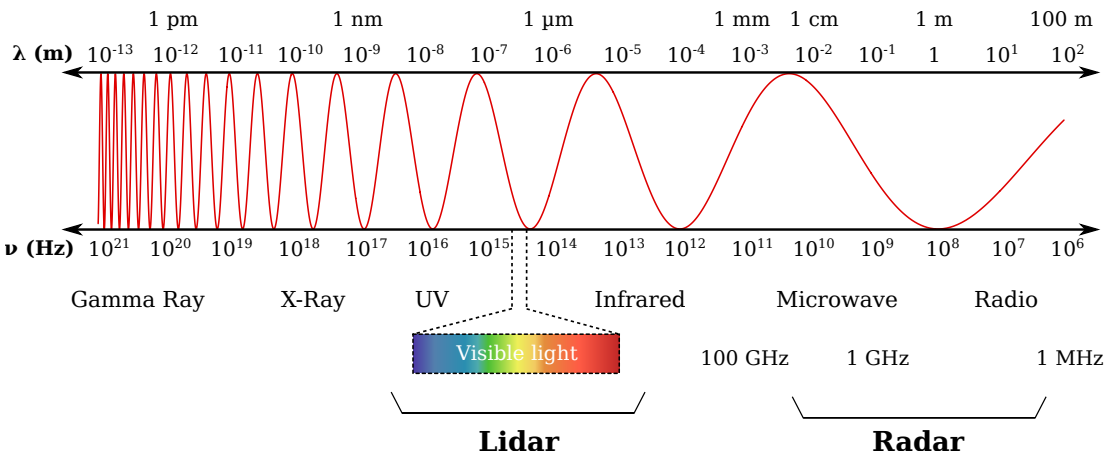

Figure 1.1: Electromagnetic spectrum.

1.2 Radar remote sensing

1.2.1 Background

Originally, radars (standing for RAdio Detection And Ranging) were developed for military purposes at the beginning of World War II, with the aim of detecting airplanes and warships, ensuring a strategic advantage on the enemy (Atlas, 1990). The radar operators soon noticed that the signal interacted with the elements present in the atmosphere, especially clouds and precipitation, which motivated meteorologists to investigate this new source of information to study atmospheric phenomena. In the later decades, advances in radar technology (e.g. improvements in resolution, polarization techniques, etc.) and the better understanding of the interactions between electromagnetic radiation and hydrometeors, allowed us to have timely information for operational weather forecasting, quantitative precipitation estimation, and more recently, for assimilation into numerical models (Andronache, 2014; Lohmann et al., 2016).

In meteorology, radar is an active remote sensing system that consists in the transmission of an electromagnetic pulse or signal through the atmosphere, which is intercepted and scattered in all directions by hydrometeors (and other non-meteorological targets) and part of this energy returns to the radar (backscattered signal or echoes), where it is measured by the radar receiver, and subsequently processed by a computer. The backscattered signal is an important source of information to characterize clouds and precipitation. The amplitude of the received signal provides information about the intensity of the precipitation, and on the other

side, information about the distance between the radar and the scatters can be obtained by knowing the speed of wave propagation (the speed of light c) and travel time of the electromagnetic pulse (Andronache, 2014; Lohmann et al., 2016).

Radars are essential tools for precipitation monitoring, due to the advantages that they provide with respect to the point observations performed with rain or snow gauges. Depending on the scanning configuration, radars can deliver information in (usually) vertical profiles or in three dimensions (horizontal and vertical), with a large spatial coverage, from a few kilometers to a few hundreds of kilometers. The large capacity of monitoring the precipitation delivered by the radars allow us to understand the evolution of precipitation in terms of space and time, develop advanced warning of hydro-meteorological hazards as well as to characterize processes that cannot be presented by traditional measurements. This information provides crucial information to validate and improve the simulation of precipitation in models.

Depending on their frequency (or wavelength), radars can be classified into different categories or bands (see Table 1.1). Each of these bands determines the ability to remotely detect clouds and/or precipitation, and also are crucial for the design of the radar systems. The half power beam-width ϕ (in degrees), the antenna size D_R and the wavelength λ (both in units of length) are related according to the following expression:

$$\phi = \kappa\lambda/D_R \tag{1.1}$$

where κ is a factor expressed in degrees, which depends on the shape of the antenna (Valkenburg and Middleton, 2001; Andronache, 2014). For the same average transmission power and ϕ, the higher the frequency (the shorter the wavelength), the more sensitive the radar is to smaller particles and requires a smaller antenna, and also becomes more sensitive to attenuation (Andronache, 2014). Currently, due to the limitations of the antenna size, space missions operating with radars using high frequency bands (greater than Ku) (Kummerow et al., 1998, Stephens et al., 2008, Hou et al., 2013), while at ground level, radar systems can afford to use lower frequencies (larger antennas) such as the operational weather radars in bands S, C and X (Van de Beek et al., 2010), which are more suitable for heavy precipitation (Lohmann et al., 2016).

The characteristics of each radar system and the type of hydrometeors observed are closely related to the type of information obtained and the way in which it can be analyzed. It is therefore important to understand how electromagnetic waves

Table 1.1: Nominal Frequencies and wavelengths of radar bands. The main radar band used in this work is bold format. (Andronache, 2014).

Band	Nominal frequency	Nominal wavelength
LF	30–300 kHz	10–1 km
MF	0.3–3 MHz	1000–100 m
HF	3–30 MHz	100–10 m
VHF	30–300 MHz	10–1 m
UHF	300–3000 MHz	1–0.1m
L	1–2 GHz	30–15 cm
S	2–4 GHz	15–8 cm
C	4–8 GHz	8–4 cm
X	8–12 GHz	4–2.5 cm
Ku	12–18 GHz	2.5–1.7 cm
K	**18–27 GHz**	**1.7–1.2 cm**
Ka	27–40 GHz	1.2–0.75 cm
W	75–110 GHz	4.0–2.73 mm
G	110–300 GHz	2.73–0.1 mm

interact with particles, and how radars are used to monitor precipitation. In the following subsections the principles of radar scattering by simple and distributed targets, and the relationship between radar reflectivity factor and precipitation rate are presented. The details of the K-band vertical Doppler micro rain radar (MRR) system used in this work are also provided.

1.2.2 Scattering regime

Scattering by particles depends on several factors related to the particle itself, such are the size, shape, orientation, temperature and composition (e.g., ice, liquid or mixed phase), and external factors as the wave frequency. The response of a target of a given composition to electromagnetic radiation is expressed by means of the dielectric constant or relative permittivity (ϵ_r, unitless). ϵ_r is a complex number, in which the real part ϵ_r' is proportional to the amount of backscattered energy and the imaginary part ϵ_r'' is proportional to the amount of energy absorbed by the particles. For the case of water, ϵ_r depends strongly on the phase of the target, the values of ϵ_r' and ϵ_r'' are both much lower for dry snow or ice than for liquid water using microwave radiation (Stiles and Ulaby, 1986; Hallikainen et al., 1986), which means that the backscattered signal from dry snow is weaker, but it is also much less affected by attenuation, around one order of magnitude less than attenuation due to liquid water at the same precipitation rate (Amaya et al., 2014). For precipitation radars, ϵ_r is approximately m^2, where m is the complex refractive index (Andronache, 2014), in

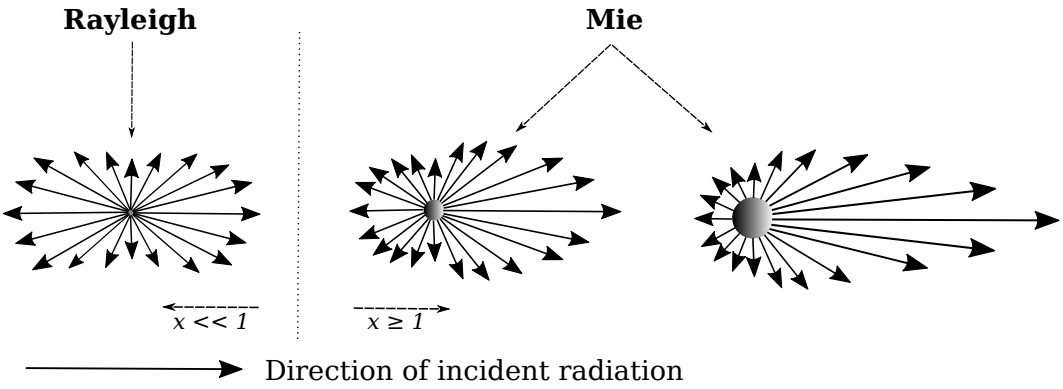

Figure 1.2: Scattering radiation patterns for Rayleigh and Mie regimes.

which the real part is the ratio of the wave's phase speed across the medium (e.g. droplets or ice particles) to that in a vacuum.

The size of the particles determines the scattering regime for a given wavelength of the transmitted power. The dimensionless size parameter

$$x = \frac{\pi D}{\lambda} \tag{1.2}$$

represents the ratio between the characteristic particle length to the wavelength λ, where D corresponds the particle equivalent spherical diameter in meters (same as λ). When the size of the scattering object is much smaller than the wavelength ($x << 1$), Rayleigh scattering occurs. Under a Rayleigh scattering regime, the radiation is scattered backward and forward in the direction of the electromagnetic wave propagation, in the same proportion, favoring the radar detection of backscattered radiation. Rayleigh regime is responsible for the detection of cloud droplets by cloud radars with millimeter wavelengths and for the detection of raindrops and snow by precipitation radars with centimeter wavelengths. When $x \sim 1$, Mie scattering predominates, favoring the forward scattering and reducing the backscattering signal toward the radars. The geometry of the Rayleigh and Mie scattering regimes is presented in Figure 1.2. As mentioned before, the maximum scattering in the backward and forward directions of the incident radiation is shown as example for the Rayleigh regime. In the case of Mie, the pattern of scattering depends on the size and shape of the particle, and exhibits an irregular distribution with predominance in the forward direction (Rauber and Nesbitt, 2014). The amount of backscattered radiation towards the radar from a target is characterized by its radar cross-section (σ), which corresponds to the cross-sectional area of a hypothetical isotropically

scattering target. When Rayleigh regime is valid, the so-called Rayleigh approximation to the Mie solution to the to Maxwell's equations for σ (in m^2) is expressed as:

$$\sigma = \frac{\pi^5}{\lambda^4}|K|^2 D^6 \tag{1.3}$$

where K (unitless) is the dielectric factor, which is a function of the complex refractive index m (unitless):

$$|K|^2 \equiv \left|\frac{m^2-1}{m^2+2}\right|^2 . \tag{1.4}$$

These parameters will be useful for the description of the radar equation, with describes the relationship between the power transmitted and the power received by the radar, that is presented in the following subsection, together with the radar reflectivity.

1.2.3 Power and radar reflectivity

1.2.3.1 Radar equation for single target

The energy scattered by a target and measured by the radar receptor P_r (in Watts) can be expressed as in the following equation:

$$P_r = S_r A_e \tag{1.5}$$

where S_r (in W m^{-2}) corresponds to the power flux density of the scattered wave at the receiving antenna and A_e is the effective area of the radar antenna in m^2. S_r is proportional to the power flux density of the wave incident on a target S_i (in W m^{-2}) located at range r (in m) far from the radar and its radar cross-section σ, according to the expression:

$$S_r = \frac{\sigma S_i}{4\pi r^2}. \tag{1.6}$$

In this ratio, the numerator corresponds to the power reflected by the target in all directions, and the denominator $4\pi r^2$ is the solid angle due to the isotropic propagation of the scattered wave between the target and antenna. S_i can be determined knowing the transmitted power P_t from the antenna and the gain of the antenna G (unitless), that represent the performance of the power transmission in a certain direction:

$$S_i = \frac{G P_t}{4\pi r^2}, \tag{1.7}$$

and introducing Equations 1.6 and 1.7 in Equation 1.5, we obtain P_r as function of σ, G, P_t, A_e and the distance between the radar and the target (Equation 1.8). It is important to remark that this equation corresponds to a radar with the transmitter and receiver located in the same place (i.e. monostatic radar). Radars with transmitter and receiver devices located in different places are called bistatic radars, and the radar equation undergoes a slight change in the range variable. In this manuscript, the monostatic configuration is used to describe the following equations.

The following equation corresponds to the radar equation for a single target

$$P_r = \frac{\sigma G P_t}{(4\pi r^2)^2} A_e, \tag{1.8}$$

which can be rewritten using the relationship between the effective antenna area, its gain and the wavelength : $A_e = \frac{\lambda^2 G}{4\pi}$ (Raghavan, 2003). By grouping terms, the radar equation can be written typically as follows

$$P_r = \frac{1}{64\pi^3}\left[P_t G^2 \lambda^2\right]\left[\frac{\sigma}{r^4}\right], \tag{1.9}$$

where $\left[P_t G^2 \lambda^2\right]$ correspond to parameters associated to the radar system and $\left[\frac{\sigma}{r^4}\right]$ are two parameters of the target, the scattering properties and the position with respect to the radar. Characteristics of the target, such as the shape or the composition determine the received power, which also strongly depends on the fourth power of the distance.

1.2.3.2 Radar equation for distributed targets

The smallest region scanned by a radar is called sampling volume or contributing region V_c, where a large population of hydrometeors are distributed. For conical beam of a pulse radar with circular symmetry, V_c can be approximated to a cylinder defined by the radial resolution equal to $\frac{c\tau}{2}$ and the beam cross-section at a distance r from the radar equal to $\pi(r\frac{\phi}{2})^2$, where τ is the duration of the 2-ways travel of the wave through V_c and ϕ is the beam width. The approximate volume of V_c is therefore

$$V_c = \frac{\pi c \tau \phi^2 r^2}{8}. \tag{1.10}$$

The total radar cross-section $\overline{\sigma}$ contributed by all the targets within the sampling volume corresponds to the sum of the individual σ in the assumption of single-scattering. Probert-Jones (1962) proposed the factor $\frac{1}{2\ln(2)}$, to correct the antenna

gain variations across the distributed targets inside of the sampling volume, using a theoretical approach validated with experimental data. These two approximations about distributed targets lead to a new radar equation:

$$\overline{P}_r = \frac{1}{64(2\ln(2))\pi^3}\left[P_t G^2 \lambda^2\right]\left[\frac{\sum_n \sigma_j}{r^4}\right], \tag{1.11}$$

where $\overline{P}_r$ is the received power by multiple targets j. $\overline{\sigma}$ divided by the volume of V_c is called the radar reflectivity η (in m^2 m^{-3} or m^{-1}) denoted as

$$\eta = \frac{\overline{\sigma}}{V_c} = \frac{\sum_j \sigma_j}{V_c}, \tag{1.12}$$

this quantity represents all the contributions of radar cross-section per unit of volume. Using Equations 1.12 and 1.10, the radar reflectivity can be obtained as a function of η as follow

$$\overline{P}_r = \frac{c}{1024(\ln(2))\pi^2}\left[P_t G^2 \lambda^2 \tau \phi\right]\left[\frac{\eta}{r^2}\right], \tag{1.13}$$

and grouping all the constant dependent on the radar system in to C_r, the radar constant, the radar equation can be simplified into

$$\overline{P}_r = C_r\left[\frac{\eta}{r^2}\right]. \tag{1.14}$$

The Rayleigh approximation for the radar cross-section presented in Equation 1.3 can be rewritten to account for all possible particle sizes within the sampling volume as it is shown in Equation 1.15

$$\overline{\sigma} = \frac{\pi^5}{\lambda^4}|K|^2 \sum_j D_j^6, \tag{1.15}$$

where $\sum_j D_j^6$ corresponds to the sum of the diameter D of all the individual targets inside of V_c. Replacing $\overline{\sigma}$ from Equation 1.12 by the Rayleigh approximation of Equation 1.15, a definition of η is obtained as function of the size of the targets:

$$\eta = \frac{\overline{\sigma}}{V_c} = \frac{\pi^5}{\lambda^4}|K|^2 \frac{\sum_j D_j^6}{V_c}. \tag{1.16}$$

The sum of the diameters of the particles per unit of volume is called radar reflec-

tivity factor Z (in mm^6 m^{-3}), defined by the following equation:

$$Z = \frac{\sum_j D_j^6}{V_c}, \tag{1.17}$$

which allows to rewrite the Equation 1.16 as follows

$$\eta = \frac{\pi^5}{\lambda^4}|K|^2 Z. \tag{1.18}$$

Using Equation 1.18, the received power in the radar equation for distributed targets can be expressed as function of the radar reflectivity as

$$\overline{P}_r = C_r \frac{\pi^5 |K|^2 Z}{\lambda^4 r^2}. \tag{1.19}$$

In this equation, the radar reflectivity factor Z depends only on the hydrometeor properties and is determined by the drop/particle size distribution, while the radar reflectivity η (see Equation 1.12) depends on hydrometeor properties, but also in the radar wavelength. The constants independent of the target can be included in C_r to simplify the expression, obtaining the following radar equation:

$$\overline{P}_r = C_r \frac{|K|^2 Z}{r^2}. \tag{1.20}$$

As generally the properties of hydrometeors are not known a priori and it is not possible to know if the Rayleigh regime is valid, the equivalent radar reflectivity factor (Z_e) is introduced, which assumes that all hydrometeors are small spherical liquid drops with respect to the wavelength, and radar cross-section can be expressed using the Rayleigh approximation. Under these assumptions, the radar equation is reformulated as:

$$\overline{P}_r = C_r \frac{|K_w|^2 Z_e}{r^2}. \tag{1.21}$$

where K_w is the dielectric factor of liquid water, equal to 0.93, for operational weather radar wavelengths. Z_e is usually transformed to decibels or dBZ, because the range of observed values can span several orders of magnitude in clouds and precipitation (see Table 1.2).

$$Z_e[dBZ] = 10 \cdot log_{10}\left[\frac{Z_e[mm^6 m^{-3}]}{1[mm^6 m^{-3}]}\right] \tag{1.22}$$

Table 1.2: Typical values of Z for various hydrometeors and precipitation types, detected with either a cloud or a precipitation radar. (Liu et al., 2008; Houze, 2014; Lohmann et al., 2016).

Radar type	Scatters	Z values [dBZ]
Cloud radar	Clouds and droplets	-40 to -20
Cloud radar	Mixed-phase clouds	-20 to -10
Cloud or precip. radar	Drizzle	-20 to 0
Precipitation radar	Very light rain or light snow Moderate	0 to 10
Precipitation radar	Moderate rain and heavier snow	10 to 30
Precipitation radar	Melting snow	30 to 45
Precipitation radar	Moderate to heavy rain	30 to 60
Precipitation radar	Hail	>60

1.2.4 Doppler radars

The Doppler effect is the change of the wave frequency produced by the relative motion of the source with respect to a stationary observer (Rauber and Nesbitt, 2014). When the particles approach the radar, the frequency of the received signal undergoes a slight change or Doppler shift, corresponding to an increase with respect to the transmitted frequency. Doppler radars take advantage of the Doppler shift, to retrieve information about the radial velocity (component of the velocity in the direction of the radar) of hydrometeors that move towards or away from the radar.

A pulsed Doppler radar cannot measure directly the frequency shift of the electromagnetic waves, instead it measures the associated phase shift of the received signal. For pulse radars, the distances traveled by a particle in the direction of the radar during a single pulse is proportional to the frequency shift $\Delta\nu$ and the wavelength λ as $\frac{\lambda}{2}\left(\frac{\Delta\nu}{2\pi}\right)$ (Rauber and Nesbitt, 2014). Thus, the radial velocity of the particle v_r is computed dividing this expression by the pulse duration τ

$$v_r = \frac{\lambda}{2\tau}\left(\frac{\Delta\nu}{2\pi}\right). \tag{1.23}$$

Other systems such as the frequency-modulated continuous-wave (FMCW) radar, used mostly for short-range observations due to receiver limitation (Anghel et al., 2014), transmit a continuous wave with a frequency that varies over a fixed period of time called sweep, with a specific shapes of modulation (see Figure 1.3). These type of Doppler radars provide information of the Doppler shift and also the distance or range of the particle from the radar. The signal from several sweeps can be used to determine the range r and the radial velocity v_r of the particles, organizing them in a matrix of time in the rows by number of sweeps in the columns.

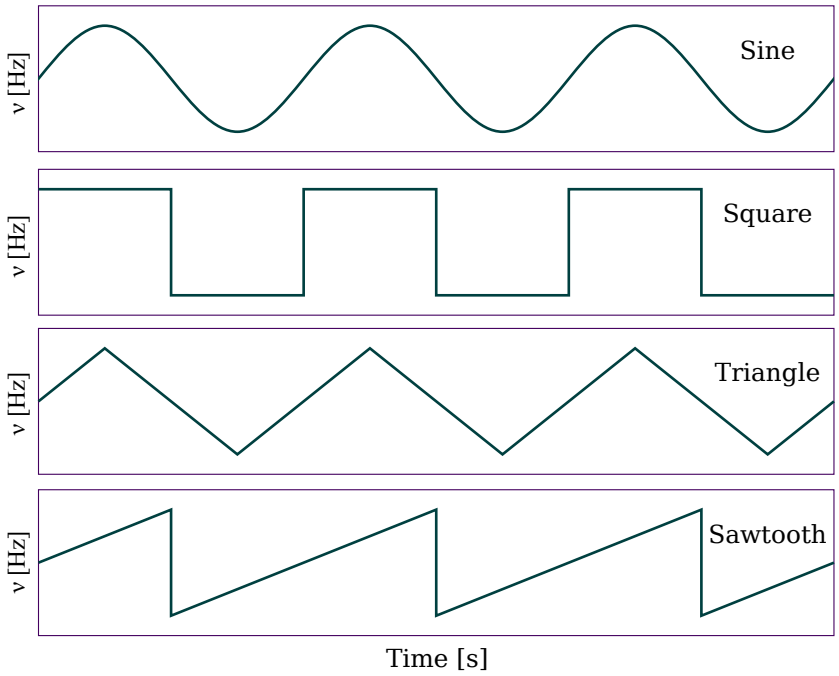

Figure 1.3: Typical modulation shapes for FMCW radars. The horizontal axis corresponds to time and the vertical axis is the variation of the wave frequency. The data used in the work is derived from a radar with sawtooth modulation.

With the help of the Fast Fourier Transform (FFT) it is possible to retrieve both components separately (r and v_r). A first FFT in each column provides the range resolved signal in the domain of the frequencies and a second FFT of each row (corresponding to range bins) provides the radial velocity for different Doppler frequency or phase shift. The signal in the domain of radial velocities is known as the Doppler power spectrum or simply Doppler spectrum and it is presented in the following subsections.

1.2.4.1 The Doppler spectrum

As mentioned before, all individual particles within the sampling volume contribute to a fraction of the total radar cross-section, thus in the total received power. The variety of particle sizes and terminal velocities leads to a spread distribution of spectral power (related to reflectivity) as a function of radial velocity (i.e. projection of the particle velocity in the direction of the radar beam), called Doppler spectrum. Other factors as the wind shear, turbulent eddies, constant sustained updraft and downdraft can also contribute to broaden the distribution of particle radial velocities (Rauber and Nesbitt, 2014).

The information derived from Doppler spectrum is used to study cloud physics,

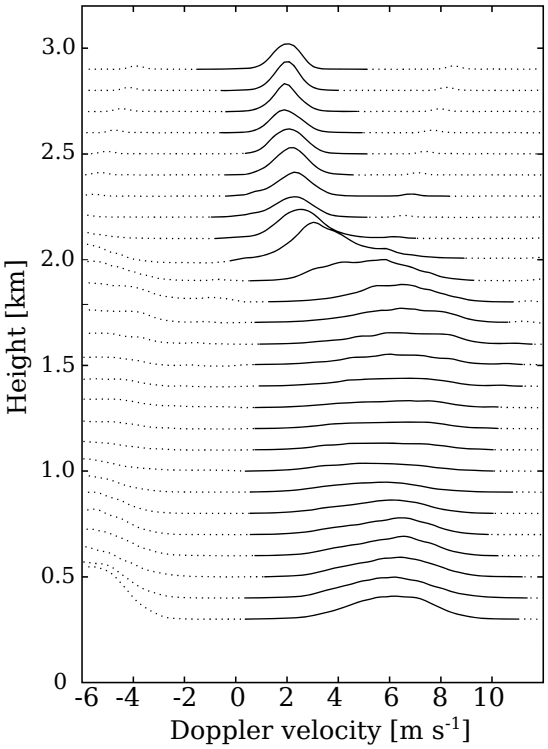

Figure 1.4: Example of range resolved Doppler spectra for a stratiform precipitation event in the Alpine region (Grenoble), derived from a vertically pointing micro rain radar (MRR). Height is expressed in distance above instrument level. Each black curve represents the Doppler spectrum, where the vertical variations are proportional to the signal variations. Dotted portion of the lines correspond to noise.

(e.g. Mace et al., 2002) and vertical structure of precipitation (e.g. Williams et al., 2007). Figure 1.4 shows an example of Doppler spectrum at different altitudes during a stratiform precipitation events in the Alpine region observed with a vertically pointing K-band MRR. In this example it is possible to observe the vertical evolution of the precipitation in terms of the distribution of Doppler velocities. In the top of the profile, 2 km above the instrument level, the velocities are rather low compared to the higher, but spread velocities near the ground. The transition from solid precipitation in the upper part of the profile to liquid precipitation toward the surface is evidenced, which can be associated to the change of the aerodynamic properties of the hydrometeors.

The Doppler spectrum can be characterized using parameters called Doppler moments, that correspond to the average contribution radar reflectivity $\overline{\eta}$, the mean Doppler velocity and the spectral width which is associated to the spread of the radial velocities. They are described in more detail below.

1.2.4.2 The Doppler moments

Doppler spectra are used to retrieve information about the radar reflectivity produced by the ensemble of hydrometeors within the contributing volume $\overline{\eta}$, used to retrieve Z_e, the mean radial velocity of the contributing volume $\overline{v}_r$ and the respective spectral width σ_v. Operationally, the use of Doppler moments allows to condense the large volume of data to a more simple, but information-rich parameters, in order to reduce the data storage requirements. These parameters correspond to the three first moments of the Doppler spectra and are defined by the following expression:

$$\overline{\eta} = \int_{-v_{max}}^{+v_{max}} \eta(v_r) dv_r \tag{1.24}$$

$$\overline{v}_r = \frac{\int_{-v_{max}}^{+v_{max}} v_r \eta(v_r) dv_r}{\overline{\eta}} \tag{1.25}$$

$$\sigma_v = \sqrt{\frac{\int_{-v_{max}}^{+v_{max}} (v_r - \overline{v}_r)^2 \eta(v_r) dv_r}{\overline{\eta}}}, \tag{1.26}$$

where $\eta(v_r)$ correspond to the contribution of radar reflectivity by each radial velocity bin.

The value of $\overline{\eta}$ retrieved from the Doppler spectra is called the zeroth moment and it corresponds to the area between the curve $\overline{\eta}$ and the noise level. Using Equation 1.24 it is possible to obtain the equivalent reflectivity factor. The first Doppler moment is the mean radial velocity $\overline{v}_r$, which is the η-weighted mean Doppler velocity. This moment is the velocity of the ensemble volume, associated to the particle movement due to gravitation and all air motion contributions. In the case of vertically pointing radars, the first moment represents the mean particle fall speed, denoted by W, produced by terminal velocities and vertical air motion of individual particles (Rauber and Nesbitt, 2014). The second Doppler moment σ_v represents the standard deviation of the Doppler spectrum and is called the spectral width. The value of $\overline{\sigma}_v$ characterize the variability of radial velocities within the contributing volume. The spread of velocities in the Doppler spectrum can be produced by the contribution of turbulence, wind shear and the different in fall velocities of each individual hydrometeor (Raghavan, 2003; Rauber and Nesbitt, 2014).

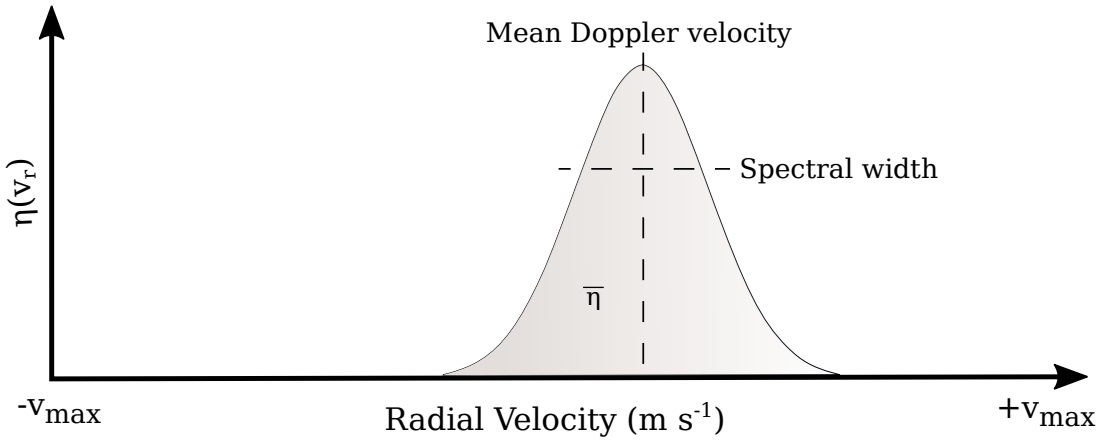

Figure 1.5: Idealized Doppler Spectrum. $\eta(v_r)$ is the radar reflectivity as function of the radial velocity. The vertical dashed line represents the mean Doppler velocity, the horizontal dashed line corresponds to the spectral width of the Doppler spectrum and the shadowed area represents the averaged received power by the radar.

1.2.5 Estimation of snowfall with $Z_e - S$ relationships

Snowfall rate S has been previously studied using the relationship between the equivalent radar reflectivity factor Z_e and the observed snowfall rate (e.g. Matrosov, 1992; Matrosov et al., 2009; Wolfe and Snider, 2012), using a power law relationship as

$$Z_e = aS^b \tag{1.27}$$

where Z_e is the equivalent reflectivity factor in $\text{mm}^6\ \text{m}^{-3}$ and S is the liquid water-equivalent snowfall rate in $\text{mm}\ \text{h}^{-1}$, and a and b are the power law coefficients, both dependent on the variability of the particle bulk densities, fall velocities, and particle size and shape distributions (Matrosov et al., 2009). The calibration of these coefficients to different precipitation characteristics and radar systems has been an important subject in radar meteorology, and recently it has been of interest for the study of precipitation in Antarctica (e.g. Grazioli et al., 2017a; Souverijns et al., 2017).

Two different approaches are used to optimize the $Z_e - S$ relationship coefficients, (1) from a theoretical approach, analyzing the values of Z_e and S estimated from models of particle mass-size and terminal-size relationships and particle size distribution (PSD); (2) and from an experimental approach, using co-located ground-based radar and snowfall rate observations (Matrosov, 1992).

The a coefficient is the most sensitive and strongly depends on the particle

Table 1.3: Coefficients for different $Z_e - S$ relationship available in Matrosov et al. (2009) (B90 and W08); Kneifel et al. (2011)(N06, M07 and K09); Grazioli et al. (2017a) (G17) and Souverijns et al. (2017) (S17). In B90 and W08, a, b and c correspond to different mass-size relationships used by Matrosov et al. (2009). We obtained CDP relationships using experimental fitting for snow and rainfall observations.

Relationship	A	B	Observation
B90-a	67	1.28	
B90-b	114	1.39	Aggregate snowflakes, surface-based PSD
B90-c	136	1.30	
W08-a	28	1.44	
W08-b	38	1.56	Low density aggregate snowflakes, aircraft-based PSD
W08-c	48	1.45	
N06	89	1.04	Sectored snowflakes and dendrites
M07	56	1.20	Scattering properties of snow aggregates
K09-LR3	24	1.51	Three bullet rosettes
K09-HA	313	1.85	Aggregate ice particles
K09-SS	20	1.74	Low-density spherical snow particles
G17	76	0.91	Experimental local relationship at DDU
S17	18	1.10	Modeled local relationship at PE
CDP-S	23	0.97	Experimental local relationship at CDP for snow
CDP-R	135	1.41	Experimental local relationship at CDP for rain

bulk density. Table 1.3 shows the variability of a and b coefficients for different $Z_e - S$ relationships, derived from both theoretical and experimental approaches, for different type of particles, where values of a present the highest variability.

Recently, $Z_e - S$ relationships have been established locally in Antarctica using empirical fitting at the Dumont d'Urville station using radar-derived Z_e and in-situ snow gauge observations by Grazioli et al. (2017a). The parameters were fitted using a modeling approach combined disdrometer and radar observations at Princess Elisabeth station by Souverijns et al. (2017).

1.2.6 Micro rain radar (MRR)

Micro rain radar (MRR) is a Frequency-modulated continuous-wave (FMCW) vertically pointing radar working at 24 GHz of frequency (see more detail in Table 1.4). Originally, the MRR was developed as a rainfall profiler, exploiting an idealized relationship between size and fall velocity of liquid precipitation (Atlas et al., 1973) and assuming absence of vertical wind (Peters et al., 2002, 2005). For the case of

Table 1.4: MRR characteristics. Source : Maahn and Kollias (2012).

MRR characteristics	Value
Frequency (GHz)	24
Radar type	FMCW
Transmit power (W)	0.05
Receiver	Single
Radar Power consumption (W)	25
System power consumption (plus antenna heating) (W)	225
No. of range gates	31
Range resolution (m)	10–200
Range resolution used in this study (m)	100
Resulting measuring range (km)	3
Antenna diameter (m)	0.6
Beam width (2-way, 6 dB)	1.5°
Nyquist velocity range (m s^{-1})	±6.0
No. of spectral bins	64
Spectral resolution (m s^{-1})	0.19
Averaged Spectra (Hz)	5.8

snowfall, the large variability of particle shapes and density changes the size-fall velocity relationship and introduces a large uncertainty in the estimation of the snow rate, thus this approach is not suitable for snow precipitation. Recently, new approaches have been proposed to address this problem through the direct integration of the Doppler spectrum to calculate Doppler radar moments such as effective reflectivity (Z_e), mean Doppler velocity (W) and spectral width (σ_v) (Kneifel et al., 2011; Maahn and Kollias, 2012). In this work, MRR data were processed using the method proposed by Maahn and Kollias (2012) (hereafter noted MK12) that improves the noise filtering algorithm and implements a dynamic procedure to dealiase the Doppler spectrum, allowing to take into account very small and negative W (cases of weak updraft). Despite of the Doppler velocity correction, turbulence is still a source of problems for the dealiasing procedure and affect low level observations, especially for the Doppler velocity. The two lowest ranges are usually not considered in the post-processing because they can be strongly affected by the near-field effect and the two highest range gates also are excluded from the analysis due to the high noise in the signal (MK12).

1.3 Lidar remote sensing

1.3.1 Background

Lidar (LIght Detection And Ranging) systems, together with radar, are fundamental tools for the atmospheric profiling research. Lidar is based on the transmission of a electromagnetic beam (laser) and the measurement of the backscattered light, similar as radar, but in this case the electromagnetic beam corresponds to the optical region of the spectrum (see Figure 1.5). Before the invention of laser, the first studies of the atmosphere using light were carried out during the 1930s, measuring scattering from searchlight beams to determine air density profiles; and using light pulses to measure the cloud base heights, deducing this information from the time between the emission of a pulse and the detection of the signal (Wandinger, 2005). From 1960, with the development of pulsed laser as source of light beam, lidar techniques, knowledge and technology advanced rapidly until the current state. Nowadays, lidar instruments can be used from ground-based platforms with high temporal resolutions, and on board of aircrafts to improve spatial coverage, as well as satellites to obtain global observations of atmospheric parameters from space.

A diverse range of applications associated with the observation of atmospheric parameters can be carried out with the use of lidar techniques, including the study of the depletion of the stratospheric ozone layer; the monitoring of polar stratospheric clouds (e.g. Gobbi, 1995; Solomon et al., 2016; Pitts et al., 2018); the study of the effect of aerosols on climate; and cloud classification and discrimination between water droplets and ice crystals on mixed–phase clouds using depolarization techniques (e.g. Hu, 2007; Hu et al., 2007; Hogan et al., 2004; Sassen, 1991). In the following subsection a description of the elastic backscattering principle, the lidar equation and the concepts of linear depolarization are presented.

1.3.2 Elastic scattering

In the scattering theory, the elastic scattering is a form of scattering by particles. For atmospheric lidars, it means that lidar transmits a laser signal at a given wavelength, which illuminates the molecules and particles present in the atmosphere and then it is scattered in all direction without changing the wavelength of the transmitted radiation, which means that the wavelength and the total energy of the incident photons are conservative with respect to the scattered light, but with different directions of propagation. This type of lidar systems, so-called Rayleigh–Mie lidar,

provides remote sensing information of molecules, aerosols, clouds and precipitation particles (Wandinger, 2005), because scattering can be separated into Rayleigh and Mie regimes depending of the type of scatters and wavelength. It is important to clarify that in the scattering theory, Rayleigh is an approximation of Mie scattering, however in lidar studies one or the other term are often used depending on whether the scatters are molecules or particles, due to their relative size with respect to lidar wavelength.

The type, size, shape and composition of the atmospheric particles play an important role in the scattering pattern. The complex refractive index m proper of a given media (e.g. the air, water drops, ice particles) and wavelength, are important parameters which governs the scattering and also the absorption of light (Kovalev and Eichinger, 2004). The real part is the ratio of speed of electromagnetic field within the medium of the scatterer to the speed of light in free space (see section 1.2.2). The ability of the medium to absorb is defined by the imaginary part of m. The real part of m varies between 1.35 to 1.6 in the visible and near-infrared part of the electromagnetic spectrum, while the imaginary part ranges from 0 to 0.1. In the case of clear sky atmospheres (such as Antarctic atmosphere), the absorption is negligible and the imaginary part of m is ignored for lidar wavelength (Kovalev and Eichinger, 2004).

The scattering produced by molecules, is referred to Rayleigh scattering when the incident radiation corresponds to the lidar wavelength, because the dimensionless size parameter x (see Equation 1.2) is much lower than 1, thus the scattering responds to the Rayleigh regime. The molecular volume scattering coefficient β_m (in m^{-1}) can be defined as follows:

$$\beta_m = \frac{8\pi^3(m^2-1)^2 N}{2N_s^2\lambda^4} \tag{1.28}$$

where N is the number of molecules per unit volume, dependent on pressure and temperature, N_s is the number density of molecules at standard conditions (i.e. N_s $= 2.547 \cdot 10^{19}$ cm^{-3} at $T_s = 288.15$ K and $P_s = 101.325$ kPa) (Kovalev and Eichinger, 2004). In this equation, it is possible to see that the molecular volume scattering coefficient has an strong dependency to the wavelength, equal to the λ^{-4}, which implies that for relative large values of λ for lidar spectrum, scattering is almost zero, while for short λ the scattering is dominated by the molecular component.

When the dimensionless size parameter x is equal to or greater than unity, the light scattering is domined by Mie scattering regime, which corresponds to that pro-

duced by particles, such as aerosols, droplets and ice crystals (She, 2007). For Mie scattering, as it is observed in the diagram of Figure 1.2, as particle size increases, the ratio of the amount of radiation scattered in the forward direction to radiation scattered in the backward direction of the transmitted wave also increases. Additionally, the variations on wavelength plays a less important role on the scattering of light by large particles, compared with the case of Rayleigh scattering (Kovalev and Eichinger, 2004).

There is another form of scattering of electromagnetic radiation different from elastic scattering, in which the incident radiation in molecules is absorbed and then re-emitted at different wavelength, this inelastic effect is called Raman scattering. Although Rayleigh scattering is the dominant regime for molecules in the lidar wavelengths, Raman scattering plays a significant role in the research of atmospheric constituents, because each molecular species (e.g. water vapour, nitrogen) produce a unique shift in the frequency/wavelength of the incident light (Kovalev and Eichinger, 2004). In the present dissertation, the Raman scattering is not detailed more deeply because the study carried out was applied to an elastic single-channel lidar. In the following subsections, the concepts of lidar equation and linear depolarization are presented.

1.3.3 Lidar equation

The basic concept of a lidar system consists in the combined operation of a light transmitter (e.g. pulsed laser) and a detection sub-system (telescope + electronic acquisition devices) (see Figure 1.8). The relation between the power transmitted through the atmosphere and the received signal, known as the lidar equation, is described in the following expression (see Figure 1.29):

$$P(r) = P_T A \frac{c\tau}{2} \eta_l \frac{O(r)}{r^2} \beta(r) exp\left[-2 \int_0^r \alpha(R) dR\right] + Bs, \tag{1.29}$$

where P (in Watts) is the power received by the lidar, dependent on the range r (R) in meters, P_T is the transmitted power, A is the area of the telescope in (m^{-2}), c is the speed of the light, τ is the temporal pulse length, η_l is the receiver efficiency (unitless), O a field of view (FOV) overlapping function (a factor from 0 to 1) between the telescope and the laser beam, β and α are the volume backscattering and extinction coefficients in m^{-1}, which can be decomposed respectively into their contributions from molecular (β_m and α_m) and aerosol (β_a and α_a) scattering. Here-

after the subindex a for aerosol makes reference to all atmospheric particles greater than molecules that produce Mie scattering, including cloud and precipitation particles. Bs is the background signal produced by electronic noise, sunlight or other source of light contamination. P_T, A, c, τ and η_l are values that remain constant in time while the configuration of the lidar system does not change, hence they can be grouped as a single calibration constant C_l. The term $exp\left[-2\int_0^r \alpha(R)dR\right]$ of the equation corresponds to the two-way path atmospheric transmission T^2.

When the transmitted power is polarized, assuming that the atmospheric attenuation is polarization independent (see Snels et al. (2009)), the relationships between backscatter coefficients and the received signals are determined by:

$$P_{\parallel,\perp}(r) = \frac{O(r)C_{\parallel,\perp}}{r^2}\beta_{\parallel,\perp}(r)T^2(r) + Bs_{\parallel,\perp}, \tag{1.30}$$

where the subscripts $\parallel$ and $\perp$, indicate the parallel and perpendicular polarization channels of the lidar system.

1.3.4 Linear depolarization

The volume linear depolarization ratio δ represents the probability that a transmitted polarized laser beam changes its polarization orthogonally during the interaction with scatterers and it is represented by the ratio between the perpendicular and parallel backscattered light, respect to the polarization angle of the transmitted power. The following expressions describe δ as function of β or the corrected received power P:

$$\delta(r) = \frac{\beta_\perp(r)}{\beta_\parallel(r)} = \frac{C_\parallel}{C_\perp}\frac{P_\perp(r)}{P_\parallel(r)} \tag{1.31}$$

It is widely used to study the properties of the atmosphere because it provides information for the discrimination of homogeneous and spherical particles that present $\delta = 0$ (e.g. liquid water), from irregular and randomly oriented hydrometeors with $\delta > 0$ (e.g. snowflakes). The δ estimates require only a few instrumental adjustments to take into account the optical and electronic gains of the two channels, because of its non-dependence to the extinction coefficient (Cairo et al., 1999; Sassen, 2003).

1.4 Datasets

This section is devoted to describe the datasets used in the present study. In order to accomplish this objective, the section is separated in two part: (1) the description

of the three site of study in Antarctica and Alps; (2) the presentation of the data used to carried out the study of this PhD thesis.

1.4.1 Sites

1.4.1.1 Dumont d'Urville station (DDU)

DDU is located on the Petrels Island (66°39'S, 140°00'E) at 41 m a.s.l. at the coast of Adélie Land. One of the strongest and most directional katabatic regime dominates this region with an annual average wind speed of 10 m s^{-1} (König-Langlo et al., 1998; Bromwich et al., 2011; Grazioli et al., 2017a) and an annual precipitation rate of about 679 mm w.e. yr^{-1} (liquid water equivalent per year) (Palerme et al., 2014). Katabatic winds coming from the interior of the Antarctic continent are responsible for the presence of significant blowing snow events and for the sublimation of a significant part of this blowing snow and precipitation, reducing the total amount of snow at ground level (Grazioli et al., 2017b).

1.4.1.2 Princess Elisabeth station (PE)

PE is located in Dronning Maud Land (71°57'S, 23°21'E), 173 km inland and at 1392 m a.s.l. on the Utsteinen Ridge, in the escarpment zone at the north of the Sør Rondane mountains range (Gorodetskaya et al., 2015). Meteorology at PE is characterized by alternation of two regimes, a cold katabatic regime with low wind speeds and humidity, strong near-surface temperature inversion and high surface pressure, and a warm synoptic regime with strong wind speeds, high specific humidity and low surface pressure (Gorodetskaya et al., 2013). Snowfall is generally associated with a cyclone located north-west or north of the station (Souverijns et al., 2018a). Unlike DDU, katabatic winds at PE are mostly attenuated by the blocking effect of the mountain range, but still heavy blowing snow events (reaching up to 30 m height) occur 13% of the time, mostly during transitional periods caused by strong synoptic winds (Gossart et al., 2017). Based on a full year of MRR observation at PE in 2012, the total annual precipitation ranges from 87 to 266 mm w.e. yr^{-1}, according to uncertainty in $Z_e - S$ relationship as described by Souverijns et al. (2017). An scheme of observation in DDU and PE is provided in Figure 1.6.

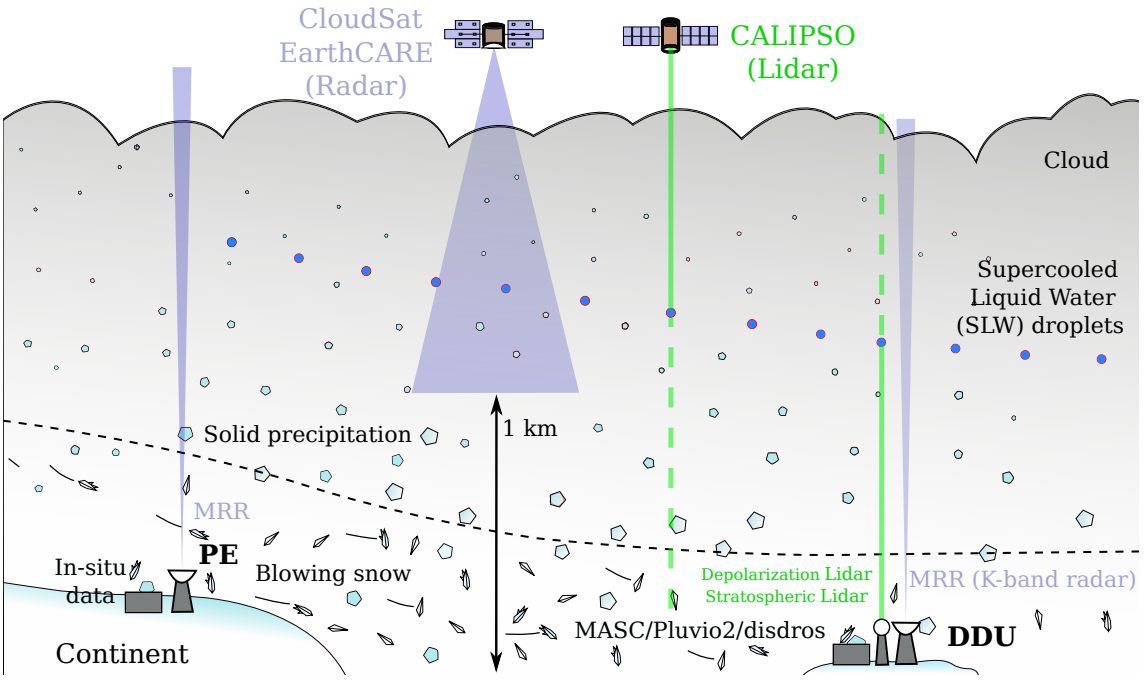

Figure 1.6: Diagram of Antarctic precipitation observation at DDU (coast of Adelie Land) and PE (inland of Dronning Maud Land). The distances in this diagram are not at scale.

1.4.1.3 Col de Porte station (CDP)

The research station Col de Porte (CDP) lies among the few sites displaying a large suite of measurements on the physical properties of snow and their relationship with the meteorological and wider environmental conditions. CDP is located at 1325 m a.s.l. altitude in the Chartreuse mountain range, close to Grenoble, France (45°18'N, 5°46' E). This station is an experimental site for the World Meteorological Organization Solid Precipitation Inter-Comparison Experiment (WMO-SPICE) aiming to compare manual and automated methods for snow precipitation and observations of snow on the ground (height and snow water equivalent) (Morin et al., 2013). See in Figure 1.7 the distribution of snow measuring instruments located at CDP during winter.

1.4.2 Instruments and data

- Micro rain radar: DDU, PE and CDP are equipped with a K-band vertically pointing MRR-2 manufactured by METEK, deployed with the aim of long-term monitoring of precipitation at DDU and PE respectively. Measurements at DDU are continuously collected since November 2015 (Grazioli et al.,

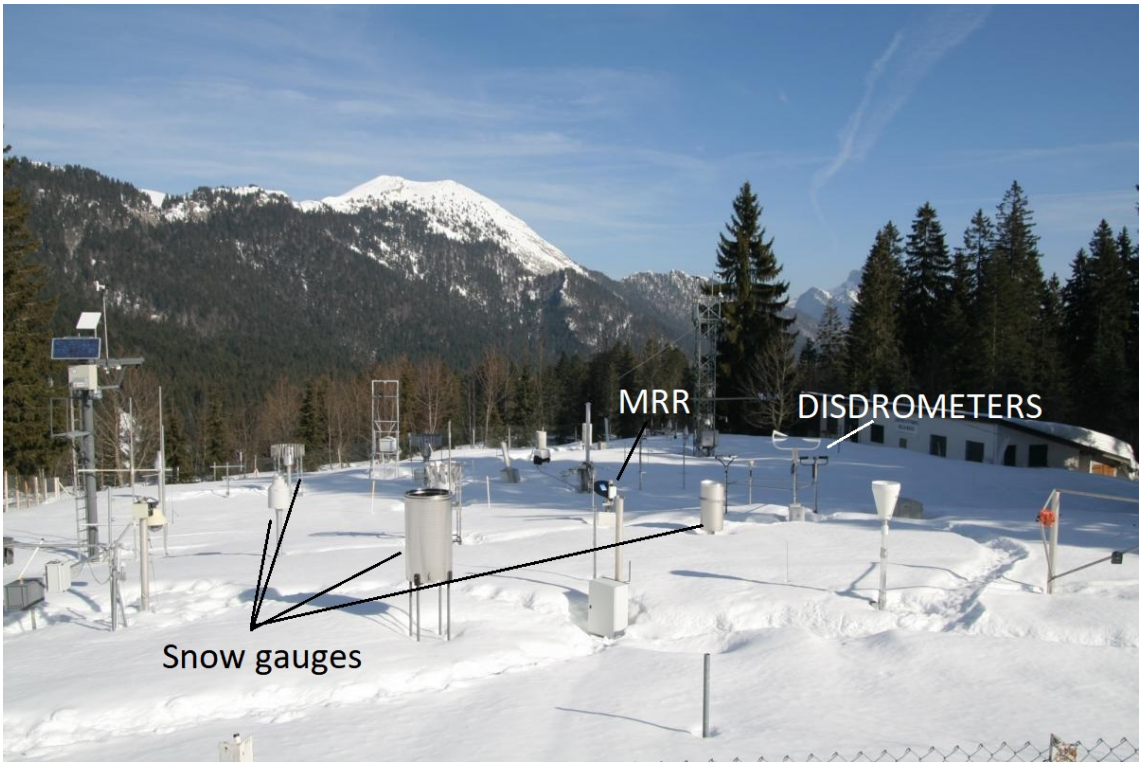

Figure 1.7: Alpine precipitation observation at CDP (French Alps). Source: SPICE (2019).

2017a), while at PE in-situ observations are carried out mainly during summer campaigns between 2010 and 2016, including one full year of measurements in 2012 (Gorodetskaya et al., 2015; Souverijns et al., 2017). In this study, two full years of data at DDU and all the observations at PE are used for the analysis. For the case CDP only one winter season was available.

MRR is a frequency-modulated continuous-wave (FMCW) system with low requirement of energy (small transmitter power: 50 mW) and of supervision during operation time (Peters et al., 2005), which makes this instrument suitable for monitoring remote locations with minimum logistic support (Gorodetskaya et al., 2015; Grazioli et al., 2017a).

The two radar systems in Antarctica use the same vertical (100 m) and temporal (1 min) resolutions, as well as the same number of range gates (31 up to 3 km) and of Doppler velocity intervals (64 between 0 and 12 m s^{-1}), while the MRR in the Alpine region was configured with a different vertical resolution (75 m). More details of the configuration of MRR and the complementary instrumentation for DDU are described by Grazioli et al. (2017a) and Genthon et al. (2018), and for PE by Gorodetskaya et al. (2015) and Souverijns

et al. (2018b). The MRR at DDU is deployed inside a radome to protect the instrument from the inclement Antarctic conditions in Adélie Land, and the MRR at PE and CDP had no radome, However this does not presented a problem because the weather conditions are not as harsh as at DDU. After post-processing, the sensitivity of MRR ranges between -14 and -8 dBZ depending of the height level (Maahn and Kollias, 2012). At DDU, the attenuation due to the radome (see Grazioli et al. (2017a)) must however be taken into account and leads to a lower sensitivity. The effect of the radome on the MRR at DDU was evaluated and corrected by Grazioli et al. (2017a) using a co-located X-band MXPol radar system. The comparison of both radar reflectivity observations showed that the radome produces an average attenuation of 6 dB in the data. A more recent analysis, using a second MRR at DDU deployed outside of the radome, confirms this estimate of the radome attenuation.

- Lidar: A single-wavelength elastic lidar with depolarization capability was designed by the Laboratory of Environmental Remote Sensing (LTE) at the Ecole Polytehnique Fédérale de Lausanne (EPFL), in the framework of the project APRES3 (Antarctic Precipitation Remote Sensing from Surface and Space) with support by CNES (program EECLAT). This instrument was deployed at DDU during the austral summer campaign of 2016-2017 at 70 m a.s.l., in a shelter located in the top of the Petrel Island.

  The lidar system transmits a linearly polarized laser beam at the wavelength of 532 nm, and the detection system measures the two components of the backscattered light using two photomultipliers (PMT) for the parallel (separated into two channels of 90 and 10% of the signal to detect saturation) and another PMT measures the perpendicular signal (See scheme of the lidar in Figure 1.8). The temporal resolution of the acquisition system is 6 profiles per minutes and the vertical resolution is 3.8 m. To reduce the noise, the vertical profiles were integrated in time and height, with a final temporal and vertical resolutions of 10 min and 23 m, respectively.

- Radio soundings: Daily radio soundings are carried out permanently at 00 UTC at DDU station by MeteoFrance since 1956, while at PE only summer radio soundings are available since 2014, collected at 12 UTC by the Royal Meteorological Institute of Belgium. In this work, we use vertical profiles of air temperature and relative humidity to characterize different precipitation

types and seasons (only summer at PE), corresponding to simultaneous observations of radio soundings and MRR. Radio soundings were also used to characterize the molecular volume backscattering at DDU, for lidar calibration purposes. At CDP, no radio soundings were available during the period MRR observations.

- All mentioned measurements are complemented with disdrometer information, automatic weather stations, snow gauges (in all stations) and Multi-Angle Snowflake Camera (only DDU). These observations were used to explore and better understand the precipitation observed at each station, however these data are not presented in detail in this dissertation.

All these datasets available for the present study represent a unique source of information about precipitation from a multi-instrumental setting, with different strengths and limitations that provide a great opportunity to take advantage of their synergy for the study of solid precipitation and clouds in complex environments, such is the case of Antarctic and Alpine regions.

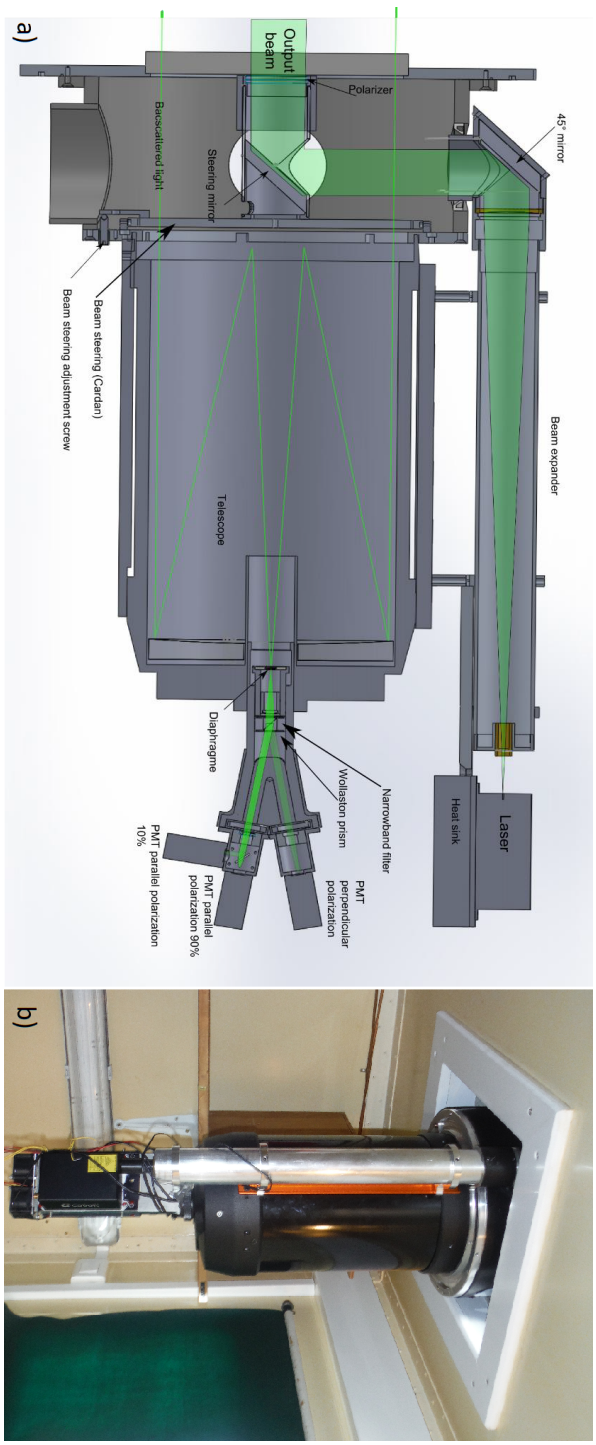

Figure 1.8: Lidar system composed by a power transmission sub-system (Laser source, beam expender mirrors and polarizer) and a detection sub-system (telescope, diaphragm, narrow band filter (532-nm), Wollaston prism and photomultipliers).

Chapter 2

Cloud and precipitation particle classification using lidar, East Antarctica

Abstract

Mixed-phase clouds (i.e., systems composed of supercooled liquid water drops, ice crystals and water vapor) are widely distributed in the Earth troposphere, covering all latitudes. They play an important role in the formation of precipitation and in the radiative balance, both at regional and global scales. In the last decades, with the help of lidar observation techniques, researchers have been able to monitor Mixed-phase clouds in different environments. Despite these efforts, there is still a great challenge to understand mixed-phase clouds and the associated physical processes, such as in the case of precipitation in Antarctica, where observations are still scarce. The lack of data makes it difficult to represent mixed phase clouds and in particular the presence of supercooled liquid water in numerical weather models and in climate models. Recently a single-wavelength lidar, with depolarization capability, was deployed at the Dumont d'Urville station on the coast of East Antarctica in February 2017 to characterize tropospheric clouds and precipitation. Measurements from an automatic weather station, observations of micro rain radar, daily radio soundings, among other information are also collected at the station. In the present work, the vertical distribution of supercooled liquid water clouds is analyzed using an automatic cloud detection method, combined with a k-means clustering approach for clouds and precipitation hydrometeor classification. Three applications of the classi-

fication were analyzed in this study: the occurrence of clouds and supercooled liquid layers; its vertical distribution; and the comparison with a satellite-derived classification. Results show a stable occurrence of supercooled liquid water clouds along the year, concentrated mainly between 1500 and 2500 m above sea level. When only cloud profiles are analyzed, the main hydrometeor class is 3-D (randomly oriented) ice, dominant in the upper part of the profiles, while 2-D (planar/oriented) ice are observed in the lowest elevations. For precipitation profiles, 2-D ice are present in all altitudes and 3-D ice are mainly observed near the surface. Regarding the comparison of ground-based and satellite-derived classifications, the vertical pattern of supercooled liquid water is consistent between both observation systems and the lidar at DDU provides important information of the variability of precipitation and cloud composition in the near surface layers.

2.1 Introduction

Aerosols and clouds are key players in the climate system, because of their importance in the radiative budget of the Earth, driving heat and water fluxes over a large range of scales (e.g. Lohmann et al., 2016). Because of their large spatial and temporal variability associated to atmospheric dynamics, the observation and monitoring of aerosols and clouds in the atmosphere is challenging (Baker and Peter, 2008). Remote sensing, and lidar in particular, offers ways to monitor aerosols and clouds at relevant spatial and temporal scales (e.g. Ackerman and Stokes, 2003; Winker et al., 2010).

Ground-based networks of lidar systems have been deployed in various regions of the world, such as the micro-pulse lidar network, called MPL-net, in the USA and other regions (Welton et al., 2001; Lewis et al., 2016), and the European Aerosol Research Lidar Network, called EARLINET and founded in 2000 (Pappalardo et al., 2014). To complement such ground-based systems and to improve the spatial coverage to be able to monitor the (nearly) entire atmosphere, spatial lidar systems have also been developed. CALIOP was the first space-borne polarization lidar system (Winker et al., 2010), on-board the Cloud-Aerosol Lidar and Infrared Pathfinder Satellite Observations (CALIPSO).

Lidar has found many applications in polar regions. Polar stratospheric clouds over the South Pole were studied using (elastic) lidar measurements collected at McMurdo (Gobbi, 1995) and later a climatology of this type of clouds in the Arctic and Antarctic regions was derived from CALIOP data (Pitts et al., 2018). Some

important properties of blowing snow (e.g. frequency of occurrence, depth) over Antarctica were characterized using CALIOP (Palm et al., 2018a,b). Not directly related to aerosols and clouds, lidar information has also proven useful to investigate glacier motion (e.g. Telling et al., 2017), calving (e.g. Podgórski et al., 2018) or estimation of topography (e.g. Pope et al., 2013).

More closely related to the scientific domain of interest of the present study, lidar has been crucial to better understand and characterize mixed-phase clouds. Depending on the type of available lidar information, various approaches have been proposed to identify supercooled liquid water (SLW) droplets, a key component of mixed-phase clouds: based on backscattering only (Hogan et al., 2004), on depolarization ratio (Sassen, 1991), on a combination of lidar and passive visible imagery (Hu et al., 2010) or of lidar and cloud radar (e.g. DARDAR Delanoë and Hogan, 2010; Cazenave et al., 2019). Further to the identification of SLW droplets in the atmosphere, classification techniques have been developed to automatically assign a type/label to lidar observations. For polarization lidar, Yoshida et al. (2010) proposed a technique to identify the different types of particles seen by the lidar in the two-dimensional space formed by the optical thickness and the depolarization ratio. Taking advantage of multi-wavelength-polarization lidar systems, Baars et al. (2017) proposed a typing method to characterize aerosol and cloud particles.

Mixed-phase clouds are of primary importance for radiative transfer and energy balance at the surface in polar regions, particularly in the Arctic (e.g. Korokev et al., 2017; Wendisch et al., 2019). The radar-lidar synergistic product DARDAR was used to characterize the variability in space and time (e.g. Mioche et al., 2015) and the microphysical properties (e.g. Mioche et al., 2017) of mixed-phase clouds in the Arctic region. In Antarctica, Del Guasta et al. (1993) characterized the cloud properties (base height, depth, phase, characteristic temperature) at the Dumont d'Urville station on the coast of Adélie Land using a polarization lidar. At the South Pole station, Lawson and Gettelman (2014) showed that mixed-phase clouds are more frequent than expected at such a high-latitude region using lidar observations. More recently, Listowski et al. (2019) characterized the geographical and seasonal variability of mixed-phase and supercooled liquid clouds over Antarctica, from the DARDAR product.

The existing datasets however correspond to limited spatial and temporal coverages, and satellite derived products are not reliable close to the Earth surface. Hence, there is a need for reference observations relevant to complement existing datasets/instruments and evaluate satellite products, in particular in poorly moni-

tored regions like Antarctica. In this study, a new lidar dataset collected in coastal Antarctica at the Dumont d'Urville station, is presented, together with innovative processing and classification approaches to derive relevant information about cloud particles in various seasons.

This Chapter is organized as follows: the material and methods are presented in Section 2.2; the processing technique is detailed in Section 2.3, while the hydrometeor detection and classification approach is presented in Sections 2.4 and 2.5; the derived statistics for different months are then analyzed in Section 2.6, and a summary and conclusions are provided in Section 2.7.

2.2 Materials and Methods

2.2.1 Lidar

A single-wavelength elastic lidar with depolarization capability was deployed at DDU during the austral summer campaign of 2016-2017 at 70 m a.s.l., in a shelter located in the top of the Petrel Island. The characteristics of the lidar used in this study and the period of observation are detailed in Subsection 1.4.2.

2.2.2 Micro Rain Radar

A K-band vertically pointing MRR-2 manufactured by METEK, was deployed at DDU, with the aim of long-term monitoring of precipitation. Measurements are continuously collected since November 2015 and were available during all the period of the present study. Observations from MRR were used to determine occurrence of near surface precipitation at DDU, which were used to complement the automatic method of hydrometeor detection (more details in subsection 1.4.2).

2.2.3 Radio soundings

We used vertical profiles of air temperature T_a (in K) and atmospheric pressure P_a (in hPa) to model the vertical profiles of volume molecular backscatter β_m and extinction σ_m coefficients for lidar calibration purposes. T_a and P_a were obtained from daily radio soundings, which are launched everyday at 00 UTC at DDU station by MeteoFrance. The following expressions are used to estimate β_m and α_m using

sounding data and Rayleigh scattering theory:

$$\hat{\beta}_m(z) = \frac{\hat{\alpha}(z)}{S_m} = \frac{\hat{\alpha}(z)}{\frac{8\pi}{3} k_{bw}} \tag{2.1}$$

and

$$\hat{\alpha}_m(z) = \frac{N_A P_a(z)}{R_a T_a(z)} Q_s \tag{2.2}$$

where $\hat{\beta}$, $\hat{\alpha}$, P_a and T_a are expressed as function of the altitude of the radio sounding z; S_m is the Rayleigh extinction-to-backscattering ratio; N_A is the Avogadro's number ($6.02214 \cdot 10^{23}$ mol^{-1}); R_a is the gas constant (8.314472 J K^{-1} mol^{-1}); Q_s is the 532-nm total Rayleigh scattering cross-section per molecule ($5.167 \cdot 10^{-27}$ cm^2); and k_{bw} represents the dispersion of the refractive index and the King correction factor of air for the working wavelength (Bucholtz, 1995; Powell et al., 2009). In Section 2.3, more details about lidar processing are provided.

2.3 Lidar Processing

2.3.1 Background correction

External sources of power (e.g. sunlight) or the dark current (i.e. flow of power in the detector system in the absence of signal or background light) induce an offset signal, which must be removed from the raw received power, for proper calibration of the data. Frequently, the offset is corrected by a straightforward background subtraction, using the far-range signal as reference for background light, where signal due to particle and molecular backscattering is assumed to be negligible (Kovalev and Eichinger, 2004; Cao et al., 2013). However, if the signal is strong and the atmosphere presents a low optical depth, remaining signal from molecular backscattering can still be present in the far-range of the lidar, especially when lidar range is not large enough for the complete extinction of the signal. Under these conditions, the estimation of the background noise level using the average signal from the upper part of the profiles leads to an overcorrection of the raw signal.

In our lidar data, we have found that during clear sky nights or with the presence of optically thin clouds, the signal in the upper part of the profiles shows a strong dependence with the range, suggesting that molecular backscattering still plays an important role. Figure 2.1a shows two cases of raw signal at high altitude, when background noise is dominated by thermal/electric noise from the detector lidar

system and background noise from sky (red line); and when the remaining signal is strongly dependent on the range (blue line). The first case corresponds to a night during a precipitation event, where signal is completely attenuated along the first 2 kilometers of altitude and the second case is a clear-sky night. The simple subtraction of the background noise level (e.g. average of the raw signal at the upper 1 km, $Bs_{\overline{9-10km}}$) can be applied to the vertical profile of the first case. In the second case, $Bs_{\overline{9-10km}}$ overestimates the background level, due to the bias produced by the remaining signal.

We propose the following method to estimate in a simple way the background level from signal that contains significant contribution of molecular backscattering in the upper part of the profile. Assuming a cloud and aerosol free region ($\beta_a = 0$) from a sufficiently high altitude r_{cf} and rewriting the lidar equation as function of the molecular backscatter and extinction coefficient (β_m and σ_m), we obtain:

$$P_{cf}(r) = \frac{C}{r^2}\beta_m(r)exp\left[-2\int_0^{r_{cf}}\sigma(R)dR\right]exp\left[-2\int_{r_{cf}}^{r}\sigma_m(R)dR\right] + Bs, \forall r > r_{cf} \tag{2.3}$$

where P_{cf} is the received power in the upper part of the profiles; the first exponential factor represents the total attenuation due to atmosphere from the instrument level to the r_{cf} and the second exponential factor is molecular attenuation. The notation of the integrals can be simplified and the known terms can be grouped to obtain a lineal relationship between molecular scattering and the received power in the upper part of the atmosphere:

$$P_{cf}(r) = C \cdot T^2 \,|_0^{r_{cf}} \left(\frac{\beta_m(r)T_m^2 \,|_{r_{cf}}^{r}}{r^2}\right) + Bs, \forall r > r_{cf} \tag{2.4}$$

The unknown parameters in the right-hand side of the linear equation correspond to the slope $\left(C \cdot T^2 \,|_0^{r_{cf}}\right)$ and intercept (Bs), while the independent and known variable is $\left(\beta_m(r)T_m^2 \,|_{r_{cf}}^{r}\, r^{-2}\right)$, derived from radio soundings. Fitting a line using least square method to this equation allows to get the value of the background signal (see example in Figure 2.2). Figure 2.1b shows the respective range-background-corrected signals $\left((P(r) - Bs)r^2\right)$ for the two examples presented before. The case with strong signal and rapid attenuation due to precipitation below 2 km, shows no significant differences between the two methods to estimate background level, while in the second case where remaining signal was present in the top of the profiles, significant differences are observed at the highest 4 km. The signal corrected by

the simple average of the signal at the top of the profile, describes an anomalous patterns compared with a profiles of clear sky conditions, which corresponds to a positive bias in the background level estimation (Kovalev and Eichinger, 2004).

2.3.2 Signal-to-Noise ratio

The signal-to-noise ratio (SNR) was used to remove low quality data from the study. In literature, several ways to compute signal to noise ratio have been proposed (e.g. Wu et al., 2006; Liu et al., 2009; Cheng et al., 2017). In most of these expressions, SNR corresponds to the ratio of the signal corrected by the background and the signal affected by the background and electronic noise, as it is shown in the following equation:

$$SNR = \frac{N_s}{[N_s + N_b + N_d]}, \tag{2.5}$$

where SNR is the signal-to-noise ratio (unitless), N_s is the received signal due to backscattering, N_b is the signal due to background light, and N_d is the signal due to dark current in the photomultiplier.

2.3.3 Calibration parameters

After estimating the contribution of the background, the system constant is obtained using clear-sky night profiles as a reference, at an altitude where it is assumed that $\beta = \beta_m$ and there is a complete overlapping between telescope and laser ($O = 1$). From the lidar equation, the system constant for both polarizations can be cleared, as it is shown in the following equation:

$$C_{\parallel,\perp} = \frac{P_{\parallel,\perp}(r) r^2}{\beta_{m\parallel,\perp} T_m^2} \tag{2.6}$$

where $P_{\parallel,\perp}$ are the background corrected received signals for the parallel and perpendicular channels. The atmospheric transmission due to molecules is obtained from extinction coefficient derived using radio soundings and the $\beta_{m\parallel,\perp}$ are estimated using the following equations:

$$\beta_{m,\parallel}(r) = \frac{1}{1+\delta_m}\beta_m \tag{2.7}$$

and

$$\beta_{m,\perp}(r) = \frac{\delta_m}{1+\delta_m}\beta_m \tag{2.8}$$

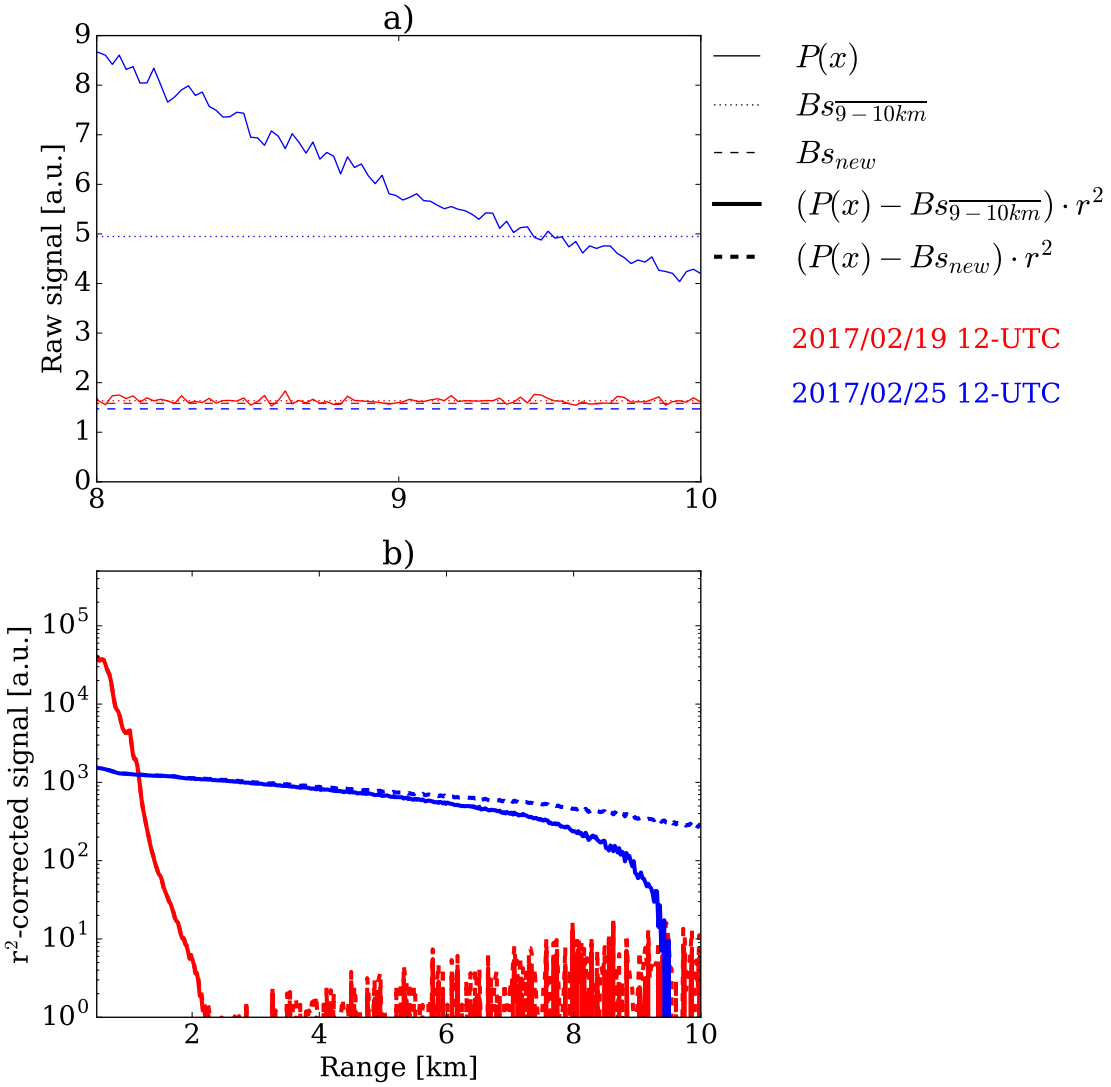

Figure 2.1: Examples of far-range raw signal used to determine background contributions (a) and range-background-corrected signals (b) for two different cases on 2017/02/19 and 2017/02/25 at 12-UTC. In the case at 19th February the far-range signal produced by backscattering is negligibly due to strong attenuation by optically thick clouds and precipitation at lower altitudes. The case of 25th February corresponds to a profile of clear sky night, with remaining lidar signal at the top of the profile.

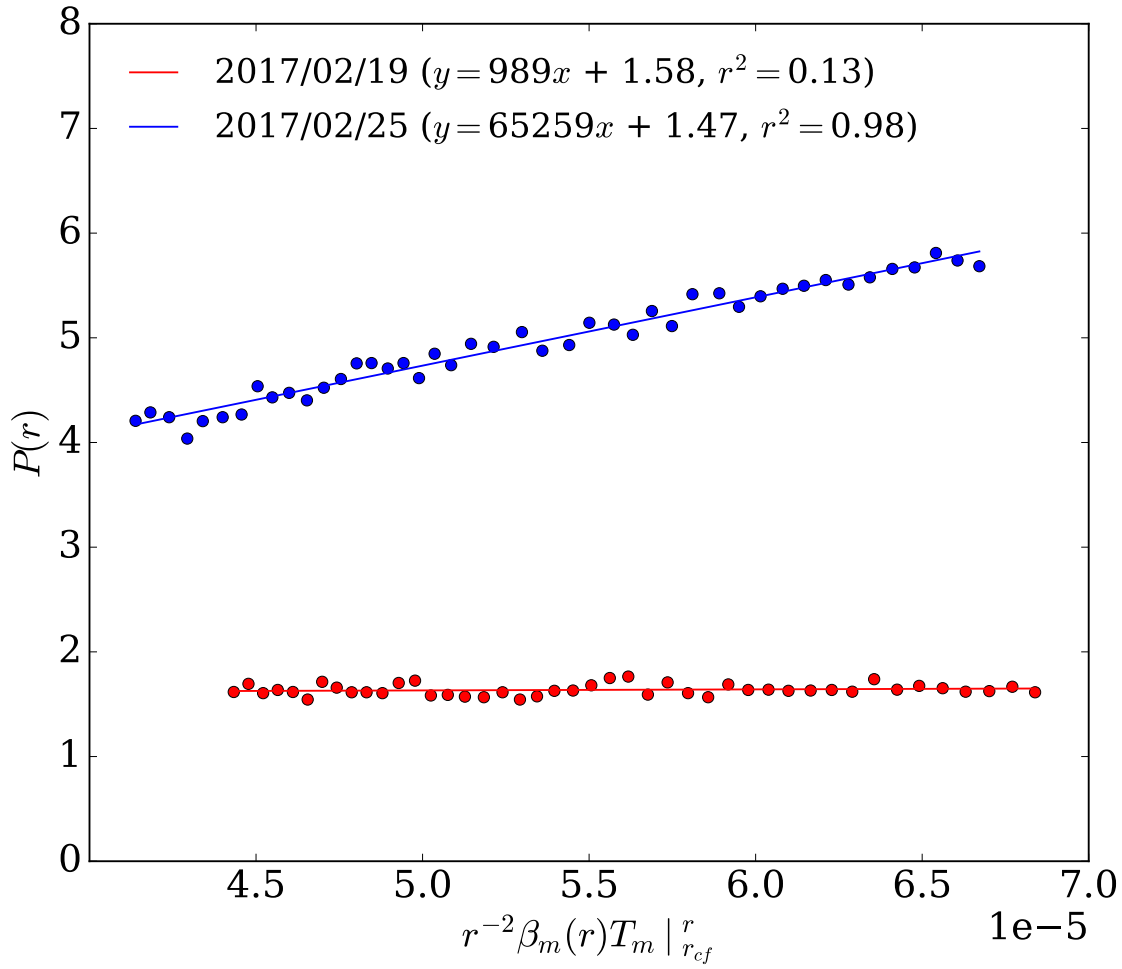

Figure 2.2: Estimation of the background signal using the proposed method for two different nights. Blue dots correspond to the signal in the far-range of a clear sky night, while red dots to a cloudy night near to the surface. The respective lines fit the received power versus the attenuated backscatter coefficient to the obtain the background signal (the intercept of the regression).

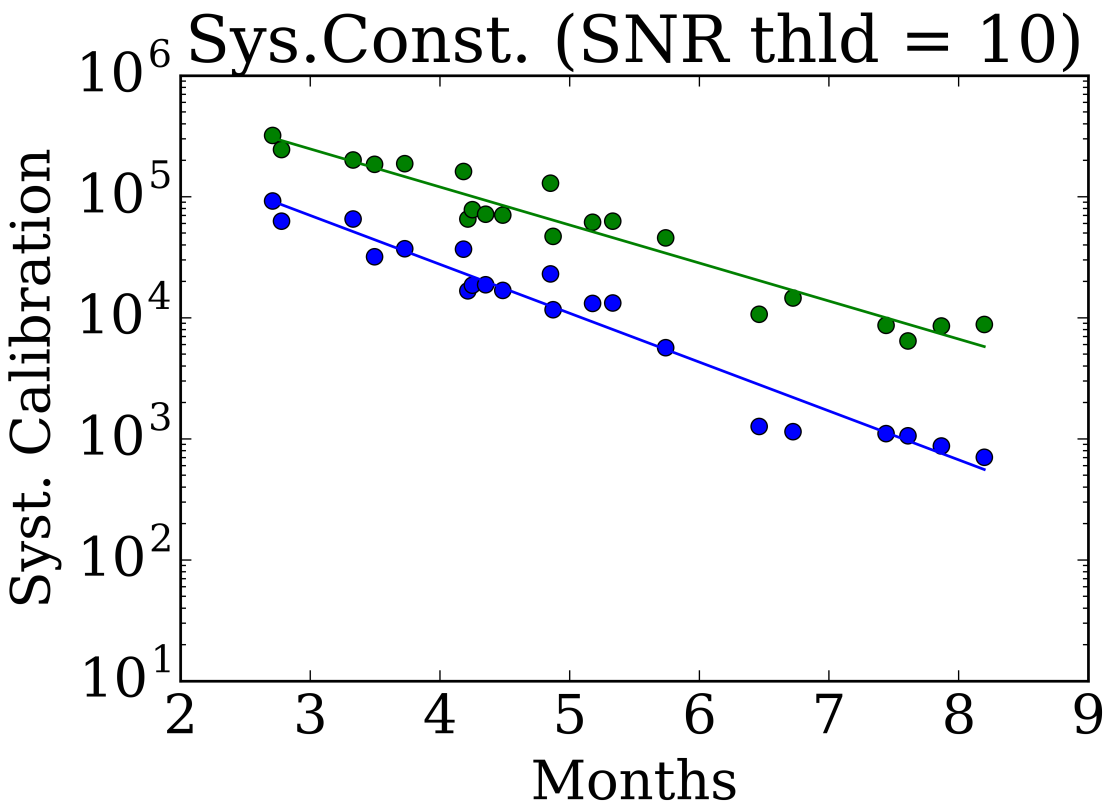

Figure 2.3: Lidar calibration constant between February and August 2017. Blue and green dots corresponds to the system calibration using clear sky night profiles, for the parallel and perpendicular polarizations respectively. Lines represents a linear fitting the each set of points used to estimate the calibration parameters along the study period.

where δ_m is the volume molecular depolarization equal to 0.00366 for Rayleigh scattering at $\lambda = 532$ nm (Young, 1981; Powell et al., 2009).

The operation of the lidar system continuously over a full year, caused wear of the useful life of the laser source, which results in a progressive decrease in the amount of transmitted energy. Additionally, misalignment of the laser with respect to the telescope FOV along the year, contributes to the lost of power in the upper part of the profiles and the decreasing of the SNR. In the Figure 2.3 it is possible to observe the decrease of calibration constant for both, the parallel and perpendicular system.

2.4 Hydrometeor detection

In order to separate cloud and precipitation particles from aerosols and clear sky lidar observations, an automatic approach was used, based on the signal simplification for

single-channel lidar proposed by Gong et al. (2011). This method uses an improved Douglas-Peucker (DP) algorithm to simplify the range-corrected signal ($S = r^2P(r)$) into a smaller number of points that represent the limits of homogeneous layers in a given vertical profile, previously de-noised using a low-pass filter. Gong et al. (2011) used the noise of the signal to define the tolerance of the DP algorithm, which demonstrated to be useful to detect clouds when there is a low signal to noise ratio. After the signal simplification, clouds are detected based on the slope of S. A mark of cloud base is assigned when the slope of S between two consecutive points is positive. The respective cloud top is marked when the slope of S is negative again and the value of the S is lower than the cloud base. To deal with the underestimation of the cloud top, the absolute value of the slope of S must be lower than the slopes of neighboring clear sky layers at lower altitude than the point in evaluation. The molecular backscatter coefficient derived from radio soundings was used to determine the slope of the clear-sky near to the analyzed point. Once the top of the cloud is marked, a new cloud base is search in the highest points, repeating the process. When all cloud layers are marked, the ratio between the signal peak of the layer and the signal at the cloud base is used to decide whether or not the layer is a cloud.

This method has shown a good performance detecting clouds, but it presents problems when there is precipitation at the surface level, because the positive slope is not present if the strongest lidar signal is located at the lowest available range of the bin. To deal with this problem, the occurrence of precipitation near to the surface level was defined using a co-located micro rain radar (MRR), which is used to monitor continuously precipitation between 300m and 3km above surface level at DDU (see more in Genthon et al. (2018)). When there was precipitation detected at the lowest available range gate by the MRR, the lowest point of the simplified signal was automatically defined as the base of a precipitation layer. See an example of cloud and precipitation detection in Figure 2.4.

2.5 Hydrometeor classification

Once cloud and precipitation particles were identified, an automatic classification of the hydrometeor phase was performed using information from depolarization ratio δ, the attenuated backscattering and the extinction of the signal. Yoshida et al. (2010) (hereafter Y2010) introduced a magnitude proportional to the optical depth between two consecutive homogeneous layers, denoted by χ, which is defined by the

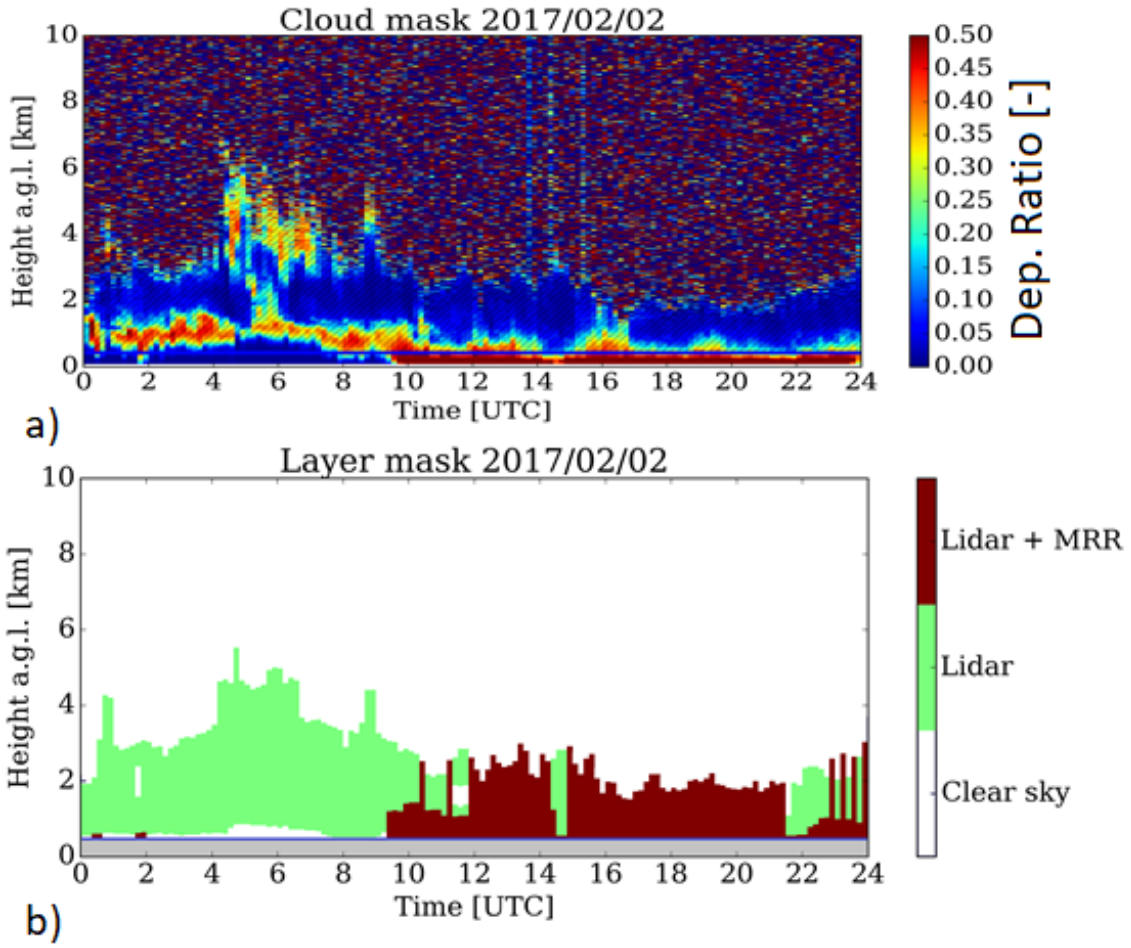

Figure 2.4: Cloud and precipitation detection using lidar + MRR information. Panel a shows the depolarization ratio for the 2nd of February of 2017, where dashed areas represent the presence of hydrometeors (clouds or precipitation). The panel b shows the detail of the used detection approach. Green areas are particles detected only using lidar information, red areas were detected using lidar and MRR information near to the surface. Within the white areas no particles were detected and gray region below 300 m was removed during the post processing.

following logarithmic expression:

$$\chi(R_i) = log_{10}\left[\frac{\beta'(R_i)}{\beta'(R_{i+1})}\right], \tag{2.9}$$

where β' is the attenuated backscatter ratio and R_i and R_{i+1} correspond to the elevation of two consecutive range gates.

Using the joint distribution between δ and χ, the method proposed by Y2010 identifies characteristic features, which allow to discriminate solid and liquid particles using lidar observations from space (CALIPSO). In presence of ice particle, lidar signal shows moderate extinction and large values of depolarization, while for water particles, it presents strong attenuation and a lower range depolarization. In addition, this method also separates ice into randomly oriented particles (3D-ice) and horizontally oriented crystals (2D-ice), using a low δ threshold ($\delta < 0.03\%$) considering that specular reflection of oriented ice particles, such as plates, produces near-zero depolarization (Del Guasta et al., 2006; van Diedenhoven, 2017). Figure 3 in Y2010 shows an example of the joint distribution of δ and χ for a given precipitation event, when layers of supercooled liquid water were observed. In that figure, the limits proposed by Y2010 are over-posed on the diagram, where the regions corresponding to 2D and 3D-ice, liquid particles associated to SLW because of the low temperatures, and two unknown regions (Unk1 and Unk2) are observed. After a spatial filter (horizontal and vertical), Unk1 and Unk2 can be classified in one of the other categories. The distribution of the data in our example shows a similar pattern to the case of Y2010 when liquid particles are observed and in general terms an agreement between the limit that separates 3D ice from SWL particles. Despite these concordances, the large amount of observation classified as unknown produces great uncertainty in the final classification, even after performing a spatio-temporal filter (vertical and time).

For this reason, in this study we proposed an automatic method of classification of precipitation and cloud hydrometeors, combining Y2010 with a cluster analysis based on k-means algorithm. In this new approach, initial regions corresponding to 3D-ice and SLW particles are identified from 8 clusters generated from the three-dimensional space created by δ, χ and the parallel backscatter ratio ($\beta'_{\parallel}$). This number of clusters was selected because it was the minimum value that allows to separate correctly the main branches observed in the distribution. A third dimension was included to facilitate the discrimination of liquid water, based on the strong signal it produces on the lidar signal. The initial centroids in the cluster analysis are

estimated using the k-means++ method (Arthur and Vassilvitskii, 2007) over a full month of observation, in order to collect all possible types of particles. Clusters are computed dynamically in temporal window of 5 days and then clusters corresponding to SLW clouds (8 and 4) and to 3D-ice (3 and 7) are merged to generate a first classification. 2D-ice is identified using the same threshold than in Y2010. After a preliminary classification, a spatio-temporal filter of 2 by 2 is apply to each gate of the vertical profiles of 23 m of vertical resolution and 10 min of temporal resolution, where the center of the kernel takes the class with more frequency.

Figure 2.6 shows an example of the classification of lidar observations using the new method for the same dates of Figure 2.5. Figure 2.6a corresponds to the 8 clusters from two different angles of view and Figure 2.6b is the final classification. The use of the additional information provided by $\beta'_{\parallel}$ represents an important advantage, which allows to reduce observations without classification, especially for SLW.Figure 2.6 presents an example of the output classification, where the presence of layers of super-cooled liquid water are highlighted in light blue between 1 and 3 km of height.

2.6 Applications

The processing carried out on the lidar data presented in Section 2.3 and the application of the methods for detecting and classifying hydrometeors presented in Sections 2.4 and 2.5 made it possible to analyze the frequency of occurrence of clouds at DDU during 2017 as well as the vertical distribution of different hydrometeors types within the clouds. Below the analysis of the three applications using particle classification using lidar is presented and a comparison with a satellite-derived classification is performed.

2.6.1 Occurrence of clouds and SLW layers

Figure 2.8 shows the monthly values of the cloud fraction (CF) for all observed clouds as well as the relative fraction of SLW layers between February and December of 2017. For a given time step (as a reminder, time resolution is 10 min), the sky is considered cloudy as soon as at least one atmospheric layer (vertical resolution is 23 m) is cloudy. Clouds are present from 50 up to 70% of the time with a maximum in February (80%) and a minimum in October (45%). There is a slight decrease in the cloud fraction throughout the year. However, this trend cannot be due solely to

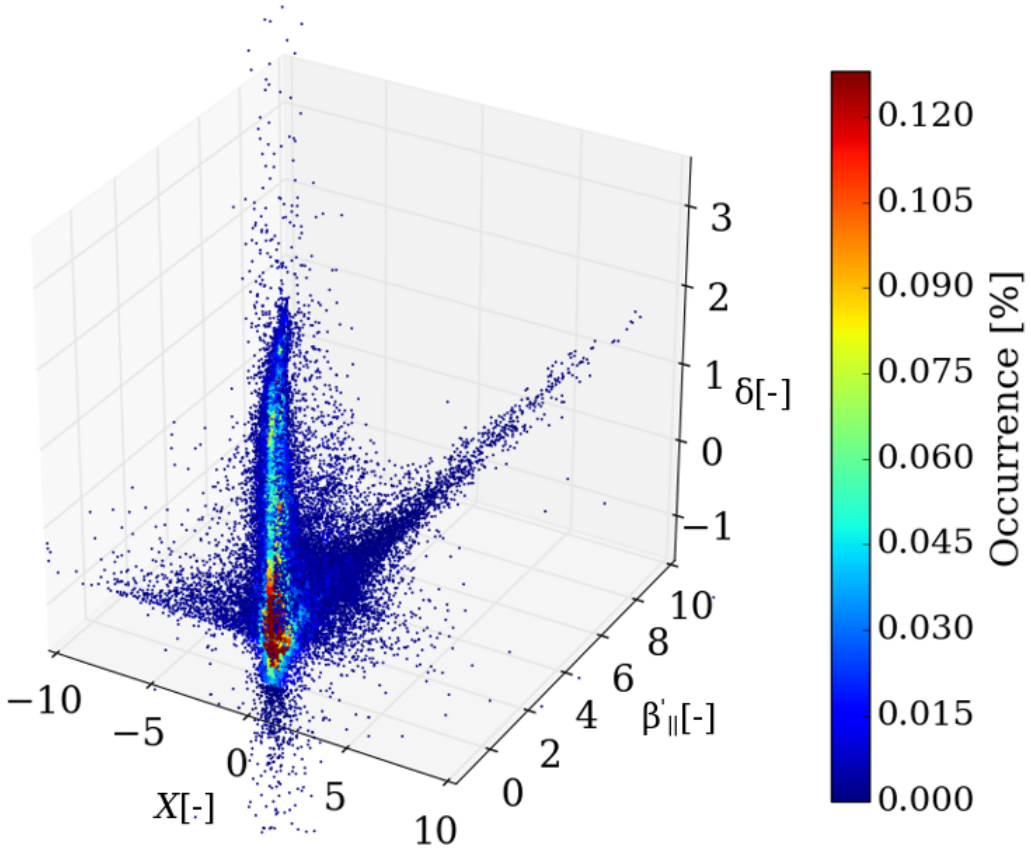

Figure 2.5: 3D histogram of cloud and precipitation particle on the χ, δ and $\beta_{\parallel}$ planes. The colors represent the occurrence frequency from observation.

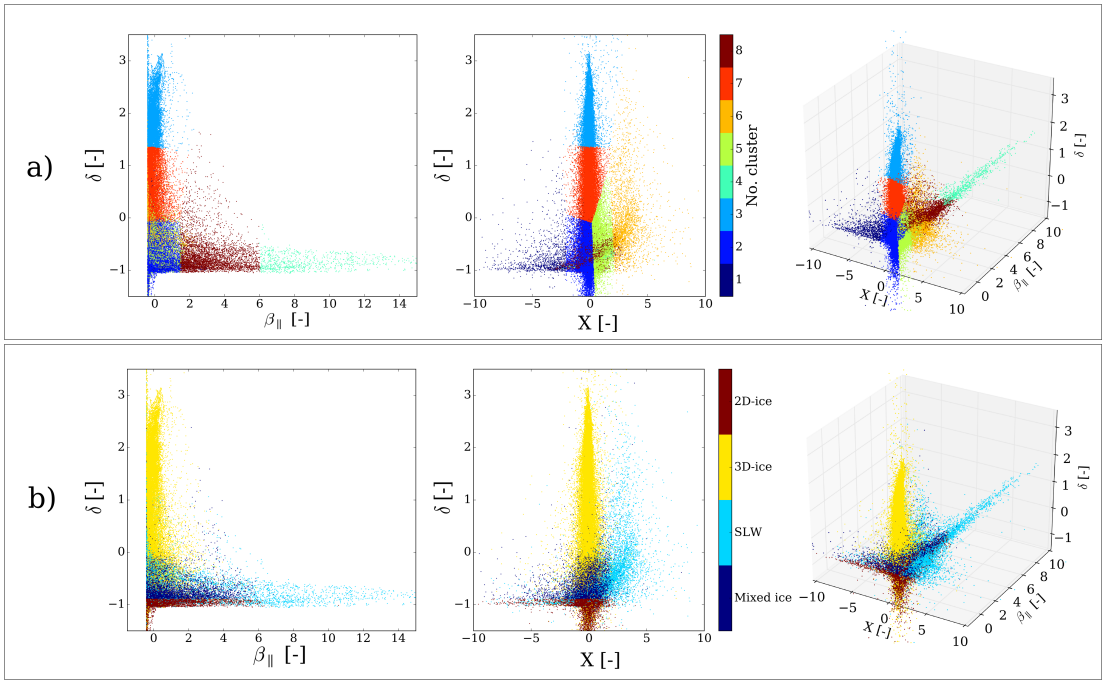

Figure 2.6: Cluster analysis and classification. The panel a shows 8 clusters, from different points of view, generated using k-means method, based on the three-dimensional space formed the depolarization ratio, the X variable and the parallel signal. In panel b, the final classification is displayed in the same space.

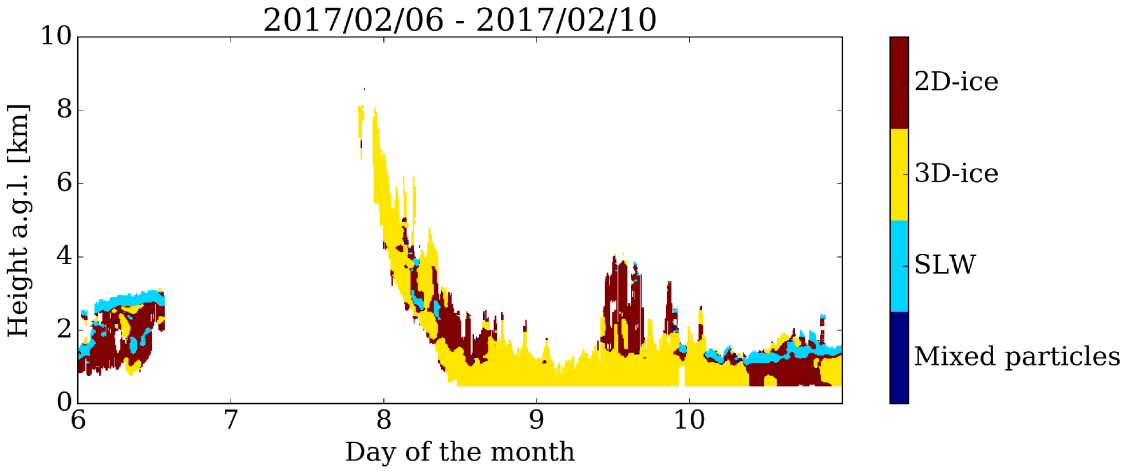

Figure 2.7: Classification of the vertical profiles displayed on a time versus height diagram.

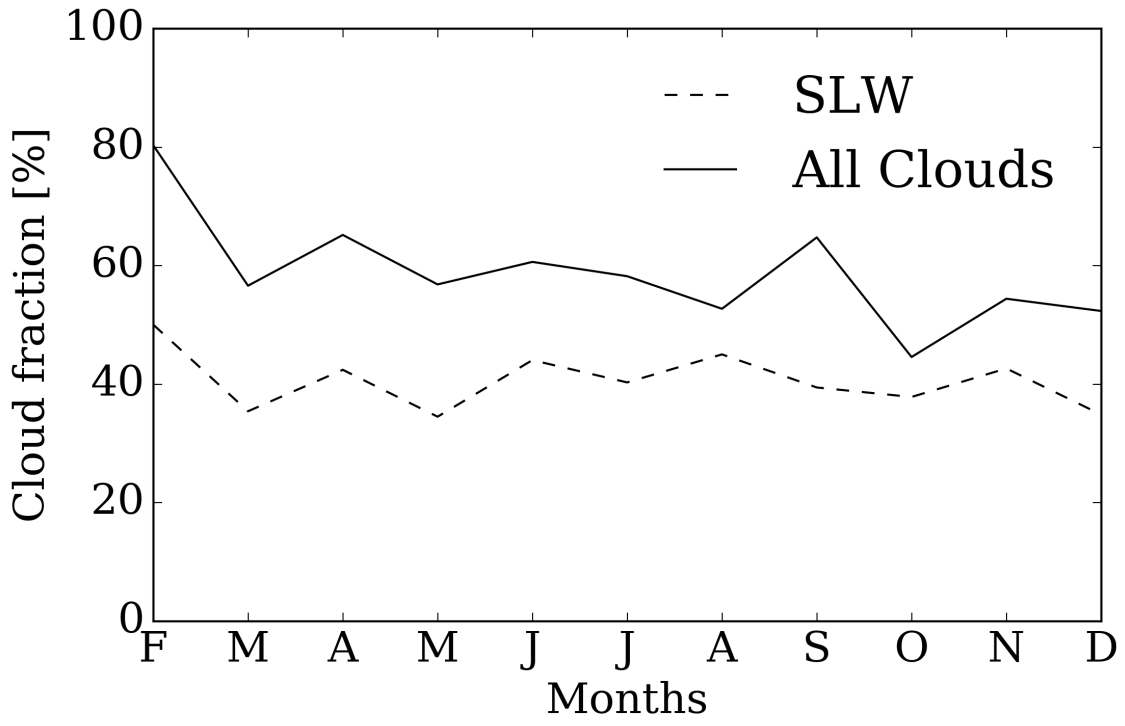

Figure 2.8: Monthly cloud fraction derived from Lidar profiles at DDU for SLW (dashed line) and all clouds (solid line).

a gradual loss of lidar sensitivity (mentioned in Section 2.4), as some increases in cloud fractions can be observed in April, September and November. The percentage of mixed-phase clouds in relation to all observed cloud is quite constant all along the year.

2.6.2 SLW vertical distribution

Figure 2.9 represents the monthly vertical distribution of clouds and the proportion of SLW clouds with respect to the total number of profiles ("absolute") and relative to the total number of clouds ("relative"). Fractions of SLW occurrence seem questionable above 6 km of altitude, in particular in June and September. Therefore, greater confidence should be given in the interpretation of the results for the first 6 kilometers (not greyed out on the figure). Furthermore, it was observed (not shown here) that during the last months of the year, the cloud fraction in the upper layer decreased dramatically and was even be zero beyond 4 km in October and November. This is probably due to the continuous loss of sensitivity of the lidar (mentioned in section 2.4) over the year, which affected first for the greatest distances (i.e. the highest altitudes) and then gradually contaminated lower altitudes during the last

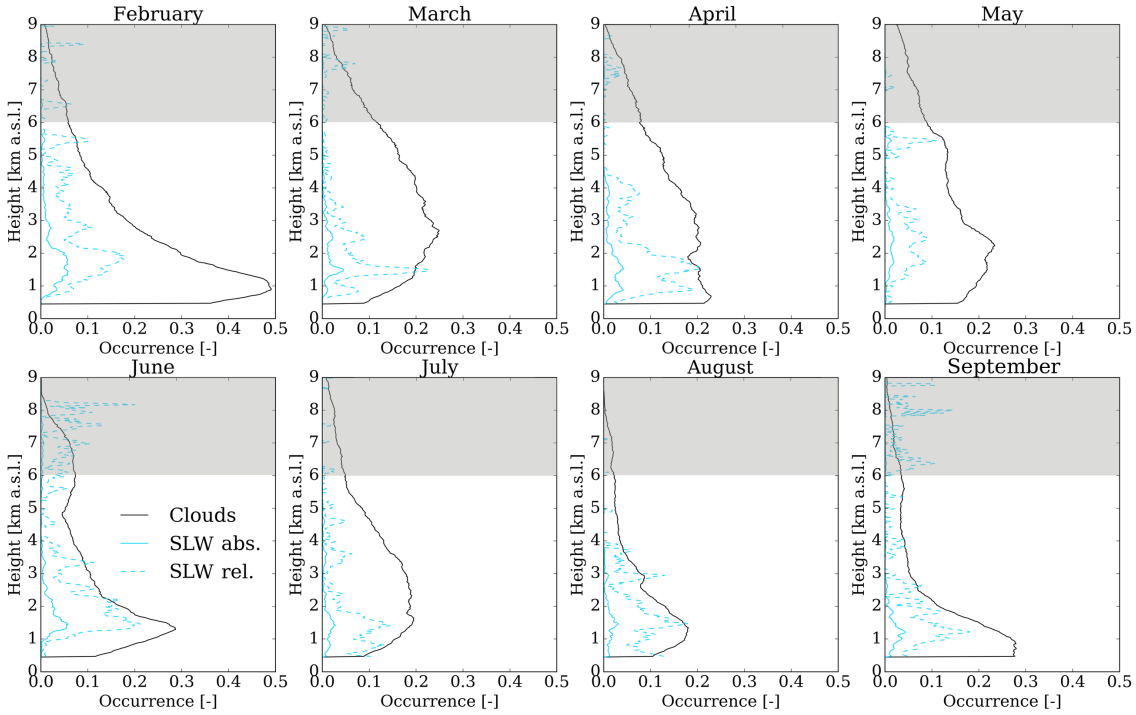

Figure 2.9: Monthly clouds occurrence per altitude derived from Lidar profiles for all Cloud (black) and SLW (cyan). dashed-cyan lines correspond to the SLW relative to the total cloud occurrence and the solid-cyan lines are the SLW respect to all the observations.

months. After an analysis of the frequency of SNR values as function of altitudes and months, it appears that until September SNR values above 10 dB are similarly present in all months and can be used at all altitudes. That is why the monthly vertical distribution of clouds shown on Figure 2.9 is restricted to the period between February and September, during which the data are reliable.

The vertical profiles of the cloud fraction show that the majority of this fraction is in the first few kilometers. Over the year, clouds are present for at least 10% time at any altitude below 4 km altitude. The vertical extension of clouds is slightly larger in the first months of the year that correspond to the southern hemisphere summer and autumn. The peak occurrence of cloud fraction is on average at 1500 m above sea level but this level can vary from one month to the next (up to about 2500 m in March and May). The peak is particularly pronounced in February and September. It is explained by both the presence of clouds but also the presence of more precipitations during these months at the lowest altitudes (a detailed partition is shown on Figures 2.10 and 2.11). Supercooled liquid water is observed all the year at different altitudes. It is mainly concentrated at altitudes of about 2000 m (from 1500 to 2500 depending on the month). The depth of the layer where this

supercooled liquid water appears tends to be greater during the southern summer. The amount of SLW bearing clouds is significant and can lead to riming. This information provided by lidar is also important to consider because of the different radiative effects caused by the presence of SLW droplets. The classification method proposed in Section 2.5 and applied to all available data makes it possible to establish a more detailed climatology than on Figure 2.9. Figures 2.10 and 2.11 represent respectively the monthly vertical distribution of clouds (resp. precipitation) and the proportion of SLW and ice clouds (resp. precipitation particles) with respect to the total number of profiles, and that, for clouds only profiles (Figures 2.10) or precipitation only (Figures 2.11). As far as the cloudy part is concerned, we can observe that most clouds are formed by 3D-ice particles (i.e. non-planar ice-only crystals), at all altitudes. Such ice crystals are dominating and even the only type in the upper part of the clouds. At lower altitudes, the clouds are more mixed, containing both 2D-ice, 3D-ice and, as previously indicated, SLW. The 2D-ice is detected up to about 5 km above sea level with a peak at around 2 km, slightly above the SLW peak. The respective proportion of 2D and 3D-ice in the lower part of the profiles changes during the year. It is more balanced in February than in any other month. The proportion of 3D-ice is preponderant even in the lower layers from April to August. Concerning the precipitation part (Figures 2.11), 3D-ice particles are the most common but concentrated in the very lowest levels. Precipitation of 2D-ice is observed at higher altitudes (up to 3 km in January and August, up to 2 km from March to July).

2.6.3 Comparison of ground-based and satellite-derived classifications

Comparison between the profiles obtained from ground-based lidars and a satellite based lidar is relevant to analyze the respective strengths and weaknesses of each source. However, this type of comparison is not trivial. Indeed, several elements must be taken into account. First of all, spatial sampling is very different: measurements collected at ground level correspond to vertical profiles over a fixed point at the Earth surface, while the one obtained from space is moving and therefore integrates vertical information all along the satellite track. Secondly, the time steps when both measurements are available simultaneously and at the same location are very rare. For our study, we mean by "same location" the area for which space-borne measurements are available at less than 100 km around DDU. In this area,

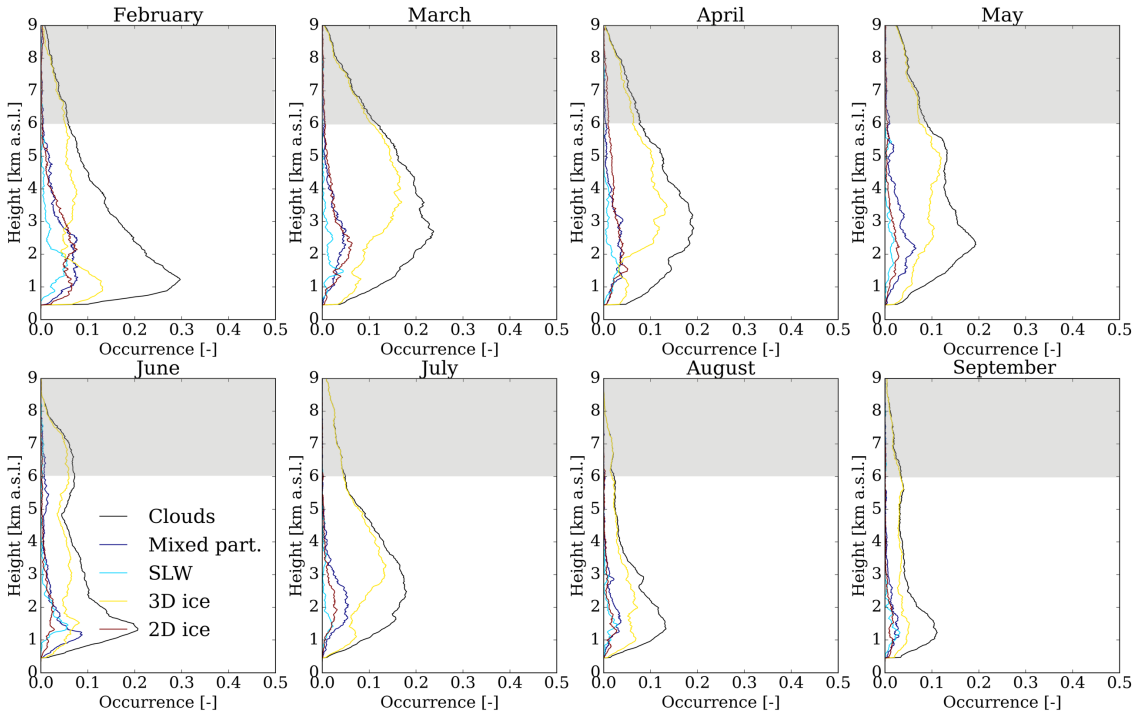

Figure 2.10: Monthly clouds occurrence per altitude derived from Lidar profiles for different types of hydrometeors. Only for clouds.

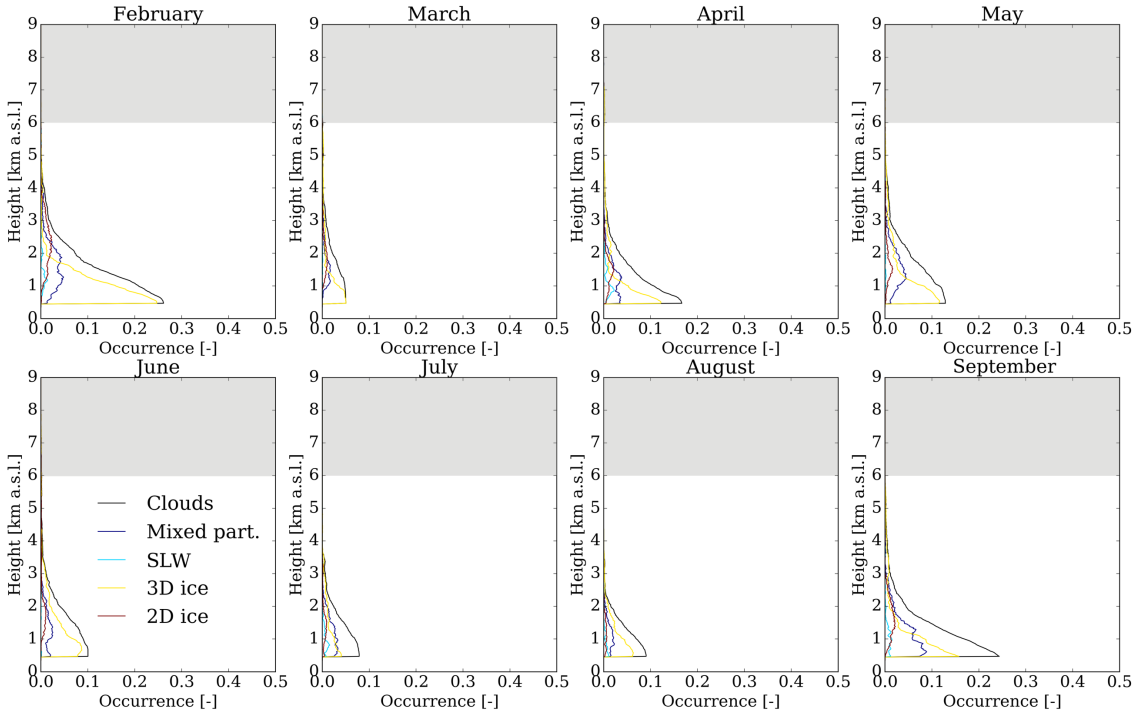

Figure 2.11: Monthly clouds occurrence per altitude derived from Lidar profiles for different types of hydrometeors. Only for surface precipitation.

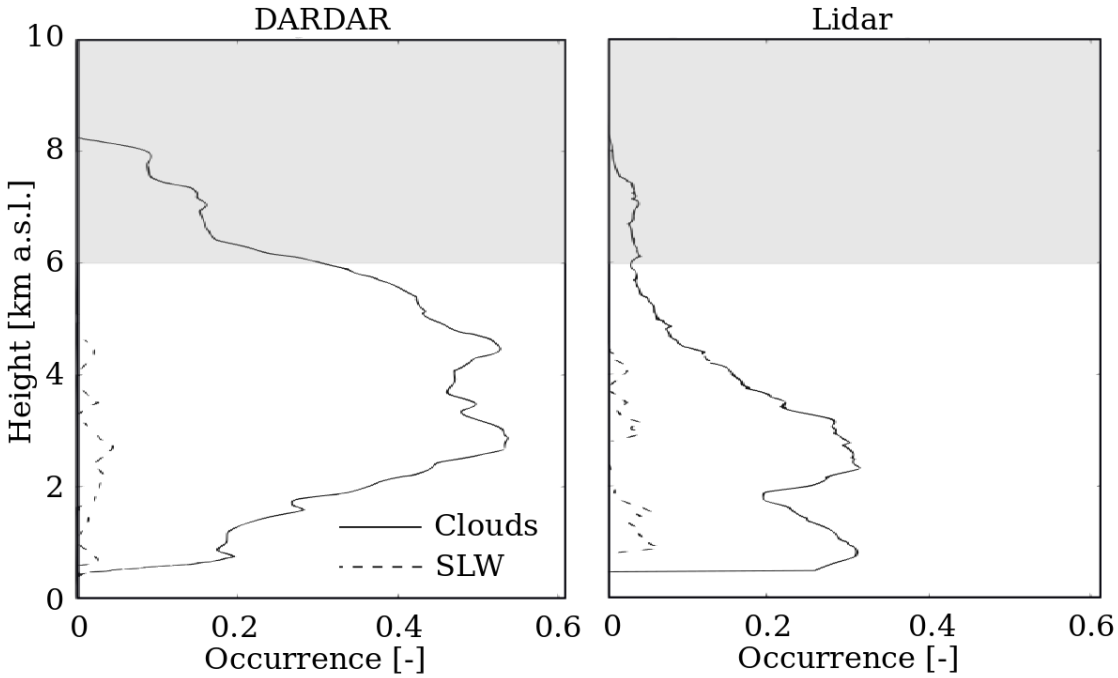

Figure 2.12: Occurrence of Clouds (solid lines) and SLW (dashed lines) using 5 satellite transect (DARDAR) located wintin 100 km from DDU, during April and co-located period of lidar profiles.

the number of overpasses of the satellite is a few per month. In addition, the passage duration of the satellite over the studied area is very short. Finally, lidar is sensitive to aerosols and cloud particles but is strongly attenuated, even totally extinguished by precipitation particles and thick SLW layers. Consequently, information obtained from observations from space about clouds located close to the ground may be lost and information about the highest clouds may be lost if obtained from ground-based observations.

Figure 2.12 shows the frequencies of cloud and SLW occurrence as a function of altitude according to 1) the DARDAR product (Delanoë and Hogan, 2010; Ceccaldi et al., 2013; Listowski et al., 2019) and 2) the ground-based lidar system at DDU for 5 overpasses over the 100 km zone around DDU during the period from April 1 to May 3, 2017. The DARDAR product combines information from the CALIOP (Cloud Aerosol Lidar with Orthogonal Polarization Winker et al., 2009, 2010) lidar on board CALIPSO (Cloud Aerosol Lidar and Infrared Pathfinder Satellite Observations) and from the Cloud Profiling Radar (CPR) on board CloudSat (Stephens et al., 2002). DARDAR products are available with a 60 m vertical resolution and 1.3 x 1.7 km^2 horizontal resolution.

The vertical extent of the profiles of cloud fraction obtained from space and

from ground measurements is quite the same, about 8 km. However the shape of the profiles and the values of occurrence frequency show important differences. First, smaller values of cloud fraction estimated from the ground-based instruments are observed. This is most likely due to the fact that ground based lidar observations may be disrupted by precipitation from the very first layers of the atmosphere. Similarly, more cloud fraction is seen by DARDAR in the highest altitudes than in the lowest altitudes, spaceborne lidar observations being not perturbated in the upper layers where precipitation are not present. Concerning the profile of SLW occurrence frequency, their shape and order of magnitude present similarities between DARDAR product and our classification method. This is particularly true for altitudes around 4 km. The vertical extent is also exactly the same. The main difference is visible in the lower part of the profile, probably the least accessible to the spaceborne lidar,because of attenuation of the lidar signal. Indeed, a smaller fraction of SLW is estimated by DARDAR below 2 km altitude. Results of classification de hydrometeors from space and from surface are consistent, especially with respect to the detection of supercooled water content in clouds.

2.7 Conclusion

This chapter deals with the classification of cloud and precipitation particles using a 532-nm elastic polarization lidar, a vertical-pointing K-band micro rain radar as well as radio soundings. This work was motivated by the fact that the properties of clouds and precipitation – in particular for mixed-phase clouds – have strong impacts on the radiative transfer and energy balance as well as on the microphysical processes and yet they are poorly documented in the Polar regions.

Three innovative techniques have been proposed for 1) the lidar signal processing, 2) the detection of hydrometeors and 3) their classification. First, lidar data was corrected for background noise signal thanks to an innovative approach that avoids overcorrection in case the signal is still strong and dominant in the far-range of the profiles (e.g. during clear sky nights or with thin clouds layers). Second, MRR data were used to identify the presence of precipitation at the surface level in order to make the identification of hydrometeor layers (according to the method proposed by Gong et al. (2011)) more reliable. Third, new development of the approach proposed by Yoshida et al. (2010) for hydrometeor classification was proposed: In addition to exploiting jointly attenuated backscattering coefficient and depolarization ratio to distinguish liquid water, 2D and 3D-ice particles, a cluster analysis based on the

k-means algorithm helped better separate classes. Moreover, adding the parallel backscatter coefficient in the classification method led to reduce the unclassified points and to a better distinction of the presence of SLW.

The enriched hydrometeor classification method was applied to a 1-year dataset (2017) of the DDU site at hourly time step. Despite a decreasing transmitted energy and therefore a progressive loss of sensitivity of the lidar, it was possible to identify cloud and precipitation particles and document the variability of the vertical profiles of this particles during almost one year. Cloud occurrence showed seasonal variations while SLW – present in a important proportion – seem to be quite constant all along the year. The analysis of the vertical distribution of clouds and SLW showed a more important concentration between 1500 and 2500 m. Clouds are mainly constituted by 3D-ice, in particular in the upper part. 2D-ice is observed only in the lower parts of the cloud. Concerning precipitation, 2D-ice was observed at all altitudes while most of 3D-ice was observed in the very lowest layers. The profiles of SLW were compared to those estimated by DARDAR products (based on spaceborne lidar and radar). Even if the top and the bottom of the vertical profile are not well observed respectively by ground-based lidar and spaceborne lidar and considering the differences in temporal and spatial dimensions, the pattern of SLW profile is consistent between both observation systems.

Chapter 3

The vertical structure of precipitation at two stations in East Antarctica derived from micro rain radars

Abstract

Precipitation over Antarctica is the main term in the surface mass balance equation of the Antarctic ice sheet, which is crucial for the future evolution of the sea level worldwide. Precipitation, however, remains poorly documented and understood mainly because of a lack of observations in this extreme environment. Two observatories dedicated to precipitation have been set up at the Belgian station Princess Elisabeth (PE) and at the French station Dumont d'Urville (DDU) in East Antarctica. Among other instruments, both sites have a vertically-pointing micro rain radar (MRR) working at the K-band. Measurements are continuously collected at DDU since the austral summer 2015-2016, while they have been collected mostly during summer seasons at PE since 2010, with a full year of observation during 2012. In this study, the statistics of the vertical profiles of reflectivity, vertical velocity and spectral width are analyzed for all seasons. Vertical profiles were separated into surface precipitation and virga to evaluate the impact of virga on the structure of the vertical profiles. The climatology of the study area plays an important role in the structure of the precipitation: warmer and moister atmospheric conditions at DDU favor the occurrence of more intense precipitation compared with PE, with a differ-

ence in 8 dBZ between both stations. The strong katabatic winds blowing at DDU induce a decrease of reflectivity close to the ground due to the sublimation of the snowfall particles. The vertical profiles of precipitation velocity show significant differences between the two stations. In general, at DDU the vertical velocity increases as the height decreases, while at PE the vertical velocity decreases as the height decreases. These features of the vertical profiles of reflectivity and vertical velocity could be explained by the more frequent occurrence of aggregation and riming at DDU compared to PE, because of the lower temperature and relative humidity at the latter, located further in the interior. Robust and reliable statistics about the vertical profile of precipitation in Antarctica, as derived from micro rain radars for instance, are necessary and valuable for the evaluation of precipitation estimates derived from satellite measurements and from numerical atmospheric models.

3.1 Introduction

Solid precipitation is a key component of the hydrological cycle in high-altitude and high-latitude regions. In Antarctica, precipitation falls mainly in form of snow and plays an important role as the largest positive term in the surface mass balance (SMB) of the Antarctic ice sheet (van Wessem et al., 2014, 2018). Climatological variations in precipitation regime can therefore significantly affect the SMB and thus the global sea level (Krinner et al., 2007; Mengel et al., 2016). Under different scenarios of climate warming, precipitation in the Antarctic region is expected to increase, due to an increase in the atmospheric moisture-holding capacity (Ligtenberg et al., 2013; Frieler et al., 2015; Tang et al., 2018). According to Palerme et al. (2017b), most of the models involved in the Fifth Climate Model Intercomparison Project (CMIP5) agree on the increase of precipitation, with an average change between 6 and 25% by the end of the 21st century, depending on the warming scenario. Nevertheless, an evaluation of the capacity of the models to simulate the current precipitation in Antarctica, using Cloudsat products as reference, reveals that most of the models overestimate the mean annual precipitation rate, reaching errors higher than 100% in some cases (Palerme et al., 2017b; Lemonnier et al., 2019). These results pose an important challenge in improving the current modelling of precipitation in Antarctica, and thereby having more confidence in the projections.

Although local net accumulation is often used as proxy for snowfall (e.g. Frezzotti et al., 2004), it is largely affected by precipitation conditions upstream of the site, leading to wind-driven snow transport to (or away from) the site (e.g. Van

den Broeke et al., 2004; Souverijns et al., 2018a). Ground-based radar instruments provide suitable information to monitor vertical variations of precipitation, through the collection of range-resolved Doppler radar observations (e.g. the vertical profile of mean Doppler velocity). The study of the vertical structure of precipitation is fundamental to understand the dynamical and microphysical processes controlling hydrometeors formation and evolution toward the surface, as well as to evaluate numerical atmospheric models and satellite precipitation products. Spaceborne active sensors, such as the Cloud Profiling Radar (CPR) on board of Cloudsat (and next on EarthCare), have the potential to monitor precipitation in a large horizontal and vertical extent in Antarctica (Palerme et al., 2014). However, this type of data source presents a generalized lack of observation close to the surface level, due to ground-clutter contamination, producing the so-called "blind zone" over the surface (the lower 1.2 km over land or ice for the case of Cloudsat) (Maahn et al., 2014). In this context, ground-based vertical profilers provide an advantage in terms of more detailed monitoring near the surface.

Significant efforts have been invested to monitor and better understand precipitation at two locations: the project APRES3 (Antarctic Precipitation Remote Sensing from Surface, http://apres3.osug.fr, Grazioli et al. (2017a)) at the French Dumont d'Urville station on the coast of Adélie Land and the project HYDRANT (HYDRological cycle in ANTarctica, https://ees.kuleuven.be/hydrant/hydrant.html, Gorodetskaya et al. (2015)) and its follow up AEROCLOUD (How do AEROsols and CLOUDs affect the East Antarctic climate?, https://ees.kuleuven.be/hydrant/aerocloud/) at the Belgian Princess Elisabeth station in Dronning Maud Land, both of them implemented with a vertical-pointing K-band micro rain radar (MRR). Other recent initiatives that also study precipitation in Antarctica are the micro rain radar observations collected at the Italian station Mario Zucchelli (Souverijns et al., 2018b) and the AWARE (ARM West Antarctic Radiation Experiment) field campaign organized by ARM/ASR (Atmospheric Radiation Measurement/Atmospheric System Research) which involved multiple radars at various frequencies and satellite-based remote sensing observations at McMurdo station (Lubin et al., 2017).

The main objective of this work is to characterize the vertical structure of the precipitation from profiles of the Doppler moments from MRRs located at these two different sites in East Antarctica, analyzing the vertical structure of precipitation throughout the year to understand the main microphysical processes involved in its variability. This knowledge will represent a significant input in the calibration

and validation of satellite observation in Antarctica and modeling purposes. This manuscript is structured as follows: Section 3.2 provides a description of the study area, the data and methodology used in this study; Section 3.3 presents the overall statistics of the vertical profiles; Section 3.4 analyses the importance of surface precipitation and virga in the study area; Section 3.5 is the seasonal analysis and Section 3.6 delivers a summary and the main conclusions of this work.

3.2 Material and methods

3.2.1 Study area

Two different sites were studied in East Antarctica, corresponding to the APRES3 and HYDRANT/AEROCLOUD observatories, located in Dumont d'Urville (DDU) and Princess Elisabeth (PE) stations, respectively. The Information relative to DDU and PE is detailed in Subsection 1.4.1. Figure 1 displays the location of both stations on a elevation map.

3.2.2 Ground-based MRR observations

In this Chapter, observation form the frequency-modulated continuous-wave (FMCW) micro rain radar (MRR) were used in the analysis. All the detail regarding to this instrument at the two stations is presented in the Chapter 1 in the Subsection 1.4.2.

3.2.3 MRR post-processing

MRR data were processed using the method of Maahn and Kollias (2012) (hereafter noted MK12) that improves the noise filtering algorithm and implements a dynamic procedure to dealiase the Doppler spectrum, allowing to take into account very small and negative W (cases of weak updraft). More detail of MRR and the post processing are detailed in the subsections 1.2.6 and 1.4.2.

The instruments exhibited different types of noise at the two stations that were not completely filtered out after the post-processing proposed by MK12. For MRR at DDU during given periods, a spread noise that covers all the range bins, especially during clear sky conditions, was present. For MRR at PE (and also a second MRR deployed at DDU) sometimes a particular artifact between different range gates was observed, encompassing from a few minutes up to a full day.

MRR at DDU sometimes experienced interruptions during the acquisition time, leading to a decrease in the number of observations per minute, collecting 2 instead of ∼6 profiles per minute. This decrease of the sampling rate leads to an increase of the normalized standard deviation (V_T) of a set of spectra and MK12 interpreted the signal as a container of potential peak due to precipitation. Therefore, the V_T threshold used by MK12 to remove clear-sky profiles from the post-processing was adapted to be dependent on the sampling rate of the instrument (See Appendix A). All clear sky noise was removed from MRR data.

For MRR at PE, the presence of artifacts could be due to low-frequency interferences produced by nearby electronic devices. The affected range gate depends on the frequency of the interference and adjacent gates are affected by leakage between gates. The interference produces a strong peak in the Doppler spectrum which frequently appears in the largest velocity gates. 3% of the days at PE containing bands of noise were excluded from the analysis.

3.2.4 Radio soundings

Daily radio soundings are carried out all year long at 00 UTC at DDU station by MeteoFrance, while at PE only summer radio soundings are available since 2014, collected at 12 UTC by the Royal Meteorological Institute of Belgium. In this work, we use vertical profiles of air temperature and relative humidity to characterize different precipitation types and seasons (only summer at PE), corresponding to simultaneous observations of radio soundings and MRR. Relative humidity (RH) with respect to liquid water is converted into relative humidity with respect to ice (RH_i) using the ratio of the saturation vapor pressure over water e_{sw} to the saturation vapor pressure over ice e_{si} as it is shown in the following equation:

$$RH_i = RH \cdot \frac{e_{sw}}{e_{si}}, \tag{3.1}$$

e_{sw} and e_{si} are derived using the equations of Goff (1957), detailed in Appendix B.

3.2.5 Statistics of vertical profiles and temporal integration

The statistics of the vertical profiles of reflectivity (VPR), of vertical velocity (VPV) and spectral width (VPS) are analyzed at DDU and PE. Considering the high variability of short time observations influenced by advection and turbulence, different temporal integration intervals are evaluated in order to choose an optimal integra-

tion time for analysis. The variability of the average VPR at fixed time intervals between 1 min and 12 h is analyzed at both stations. Average VPR are calculated in linear units ($mm^6\ m^{-3}$) as the sum of the 1-min VPRs along fixed windows of t duration, divided by t and then converted in dBZ as in Welsh et al. (2016).

Figure 3.1a and c show the average VPR at different temporal resolutions for DDU and PE respectively, compared to the original 1-min resolution. Significant differences can be observed between the absolute values of VPR between the two stations, with a higher Z_e at DDU than at PE and greater variability between integration intervals. These differences in the average VPR at the two stations, are the first indication about the presence of different growth habits and size distribution of ice particles at DDU and PE. Ice growing processes, such as riming and aggregation, that depend on temperature and the moisture content in the atmosphere, can play an important role in the increase of Z_e. The relatively warmer conditions at DDU and the proximity to the a cyclogenesis region (Bromwich et al., 2011), may explain the observed differences with respect to PE.

Variations of VPR between temporal resolutions t are compared using the following expression:

$$\delta = \frac{|\Delta Z_e|}{\Delta t \cdot Z_e} \tag{3.2}$$

where ΔZ_e is the absolute difference in Z_e between consecutive temporal integration, Z_e is the average VPR and Δt is the increase in time resolution, with a constant value equal to 15 min, except for the first interval between 1-min and 15-min temporal integration steps. The values of VPR decrease as the temporal integration increases, but at each step the Z_e values tend to decrease more slowly. Figure 3.1, panels b and d show the mean, minimum and maximum variation (δ) of the average VPRs with respect to the time integration steps, for DDU and PE respectively. At both stations, VPR presents large changes between shorter time scales and it is more stable for larger time resolution. Maximum and minimum variation in the vertical profile also decrease, which means that the shape of the VPR also becomes more stable. The integration times of 1 h and higher represent more stationary patterns in the vertical profile than short time integration, that can be affected by advection or turbulence. Based on this analysis, 1 h was considered as an optimal temporal integration to study climatological patterns in the VPR, removing the short time perturbations while keeping enough observations to make a robust statistical analysis.

After the selection of the temporal integration, VPV and VPS are averaged at the same temporal resolution. In these cases, the average does not consider the zero

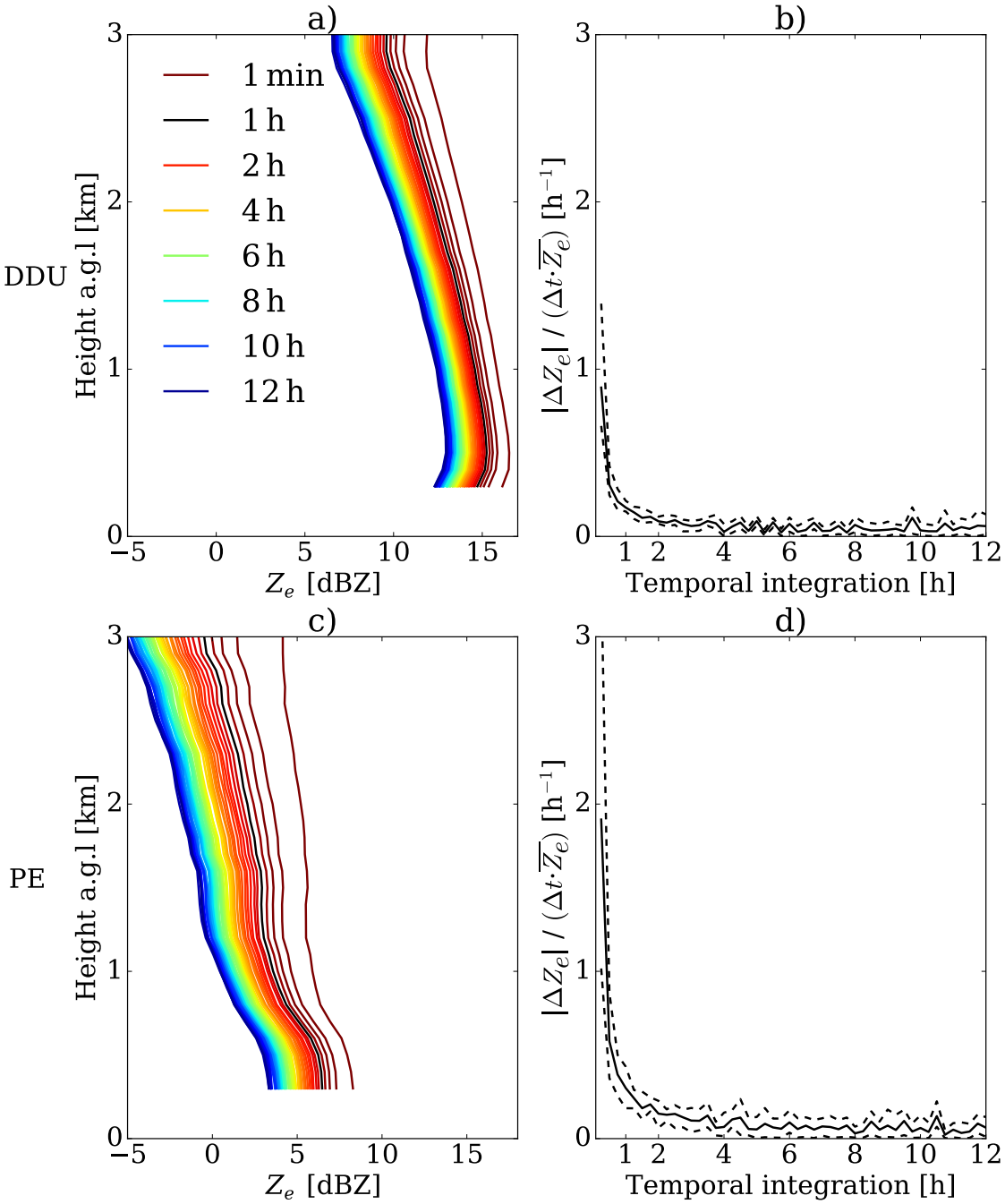

Figure 3.1: Average VPR at different temporal integrations are displayed in (a) and (c) panels, for DDU and PE respectively. Colored lines represent different temporal integration steps, corresponding to 1 min and from 15 min to 12 hours separated by 15-min intervals (legend displays only a few selected time steps and 1-h VPR is represented in black). The temporal variability between time steps is shown in panels (b) and (d), for DDU and PE. Bold lines correspond to the mean reduction of Z_e in function of the temporal integration step, weighted by time interval and the mean Z_e at the given time scale. Dashed lines are the maximum and minimum reductions of Z_e within the whole average VPR.

values (clear sky situations), as the case of VPR, because W and σ_v are considered as intensive properties of precipitation, which means that they are independent of the amount of precipitation within a given temporal interval.

3.2.6 Precipitation profile classification

We classified the vertical profiles of precipitation in two different categories based on whether the precipitation reaches the surface or not. Figure 3.2 shows and example of vertical profiles of virga and surface precipitation observed using Z_e profiles during the same precipitation event. Snowfall sublimation depends on both the properties of the solid hydrometeors (e.g. bulk density, terminal velocity and particle size distribution) and meteorological conditions (e.g. relative humidity, temperature) (Clough and Franks, 1991; Maahn et al., 2014). Precipitation sublimation and virga may occur often in Antarctica under temperature inversion and unsaturated air conditions (Maahn et al., 2014; Grazioli et al., 2017b). At both sites, virga have been reported in previous works by using ground-based remote sensing techniques, such as radar and lidar instruments (e.g. Gorodetskaya et al., 2015; Maahn et al., 2014; Grazioli et al., 2017a).

MRR is especially suitable to detect hydrometeors that have reached a sufficient size to fall as precipitation, including streaks of virga, but it is insensitive to cloud particles (Gorodetskaya et al., 2015; Souverijns et al., 2017). For this reason, the presence of precipitation signal in the lowest reliable MRR range gate of each profile was used to separate virga observations from surface precipitation. Occurrence of echoes at 300 m height was used as reference of surface precipitation since there is no useful signal below this height for all the profiles at both stations.

3.3 Overall statistics

The statistics of all the MRR profiles for the complete observation period at both stations were carried out, prior to the classification of the precipitation profiles and the seasonal analysis, to obtain a general picture of the distribution of the variables of interest. A total of 5331 and 5058 hourly vertical profiles were obtained at DDU and PE during all respective data periods. Figure 3.3 shows the distribution of Z_e, W and σ_v in the vertical profile extension in percentage, normalized by the total number of the range gates containing precipitation. In the following subsections, the statistics for vertical profiles of the three Doppler radar moments are presented.

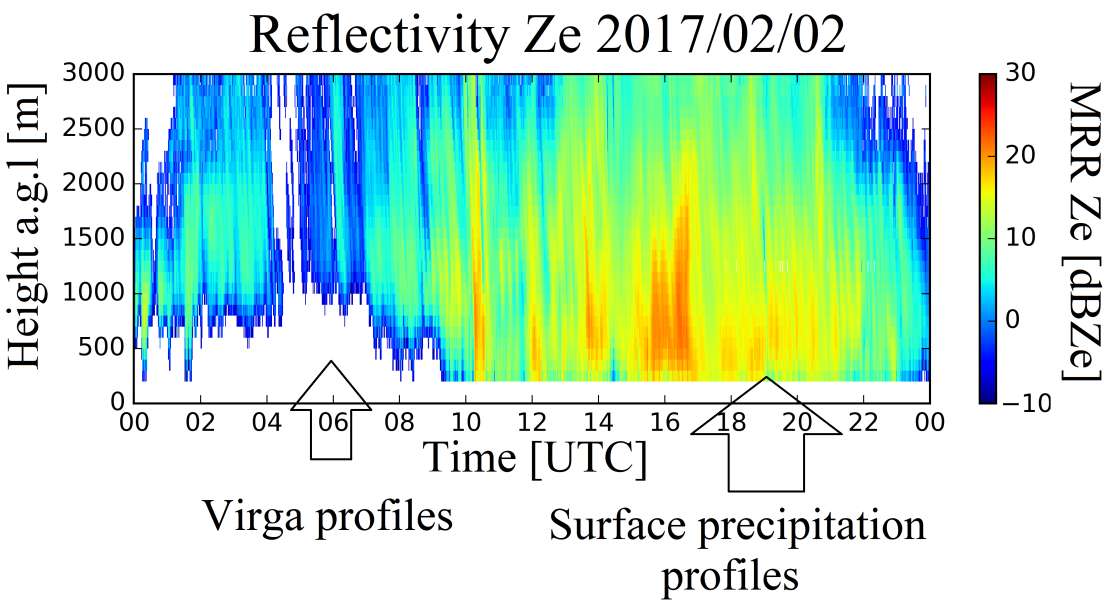

Figure 3.2: Virga and surface precipitation profiles detected using vertical profiles of Ze at DDU.

3.3.1 Vertical profiles of reflectivity

At both stations, mean and median VPR describe a general increase from the top toward the surface. Variability of Z_e depends on the microphysical and scattering properties of the targets such as the particle size distribution (PSD) and the complex refractive index (m). Previous studies have shown that in the ice part of precipitating clouds and snow storms, the ice growth by vapor deposition, riming and/or aggregation have an important role on the vertical evolution of PSD and thus on the vertical patterns of radar VPR, which may cause the observed increase of Z_e toward the surface (Moisseev et al., 2009, 2015; Bechini et al., 2013; Schneebeli et al., 2013; Pfitzenmaier et al., 2018). Considering that dry snow is a mixture of ice and air, the dielectric properties of a particle depend on the proportion of ice and air that it contains, thus $\underline{m}$ is sensitive to the snow/ice particle type and bulk density (Tiuri et al., 1984; Sadiku, 1985). The vertical profiles of snow types have been identified with the dual-polarization weather radar observations collected at DDU by Grazioli et al. (2017a), who found that more pristine particles (e.g. dendrites, columns) are largely dominant above 2.5 km of height and that the proportion of aggregates and rimed particles significantly increases with decreasing height. For the case of PE, rimed particles and graupel are less frequent due to the colder temperatures in this region (Souverijns et al., 2017).

Mean VPR at DDU experiences a peak of maximum Z_e of 15.3 dBZ close to

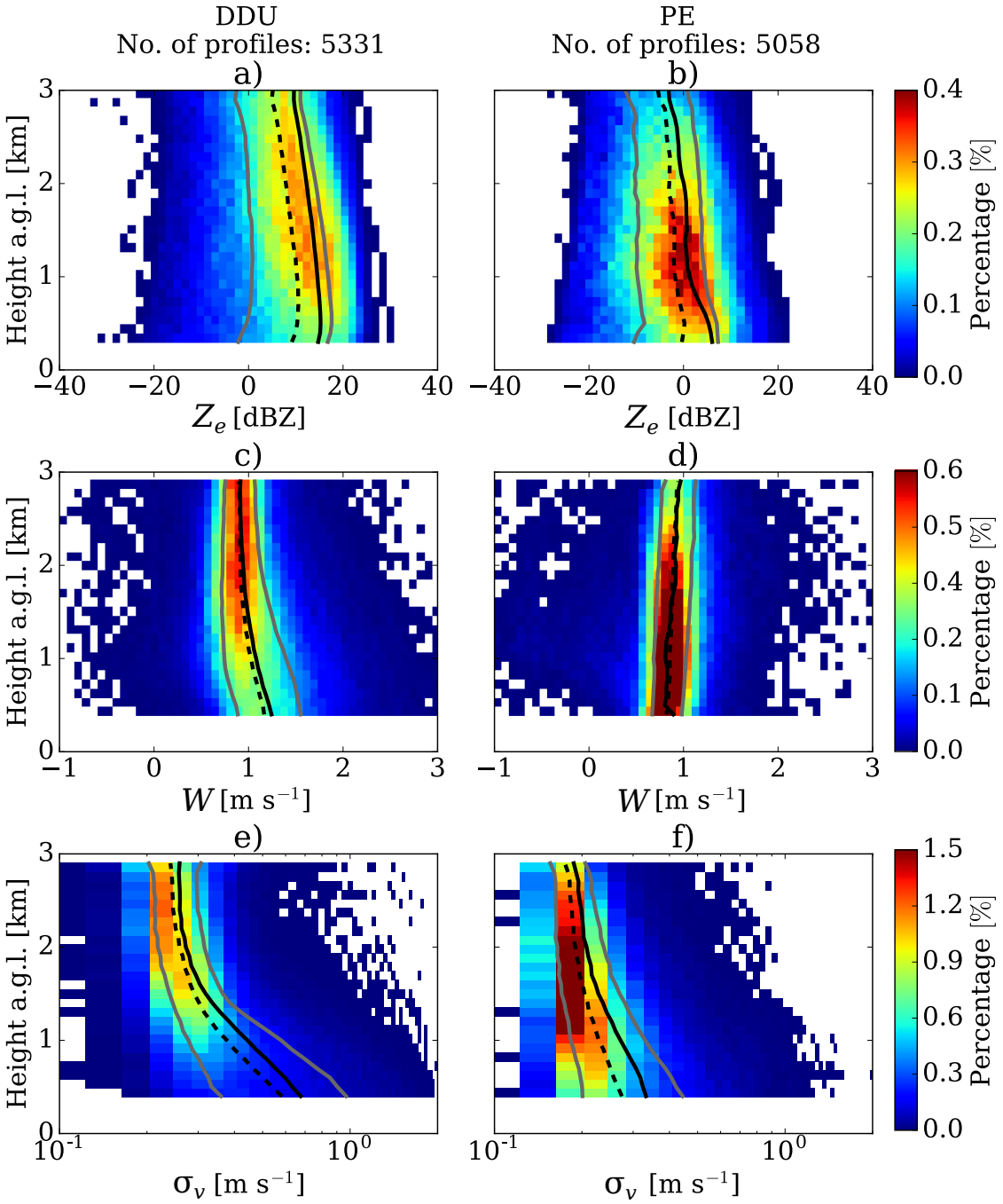

Figure 3.3: Frequency by altitude diagram for Z_e (a, b), W (c, d) and σ_v (e, f) values observed at DDU (a, c, e) and PE (b, d, f). Solid-black and dashed-black lines represent the average and median vertical profiles of Z_e, W and σ_v respectively. Grey lines correspond to the 20 and 80% quantiles of the vertical profiles. σ_v values are plotted in log x-axis to highlight the variations for small values.

the ground followed by a decrease toward the surface to 14.7 dBZ. This particular pattern is associated with an enhanced sublimation process driven by low-level katabatic winds leading to unsaturated air conditions that favor the sublimation of ice particles, especially associated with lighter snowfall (Grazioli et al., 2017b), but it is not clearly observed at PE (see Figure 3.3a, b).

At PE, where katabatic winds are less strong than at DDU due to the Sør Rondane Mountain sheltering (Gorodetskaya et al., 2013, 2015; Thiery et al., 2012), the mean VPR does not exhibit a decrease close to the surface as it is observed at DDU. It must be noted that most observations at PE were collected in summer when katabatic winds are even weaker. The Z_e value at the lowest height is 6.1 dBZ, which corresponds to a difference of 8.6 dBZ compared to DDU at the same range bin.

The average VPRs at both stations are larger than the median VPRs at all the range bins, because the mean values are strongly influenced by a few high values. Median and quantiles are not affected by the differences of Z_e values and they can represent the patterns of lower reflectivity values. For instance, low level sublimation is observed on these lower quantiles of VPR (e.g. Q20%) inducing an amplified decrease of Z_e near the surface at DDU and even observable at PE, probably because small ice particles within these events are more susceptible to sublimation (Clough and Franks, 1991; Grazioli et al., 2017b).

3.3.2 Vertical velocity profiles

The vertical structure of W presents two different patterns at DDU and PE (see Figure 3.3c, d). In the case of DDU, mean and median VPV remain constant at about 0.9 m s^{-1} from 3 to 1 km of height, and increase up to 1.2 m s^{-1} in the lowest km above ground. At PE, a limited decrease from about 1 m s^{-1} at 3 km of height to about 0.9 m s^{-1} at 400 m of height is observed.

W represents the mean of the reflectivity-weighted terminal velocities of the scatters, but also is influenced by the vertical air motion. Depending on the type of ice particles, the terminal velocity V_t can be parameterized as function of the maximum size D, based on the different relationships between air friction and Reynolds number (Re), which both depend on the air density ρ_a (Böhm, 1989; Mitchell and Heymsfield, 2005; Heymsfield and Westbrook, 2010; Molthan et al., 2010). At DDU, the increase in occurrence of larger hydrometeors towards the ground, mainly of aggregates and to a lesser extent rimed particles (Grazioli et al., 2017a), can explain

the observed increase in the VPV in the lowest km above ground.

At PE, the habits of hydrometeors at the ground are represented by mostly small dendrites, columns, capped columns and rosettes (Gorodetskaya et al., 2015; Souverijns et al., 2017), that are more affected by air friction, resulting in lower values of W than at DDU. Moreover, for small crystals with low growth along the downward trajectory, the increase of air density can lead to an increase of the air friction and thus to a decrease of V_t and W, which can be the reason for the slight but regular decrease in the VPV toward the surface observed at PE. Previous works have used a power-law relationship between size and terminal velocity with an air density correction factor that take into account the inverse relation between V_t and ρ_a (e.g. Molthan et al., 2010; Heymsfield et al., 2013):

$$V_t(D) = aD^b \left(\frac{\rho_0}{\rho_a}\right)^w \tag{3.3}$$

where ρ_0 is the air density at the surface, a and b are the parameters of the power-law relationship depending on the type of ice particle and w controls the correction factor, usually equal to 0.4. According to standard atmospheric conditions, air density can increase from 0.79 to 1.07 kg m^{-3}, from the 3 km of height level to the ground at PE, leading to a decrease 11% of terminal velocity, that is in accordance with the results obtained at PE. Finally, a decrease toward the ground of the fall speed of the crystals can also be expected when air temperatures increase, since air viscosity also increases with temperature (Westbrook, 2008). A more detailed comparison of VPV in the common range of altitudes above sea level at the two stations is presented in Appendix C.1.

3.3.3 Vertical profiles of spectral width

For a vertically pointing radar, the spectral width (σ_v) represents the variability of the vertical velocity due to the variety of particle sizes and shapes within the sampling volume (Garrett et al., 2015; Maahn and Kollias, 2012). The variability of the vertical velocity is also influenced by the environmental turbulence (i.e. strong turbulence leads to a broad spectrum) (Nastrom, 1997; Garrett and Yuter, 2014). In the case of DDU, the average VPS describes no significant variations between 2 and 3 km a.g.l., but it exhibits a constant increase toward the surface along the 2 km near the ground. This increasing of VPS occurs at the same height where VPV begins to increase and also where the differences between Q20% and Q80%

of W increases (see Figure 3.3e). One factor that can explain this increase of VPS toward the surface is the increase of rimed particles and aggregates that co-exist with small ice particles, generating spectra with low and high Doppler speeds. Moreover, the interaction of the particles with the turbulent katabatic layer below 2 km, can increase the spectral width (Parish et al., 1993).

On the other hand, the VPS at PE also increases toward the surface, but less pronounced than at DDU. Figure 3.3e shows the probability of occurrence of σ_v at different heights. Dominant presence of small particles, with low probability of rimed or aggregated particles, leads to lower variations of VPS.

3.4 Surface precipitation and virga

Previous studies (e.g. Maahn et al., 2014; Gorodetskaya et al., 2015; Grazioli et al., 2017a,b) and our current observations suggest that virga is a frequent phenomenon in the study area (36% of the precipitation profiles at DDU and 47% at PE are virga observations), it is therefore worth to analyze its impact on the climatology of the vertical structure of precipitation in the study area. For that, the statistics of all vertical profiles are analyzed, based on the classification of surface precipitation or virga. Higher values of virga occurrence could be expected, considering that the absence of data below 300 m makes it difficult to discriminate between virga and surface precipitation.

Figures 3.4 and 3.5 show the vertical distribution of Z_e, W and σ_v values for the entire observation period, separated into surface precipitation and virga, for DDU and PE respectively. The signature of the mean and median VPR of the surface precipitation show important differences with respect to virga. At both locations, VPR of virga has a lower reflectivity than the profiles associated with precipitation reaching the surface, because weaker precipitation is more likely to be completely sublimated. The occurrence of riming/aggregation of the hydrometeors may also play a secondary role in the increase of W toward the surface observed at DDU in virga profiles.

Ice virga occurs when the low troposphere is dry, ice particles are small and do not experience significant growth, which are ideal condition for ice sublimation (Clough and Franks, 1991). In the case of DDU, the peak of the mean VPR of surface precipitation is 15.8 dBZ, whereas the peak of the virga VPR is 7.5 dBZ. The values closest to the ground for surface precipitation and virga are 14.7 dBZ and -12.9 dBZ, evidencing an enhanced sublimation rate towards the surface for virga

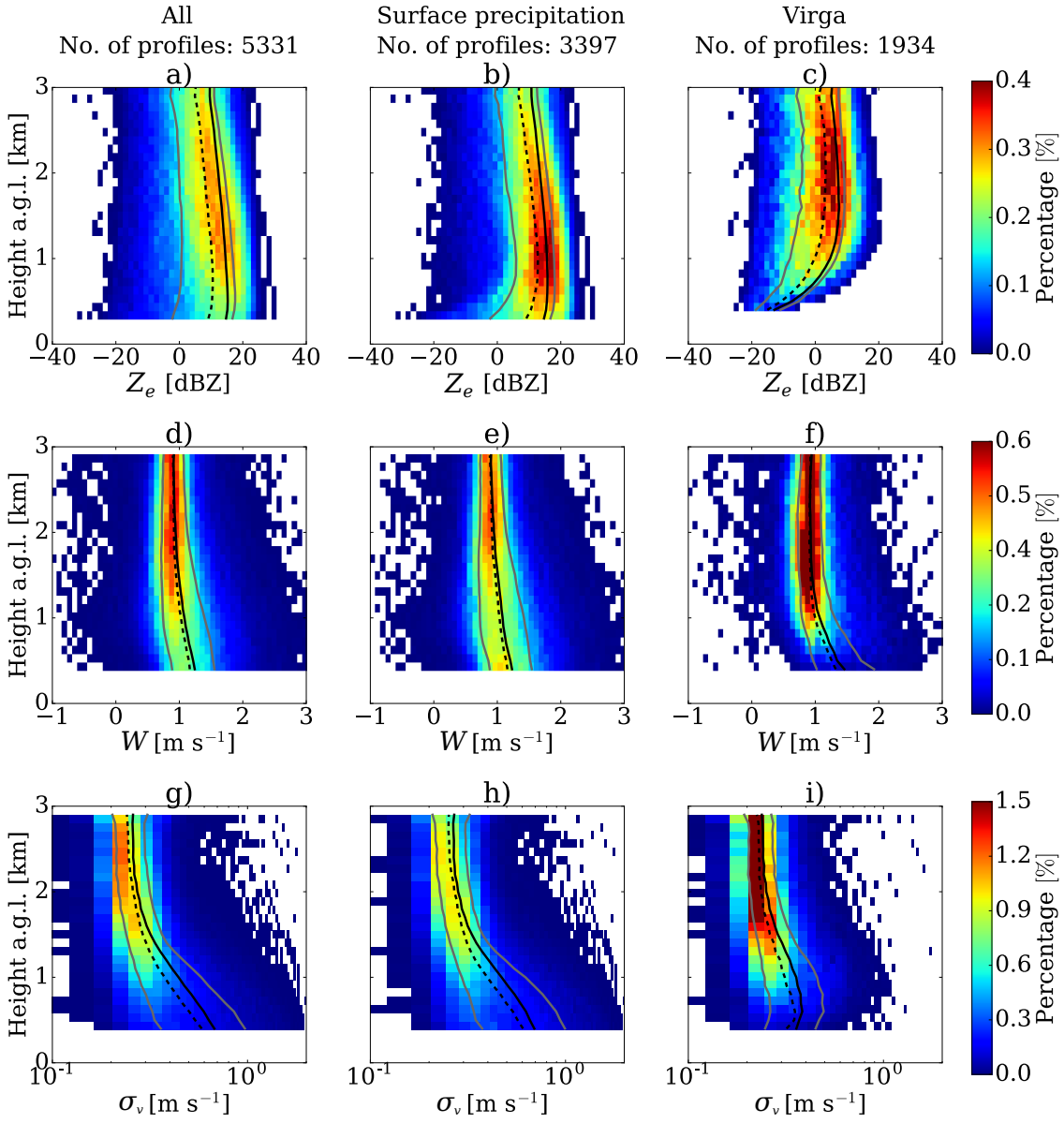

Figure 3.4: Frequency by altitude diagram for Z_e (a, b, c), W (d, e, f) and σ_v (g, h, i) values observed at DDU, separated by type of snowfall. (a, d, g) correspond to all the profiles, (b, e, h) to surface precipitation and (c, f, i) to ice virga. Solid-black and dashed-black lines represent the average and median vertical profiles of Z_e, W and σ_v respectively. Grey lines correspond to the 20 and 80% quantiles of the vertical profiles. σ_v values are plotted in log x-axis to highlight the variations for small values.

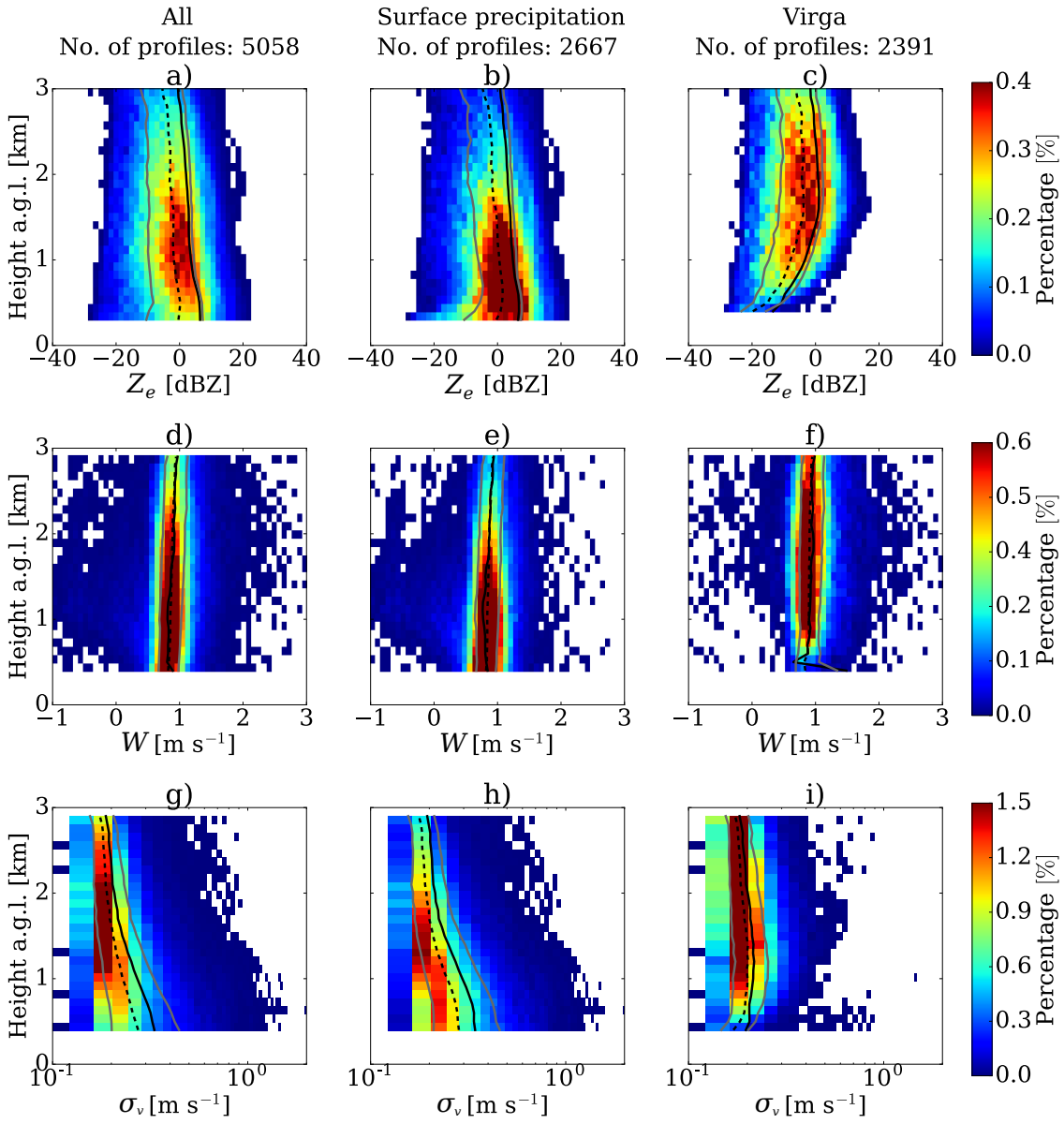

Figure 3.5: Same as Figure 3.4, but for Princess Elisabeth station.

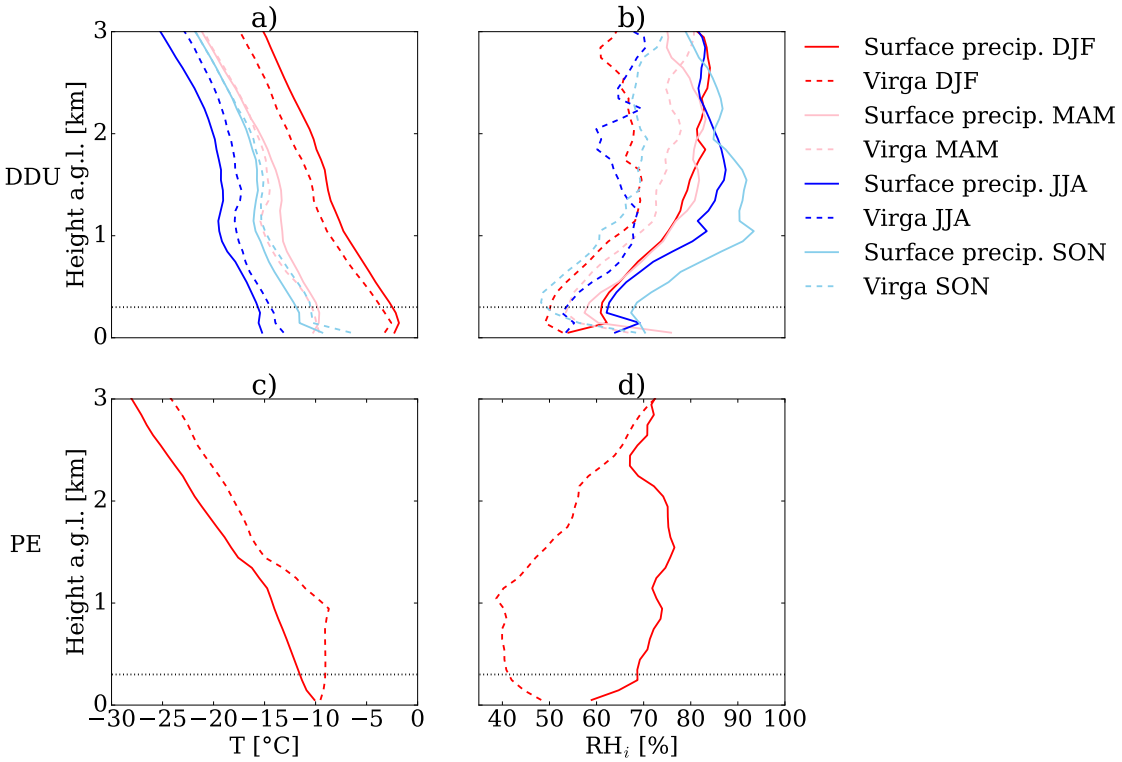

Figure 3.6: Average vertical profiles of air temperature T_a (a and c) and relative humidity with respect to ice RH_i (b and d) during simultaneous time of radio sounding and profiles of precipitation observed with MRR at DDU (a and b) and PE (c and d). Red, pink, blue and sky blue lines represent the summer (DJF), autumn (MAM), winter (JJA) and spring (SON) respectively, and solid lines correspond to surface precipitation, while dashed-lines are virga events. Horizontal doted lines correspond to the height of the lowest available MRR bin (300 m).

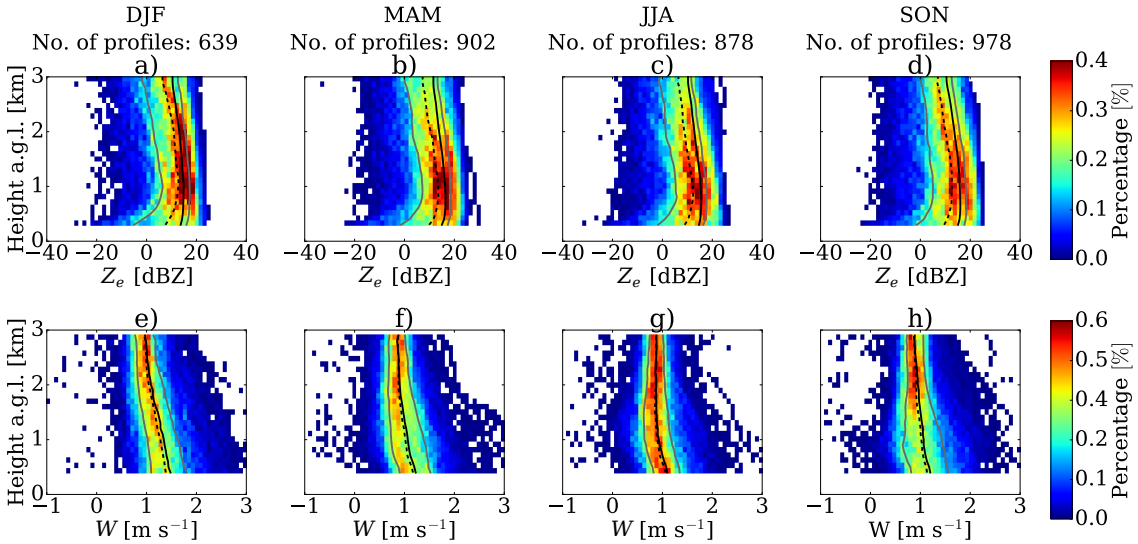

Figure 3.7: Frequency by altitude diagram for Z_e (a, b, c, d) and W (e, f, g, h) values observed at DDU during DJF (a, e), MAM (b, f), JJA (c, g) and SON (d, h) of surface precipitation. Solid-black and dashed-black lines represent the average and median vertical profiles of Z_e and W respectively. Grey lines correspond to the 20 and 80% quantiles of the vertical profiles.

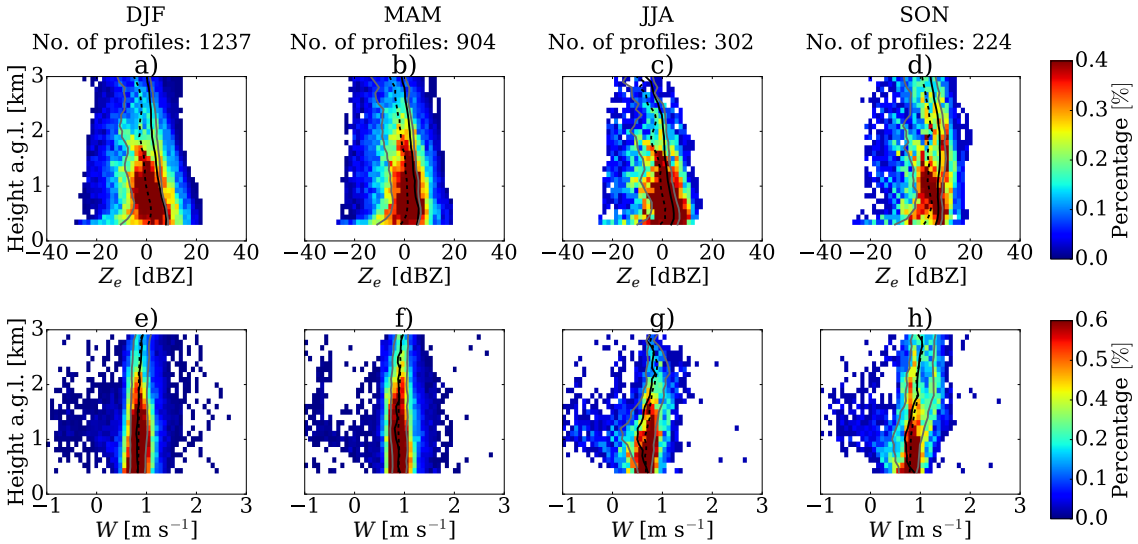

Figure 3.8: Same as Figure 3.7, but for Princess Elisabeth station.

profiles. With respect to the VPV, the patterns of surface precipitation are similar to those for all profiles together, however VPV of virga shows a significant increase of W within the lower 1000 m toward the surface. This increase of W for virga profiles at DDU suggests that small particles are the first to sublimate completely, leading to an increase of the mean Doppler velocity because of the biggest particles.

At PE, the values of Z_e are lower compared to DDU, but they also present significant differences between VPR of surface precipitation and virga. The maximum value of the mean VPR of surface precipitation is 6.8 dBZ and 1.1 dBZ for the case of virga. The respective values near the ground are 6.5 and -13.4 dBZ. The VPV shows a steady but constant decrease of the vertical velocity for both precipitation reaching the surface and virga. The fast increase of W for ice virga does not happen at PE, which can be explained by the lower occurrence of aggregation and riming, leading to lower vertical velocities and narrow spectral width, compared with DDU. The two lower layers of mean VPV for virga show an irregular shape because the mean value become more sensitive to the extremes when the number of observations is reduced (see Figure 3.5f). Median VPV does not present this problem at the lowest bin gates and it shows the same decreasing pattern of the rest of the profile.

The VPS presents similar behavior at both stations as visible in Figure 3.4 and 3.5 (g, h and i). For surface precipitation, VPS increases toward the surface similarly for all profiles together. For the case of ice virga, VPS increases going to the surface but decreases within the lower 1000 m. Although there is an increase in turbulence that increases the value of σ_v, in the last part of the trajectory of the particles, a large part have been sublimated, especially those of small size, reducing the breadth of the velocity spectra.

The low-level sublimation of surface precipitation is more evident when the profiles of virga are removed from the analysis. This can be observed in both stations, comparing the quantiles 20% of the Figure 3.4a-b and Figure 3.5a-b. For all the profiles together, the low Z_e values of virga profiles, just above the low-level sublimation layer, smooth the strong curvature that is observed when virga is removed.

These results confirm that virga has a significant impact on the patterns of the vertical profiles of Z_e, W and σ_v, which makes it necessary to differentiate both types of profiles to analyze the structure of the precipitation in the study area. In the following section, a seasonal analysis of the surface precipitation and virga is presented.

Table 3.1: Percentage of surface precipitation and ice virga with respect to the total number of vertical precipitation profiles during all data period and each season at DDU and PE.

Site	Precipitation type	All seasons	DJF	MAM	JJA	SON
DDU	Surface precipitation	64	56	63	66	69
	Virga	36	44	37	34	31
PE	Surface precipitation	53	51	52	63	53
	Virga	47	49	48	37	47

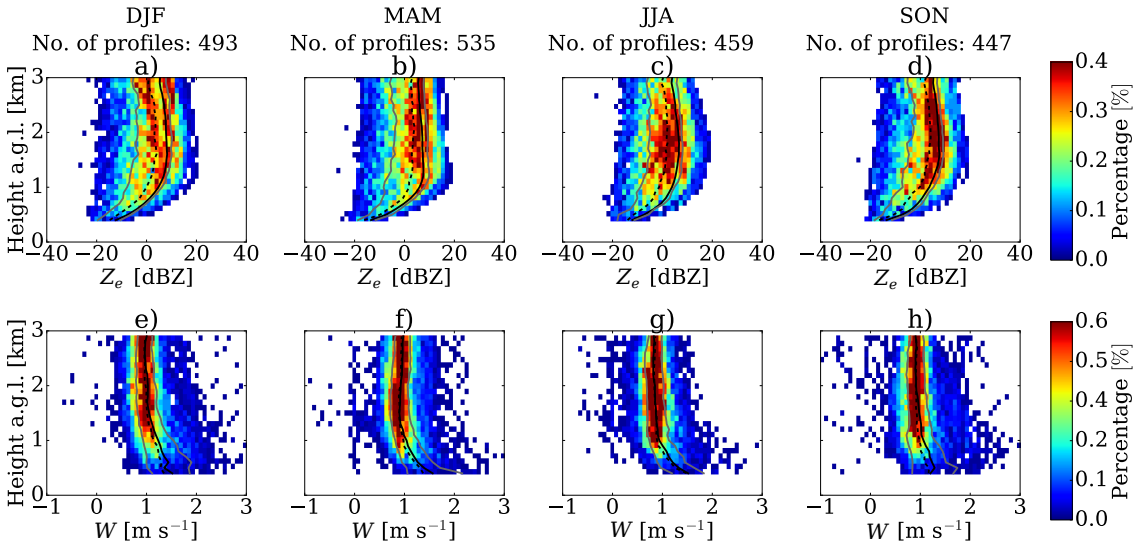

Figure 3.9: Frequency by altitude diagram for Z_e (a, b, c) and W (e, f, g) values observed at DDU during DJF (a, e), MAM (b, f), JJA (c, g) and SON (d, h) of virga. Solid-black and dashed-black lines represent the average and median vertical profiles of Z_e and W respectively. Grey lines correspond to the 20 and 80% quantiles of the vertical profiles.

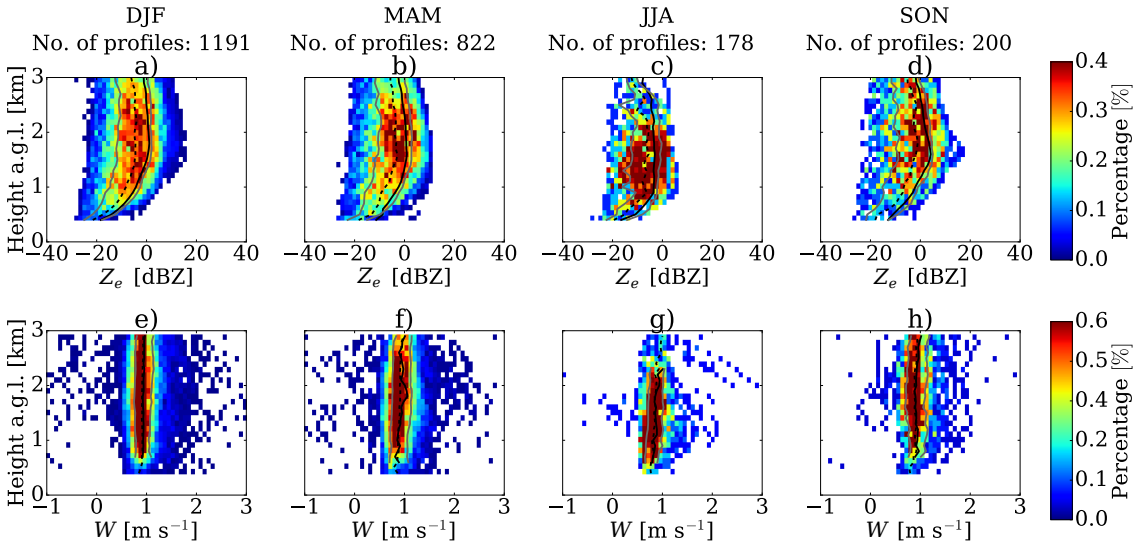

Figure 3.10: Same as Figure 3.9, but for Princess Elisabeth station.

3.5 Seasonal variability of vertical profiles

Seasonality of precipitation in Antarctica depends on the availability of moisture in the atmosphere, which depends on the air temperature and the large-scale circulation dynamics in relation to the topography of the continent (Schlosser, 1999; van Lipzig et al., 2002; Marshall, 2009). Coastal region are more affected by the influence of poleward moisture transport, while inland regions are less influenced, because of the blocking by the ice sheet (van Lipzig et al., 2002). Since the seasonality of precipitation is region-dependent, it is fundamental to perform a seasonal analysis of the vertical structure of the precipitation at the two study areas.

In general terms, observations are distributed with 21, 27, 25 and 27% for December-January-February (DJF), March-April-May (MAM), June-July-August (JJA) and September-October-November (SON) respectively at DDU, while at PE the distribution is more concentrated during DJF (48%) and MAM (34%) because of power failures occurred during winter, when the station is not active. Profiles for JJA and SON at PE correspond to the 9 and 8% of the observations, therefore the overall statistics are biased towards DJF and MAM at PE.

Figure 3.6 shows the average radio soundings of the air temperature (T) and the relative humidity with respect to the ice (RH_i) for co-located profiles of MRR during surface precipitation and virga events. At DDU, the vertical profiles of T show a seasonal cycle during both types of precipitation. For the cases of RH_i, a seasonality is not clearly observed, however profiles corresponding to virga events are systematically drier than those for surface precipitation, conditions expected when solid particles are completely sublimated before reaching the surface. Radio soundings at PE show colder profiles in summer compared to DDU and also drier troposphere during virga events compared to precipitation reaching the ground.

3.5.1 Surface precipitation

During the different seasons at DDU, surface precipitation remains dominant (56 to 69% of occurrences, see Table 3.1), with the lowest proportion during summer. Figure 3.7 shows the variability of the VPR and VPV for the different seasons at DDU. Despite that the 3 km range of the radar does not display the full extent of the precipitation systems, this higher percentage of observations in the highest gates suggests that the vertical extension of precipitation events in summer is larger than in the other seasons.

The mean and median VPV at DDU show low variations in the top and then

an increase toward the surface. During summer the height at which W starts to increase (2.5 km) is higher compared to autumn and spring (2 km) and winter (1 km). The aggregation process is more favored when temperatures are higher than -15°C (Hosler and Hallgren, 1960; Hobbs et al., 1974), thus a possible explanation for this pattern is that in summer particles have a higher probability to increase in size, since the environmental conditions are favorable for aggregation, according to the radio soundings collected at DDU during precipitation events of the present study (see Figure 3.6) and previous long term observations (Mygard et al., 2013). The influence of temperature on the vertical radar profiles in the study area, in particular for surface precipitation, is detailed in the Appendix D. On the other hand, the longer path that particles travel during summer increases the probability of reaching bigger size and W, because the longer a particle takes to reach the surface,the greater the probability of interaction with other particles, favoring the growth by (i.e. by aggregation).

At PE, surface precipitation is also dominant in all seasons, but with a slightly lower occurrence compared with DDU. The season with lower percentage of surface precipitation is summer (51%), on the other hand, winter presents the higher proportion of surface precipitation (63%). During all seasons, Z_e frequencies are highest close to the ground (compared to DDU) and the percentage of observations decreases as the altitude increases (see Figure 3.8). In winter, the occurrence of precipitation at high altitude levels is lower compared to the other seasons, similarly to DDU.

During all seasons at PE, mean and median VPV show a slight decrease along the vertical profile. Summer and autumn present a more steady decrease, compared with winter and spring, because the latter two decrease until above 1km, then W increase along the lower km. These breaks in the VPV signatures are associated with the reflectivity of shallow precipitation event that are present in all seasons with low frequency, but enough during JJA and SON to impact the shape of the VPV. These shallow profiles of precipitation are characterized by very low to negative values of W at the top, followed by an increase toward the surface.

3.5.2 Virga

Values of reflectivity factor and vertical velocity at DDU shown in Figures 3.9 exhibit similar patters in all the seasons, mean VPR decreases rapidly in the lowest 1 km towards the surface. For the cases of VPS at DDU, it shows an increase towards

the surface. On the other hand, at PE, the seasonal values of reflectivity also decrease near to the surface, similar to the shape of the vertical profiles at DDU (see Figure 3.10), however mean and median VPV are relatively constant along the vertical path.

There is a seasonal variability at the two stations, with virga more frequent in summer and autumn compared to winter and spring (see Table 3.1). The differences in proportion of surface precipitation and virga observed during the season at DDU can be explained due to the seasonal variability of the air temperature. Figure 3.6a presents the air temperature (T) for surface precipitation (solid-lines) and virga (dashed-lines) based on synchronous radio soundings - MRR profiles at DDU. According to Clough and Franks (1991) and Maahn et al. (2014), relatively warm air (as the case of summer) and low relative humidity lead to more sublimation of ice particles. Relative humidity, plays an important role in the sublimation of the particles, but in the case of DDU, relative humidity with respect to ice (RH_i) shows no clear seasonality (See Figure 3.6b). Although during summer the moisture content in the troposphere is higher compared to winter, RH_i decreases as the temperature increases. Figure 3.6b displays the RH_i for virga and surface precipitation, showing that virga profiles are characterized by less saturated conditions compared with surface precipitation, with a difference in RH_i between 10 and 35%.

3.6 Summary and conclusions

In this study we present a multi-year characterization of the vertical structure of precipitation at two stations in East Antarctica, using vertical profiles of reflectivity (VPR), vertical velocity (VPV) and spectral width (VPS) from micro rain radars. The shape of these vertical profiles suggests the influence of the climatological patterns that impact on precipitation processes at the two stations. The coastal location of DDU provides relatively warmer and moister conditions than at PE, which is located at a higher altitude in the escarpment zone. Analyzing the statistical distribution of the long term observations of the VPR and VPV demonstrated that at DDU there is a higher occurrence of more intense precipitation events with larger vertical extent than at PE. Higher frequencies of large Z_e and W values at DDU compared to PE were used as a proxy for the occurrence of intense precipitation. The strong katabatic winds blowing at DDU have a significant impact on the VPR due to a low-level sublimation process. Topographic conditions at PE protect the station from the direct impact of katabatic winds and from strong sublimation of

precipitation near the surface.

Two contrasted shapes of VPV are observed in the study areas, influenced by the microphysics of ice particles and the lower tropospheric conditions. Although both stations are characterized by the presence of small ice particles during snowfall events, relatively warmer and moister conditions at DDU favor the occurrence of aggregation and riming of crystals, increasing the mean vertical velocity toward the surface. On the other hand, the cooler and drier conditions at PE limit the ice-growing processes, leading to a more uniform VPV, with even a decrease towards the surface due to the increase in air density.

The multi-year observations show that virga is a frequent phenomenon in the study areas, corresponding to 36% and 47% of all precipitation profiles at DDU and PE. The vertical profiles of virga are characterized by lower values of radar reflectivity and associated with drier and warmer atmospheric conditions. At both stations, significant differences in the shape of the VPR of surface precipitation were observed when the virga profiles were included. This takes particular importance in the calibration and validation of satellite products for the monitoring of precipitation, because the blind zone limits the differentiation of surface precipitation from virga. Virga appears more frequently in summer, when most of the observation in Antarctica are carried out because of logistical reasons. Winter is the season when virga is less frequent and precipitation events are shallower compared to the other seasons.

The present study explores unique datasets of micro rain radar measurements, which demonstrate a great potential for long-term monitoring of the vertical structure of precipitation in a remote region as Antarctica. Nevertheless, it is necessary to extend this analysis to additional locations across the continent (once large enough datasets become available), in order to improve the characterization of the vertical patterns of precipitation in different geographical conditions. Moreover, new intensive field campaigns to collect more detailed information on microphysics of hydrometeors also are important to improve the interpretation of the results. Current statistics and future measurements will contribute significantly to better understand the Antarctic precipitation and to evaluate satellite products and verification of numerical precipitation models.

Chapter 4

The vertical structure of winter precipitation using ground-based radar observations at Col de Porte, French Alps

Abstract

Space-borne active and passive microwave remote sensing observations have a great potential to provide information about the spatial variability of the precipitation in the Alpine region. However, as they do not take measurements near the surface (e.g. because of ground-clutter contamination in the case of radar systems), gridded retrievals are affected by systematic error due to the vertical variability of precipitation near to the ground level. In this chapter, we present an analysis of the near-surface vertical structure of Alpine precipitation during winter, using a ground-based K-band vertical-profiling micro rain radar and in-situ weather observations at the experimental monitoring site Col de Porte in the French Alps. The vertical profiles of the first three Doppler moments, the effective radar reflectivity factor Z_e, mean Doppler velocity W and spectral width σ_v were analyzed between 225 m and 2.25 km above the ground level. Solid and liquid precipitation were separated using temperature thresholds and evaluated with a classification of precipitation particles derived from a present weather sensor. Because its importance for the vertical variability of precipitation, profiles of virga (i.e. precipitation that does not reach the surface due to sublimation/evaporation) were detected using radar observations and

analyzed separately from ground precipitation profiles. The results show that the classification from the disdrometer is consistent with the snow-rain and virga-surface precipitation classification. Vertical patterns of snow virga and surface precipitation are similar to those observed in other regions, such as in Antarctica (Chapter 3), however with a lower portion of virga events equal to 15%, compared to 36% and 47% observed in the Antarctic coast and inland of East Antarctica, respectively. Sublimation in arid regions (e.g. Sahara Desert) presents over 50% (30%) using CloudSat (TRMM and GPM) for previous studies. Near-surface mean relative humidity for virga was lower than surface precipitation, but only for snowfall was statistically significant (p-value < 0.05), while vertical profiles of reflectivity and vertical velocity presented dependence on temperature only for surface precipitation, suggesting the effects of ice aggregations processes. This work is a contribution to the study of atmospheric phenomena that influence the vertical structure of precipitation near the surface, such as virga. The findings are useful for a better understanding of precipitation in the alpine region, as well as providing important information for the evaluation of satellite products and models.

4.1 Introduction

High resolution information in the spatial and temporal dimensions is key to understanding the precipitation processes and its relationship with the environment. In mountainous regions, in-situ measurements are scarce and scattered and satellites provide a solution to monitor the spatial variability (Steger et al., 2013). Satellite products have several factors of uncertainties, including the vertical variability of precipitation, especially near to the surface where active microwave are spoiled due to ground clutter contamination (Surussavadee and Staelin, 2011; Maahn et al., 2014). On the other hand, for the case of ground-based radars, high elevation angles are used to avoid ground clutter and beam blocking in regions with abrupt topography, leading also to the lack of information near the surface (Germann et al., 2006). Ground-based vertically pointing radars, as micro rain radar (MRR), allows us to monitor the vertical structure of precipitation near the surface, providing crucial information to evaluate other remote sensing products.

The vertical profiles of radar variables, especially the radar reflectivity, has been studied to understand for instance the variability of the 0°C isotherm; the hydrometeor growth processes, such as aggregation, collision and coalescence; or the evolution of snow/rainfall rates towards the surface to correct precipitation estimations (e.g.

Rakovec, 1997; Vignal et al., 2000; Snow et al., 2012; Welsh et al., 2016). The change of precipitation phase due to sublimation in case of snowfall or evaporation in case of rainfall, has also been an important research issue, due to its implications to the redistribution of heat and moisture in clouds (Smith et al., 2003), and because of the uncertainties that it produces in microwave retrievals of surface precipitation rate (Surussavadee and Staelin, 2011).

The extreme case of precipitation sublimation/evaporation, virga, was studied previously using active microwave instruments, demonstrating that virga is a process that occurs widely in different regions (e.g. Geerts and Dejene, 2005; Evans et al., 2011). Virga is a component that is usually not explicitly included in modeling system for moisture source estimations (Gangoiti et al., 2015). Recently, sublimation of precipitation and virga observations have been carried out using ground-based radar observation in extreme region as Antarctica (e.g. Grazioli et al., 2017b; Durán-Alarcón et al., 2019) and also at global scale using spaceborne radar satellite data, excluding the polar regions, focusing the analysis on arid lands by Wang et al. (2018).

In the present work, we investigate the vertical variability of the lowest layers of winter precipitation in the Alpine region using a MRR and in-situ observations. The chapter is structured as follows: the section 4.2 presents the material and methods, including the description of the study area, datasets and the classification of precipitation, section 4.3 provides the results of the snow - rain and surface precipitation - virga classifications and the analysis of the vertical structure; finally, the summary and main conclusions are presented in section 4.4.

4.2 Material and methods

4.2.1 Study area

This study is based on data collected at the research station Col de Porte (CDP), located at 1325 m a.s.l. in the Chartreuse mountain range, French Alps (45°18'N, 5°46' E). The information relative to this station is detailed in Subsection 1.4.1. This experimental site was part of the World Meteorological Organization Solid Precipitation Inter-Comparison Experiment (WMO-SPICE), aiming to compare manual and automated methods for snow precipitation and observations of snow on the ground (snow height and water equivalent) (Morin et al., 2013). See in Figure 1.7 the distribution of snow measuring instruments located at CDP during winter. Figure 2 of

general introduction displays the location of the station on a map.

4.2.2 Data

All details regarding the instruments at the station are presented in Chapter 1 Subsection 1.4.2. Data from a micro rain radar located at CDP was used to analyze the vertical profile of precipitation, with a vertical and temporal resolution of 75 m and 1 minute, respectively. Profiles were aggregated to 1 h resolution, according a similar analysis presented in Subsection 3.2.5.

The period of observations corresponds to two winter campaigns with continuous MRR observations between January 14 and March 21 2014, and February 12 and April 8 2015 (see Figure 4.1). Additionally, in-situ weather information was used to separate snowfall from rainfall and to evaluate the final results of classification: air temperature T_{2m} at 2 m above surface (in degree Celsius), snow gauge measurements of precipitation (in mm h^{-1}).

An hourly classification of the phase (i.e. snow, rain and mixed phase) of precipitation events based on temperature thresholds was available at the station, which defined an upper threshold for pure snow equal to 0°C and a lower threshold for pure rain corresponding to 2°C. Precipitation between 0 and 2°C was examined by a meteorologist of MeteoFrance using additional information, corresponding to measurements of surface albedo, shortwave and longwave radiation, surface temperature, among other weather data, and finally the precipitation was classified as rain, snow or mixed phase.

Information about relative humidity RH near the surface level was used to analyze the different types of precipitation profiles in the subsection 4.3.4.

4.2.3 Method

In the Alpine region at the elevation of Col de Porte station, precipitation in form of rain can occur at ground level during winter (Bartolini et al., 2009). It is important to separate both types of events before analyzing the vertical profile of precipitation, because different cases exhibit known differences in the vertical pattern, such as the case of the presence of a bright-band in the melting layer region during stratiform rainfall events, due to an enhancement of the backscattering of the melted surface of solid hydrometeors (Fabry and Szyrmer, 1999).

On the other hand, the vertical profiles of precipitation were classified in two different categories based on whether the precipitation reaches the surface (called

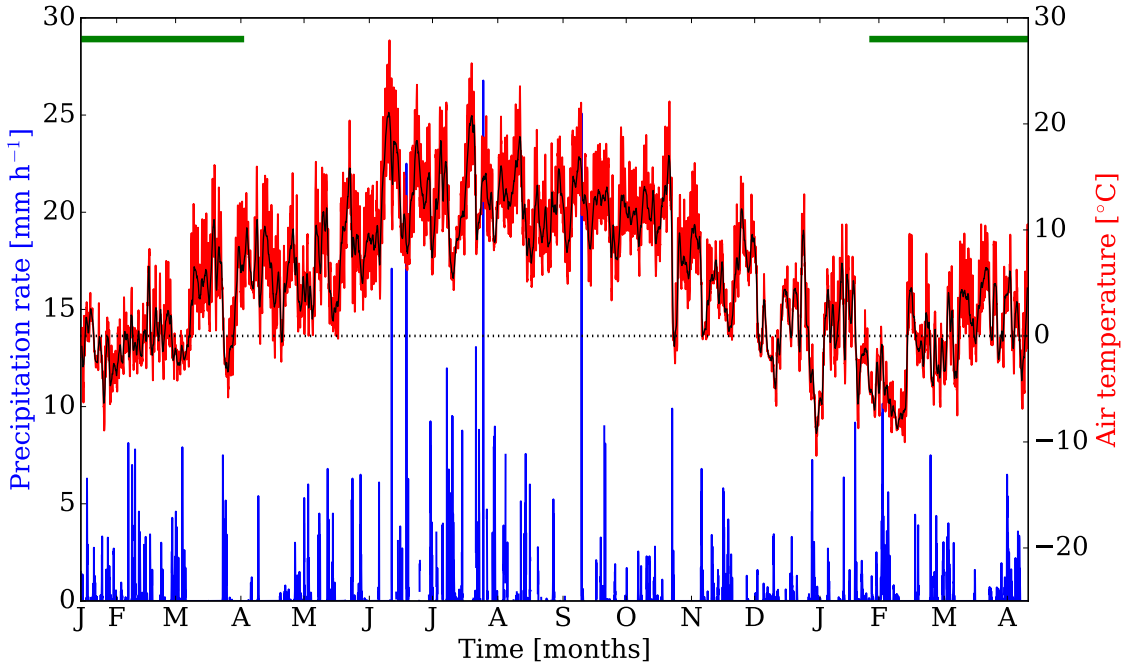

Figure 4.1: Micro rain radar and in-situ precipitation and temperature observations at Col de Porte station, during the period of study (January 2014 to April 2015). Blue line corresponds to snow gauge observations; red line is the air temperature at 2 m; black line is the respective daily moving average; dotted line marks the 0°C limit; and green lines correspond to the period with MRR observations.

surface precipitation) or not (called virga). Snowfall sublimation depends on both the properties of the solid hydrometeors (e.g. bulk density, terminal velocity and particle size distribution) and meteorological conditions (e.g. relative humidity, temperature) (Clough and Franks, 1991; Maahn et al., 2014). Sublimation of snow particles plays an important role in the air mass transformation in orographic precipitation taking latent heat from the surrounding atmosphere (Smith et al., 2003), and together with evaporation of liquid droplets are one of the reasons for overestimation of surface precipitation from space (Surussavadee and Staelin, 2011).

The description of the snowfall-rainfall and virga-surface precipitation classifications is presented below.

4.2.3.1 Snowfall - rainfall precipitation classification

At Col de Porte station, a classification of the phase of precipitation at the surface level is available for each hour during the period of study based on temperature thresholds for solid, liquid and mixed phase. This information is useful to separate snowfall from rainfall events, when precipitation reaches the surface. We checked the ranges of temperature of the classification to define the threshold of air temperature (T_{2m}) for snowfall and rainfall/mixed-phase events, in order to determine if a profile corresponds to snowfall or rainfall, even if no precipitation is observed at the ground level.

Figure 4.2 shows the empirical distribution of T_{2m} separated according to the classification of solid, liquid and mixed phases of precipitation at Col de Porte. Snow and rain show a very narrow region of overlapping between the two phases of precipitation. The distribution of mixed phase precipitation extends from -0.2 to 1.9°C. These temperature values were used as the upper limit for the occurrence of pure solid precipitation and the lower limit for the occurrence of only liquid precipitation, respectively. A sensitivity analysis of the virga occurrence shows that these thresholds are not very sensitive for value down to -2°C for snow and up to 4°C for rain, however temperature does affect the vertical profiles of reflectivity and vertical velocity (discussed in detail in Section 4.3.4). The common range of temperature values were removed from the analysis to avoid mixed precipitation at ground level.

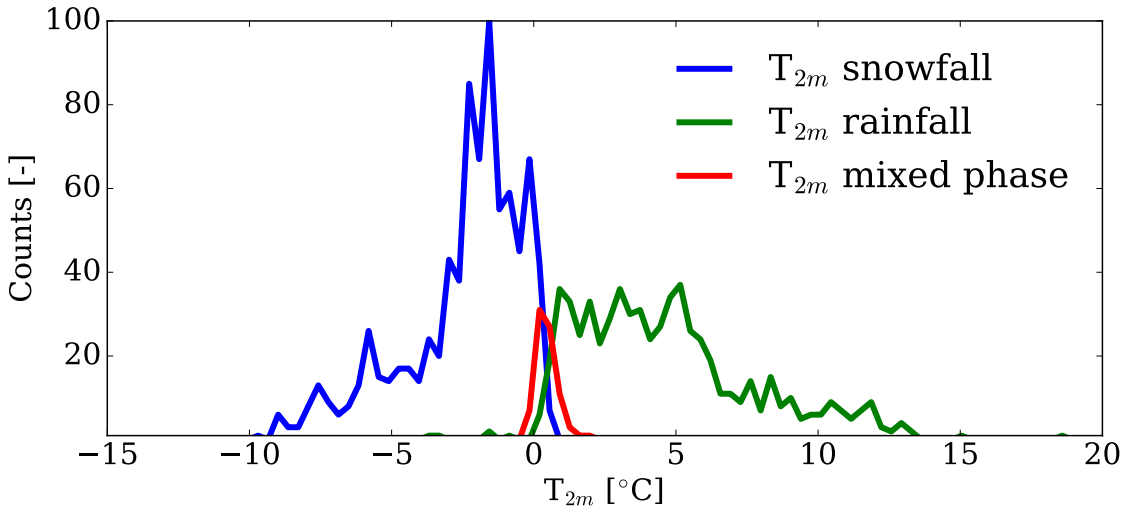

Figure 4.2: Histograms of air temperature at 2 m during snowfall (blue line), rainfall (green line) and mixed phase observations at Col de Porte (red line).

4.2.3.2 Virga - surface precipitation classification

The presence of precipitation signal at the lowest reliable MRR range gate of each profile was used to discriminate virga from surface precipitation. Occurrence of echoes at 225 m height above the ground level was used as reference of surface precipitation (as in Durán-Alarcón et al. (2019)). MRR is especially suitable to detect hydrometeors that have reached a sufficient size to fall as precipitation, including streaks of virga, but it is insensitive to cloud particles (Gorodetskaya et al., 2015; Souverijns et al., 2017).

4.3 Results

4.3.1 Comparison of snow-rain and virga-surface precipitation with disdrometer classification

In order to evaluate the classification of snowfall and rainfall using thresholds on T_{2m}, a particle classification derived from a PWS100 disdrometer (present weather sensor) located at Col de Porte during the period of study was used. One output of the PWS100 classification is the present weather code of the National Weather Service of USA (NWS), which corresponds to the categories listed in Table 4.1. The classification algorithm of PWS100 is a decision tree system that uses fuzzy logic tables to analyze different properties of the hydrometeors such as the size, falling velocity and environmental conditions such as temperature, relative humidity, in

order to determine the type of particles (CS Inc., 2014). From this list of categories, ice pellets, ice crystals and hail were not detected by the disdrometer when it was co-located with MRR. The information from the disdrometer was also used as an independent reference about precipitation occurrence to evaluate the method proposed for the virga-surface precipitation classification.

Figure 4.3 shows the distribution of the particle classes provided by the PWS100, separated by snowfall and rainfall, and by surface precipitation and virga. The percentage of occurrence of each hydrometeor corresponds to the number of times a given type was observed with respect to the total number of hydrometeors detected during the period that the PSW100 was co-located with the MRR, based on observations at 6-minute resolution.

For the case of snowfall, when precipitation is detected by the lowest available range gate of the MRR, the disdrometers classified most of the time the particles as S (snow) or other solid precipitation particle, while no liquid particles were observed. It is noteworthy that an important part of the observations are classified as unknown precipitation (P) or clear sky situation. In the latter case, corresponding to about 20% of the time, two main reasons may explain this result: (1) the miss-detection by the disdrometer and (2) as the lowest available range gate of MRR is located at 225 m, what it is observed at this height can still sublimate on its way to the surface, which in this case could be associated with an underestimation of virga events.

For the case of snow virga, most of the observations were assigned to clear sky by the disdrometer, while a reduced percentage corresponds to unknown precipitation particles, which may be associated to very small particles that were not detected by the MRR and at the same time unable to be identified by the disdrometer. On the other hand, the fact that only during snow virga a few observations were classify as P, suggest the presence of blowing snow. In general, these results are consistent with the expectation of absence of precipitation particles during virga profiles.

For rainfall events, R (rain) is the dominant class according to the disdrometer data, however a significant part of the PWS100 observations were included in the category of clear sky. Moreover, a very small percentage was classified as snow, which could be associated to a possible underestimation of the temperature threshold (1.9°C) to exclude all precipitation in solid form. The rain virga, again shows the same pattern of dominant clear sky classification.

These results show that the snowfall - rainfall classification using a threshold of in-situ air temperature is reliable to separate the main hydrometeor types of solid and liquid precipitation. However, limitations in the classification of the PSW100

Table 4.1: PWS100 NWS output codes. Source: CS Inc. (2014).

Name	Code
No precipitation	C
Unknown precipitation	P
Drizzle	L
Freezing drizzle	ZL
Rain	R
Freezing rain	ZR
Snow	S
Ice pellets	IP
Snow grains	SG
Ice crystals	IC
Hail	A

still remain, related to the uncertainty of particles classified as P (unknown precipitation). In the case of the surface precipitation - virga classification, MRR observations show a high performance detecting virga, some streaks that do not reach the surface were interpreted as surface precipitation because sublimation/evaporation below 225 m cannot be detected by the MRR. On the other hand, the undetection by the PWS100, either because of the presence of a very small size particles or because under-catching in the limited sampling area, may contribute to the occurrence of clear sky classification during actual precipitation profiles. According the PWS100, 20% of time surface snowfall precipitation corresponds to no precipitation, of which a part could correspond to virga. For the case of rain, this percentage increases to double.

4.3.2 Vertical variability of Doppler moments

The vertical variability of the first three Doppler moments derived from the MRR observations at Col de Porte station during two winter seasons is presented in this section. The precipitation profiles were separated into snow and rain close to ground, and then the joint distributions or 2D distributions of each radar variable with respect to altitude were calculated. Mean and median vertical profiles were computed, in addition to the 20^{th} and 80^{th} percentiles.

During the period of observations, a total of 585 hourly vertical profiles corresponding to snowfall events were collected. The results of each Doppler moment are discussed below. The main motivation of this study is to characterize the behavior

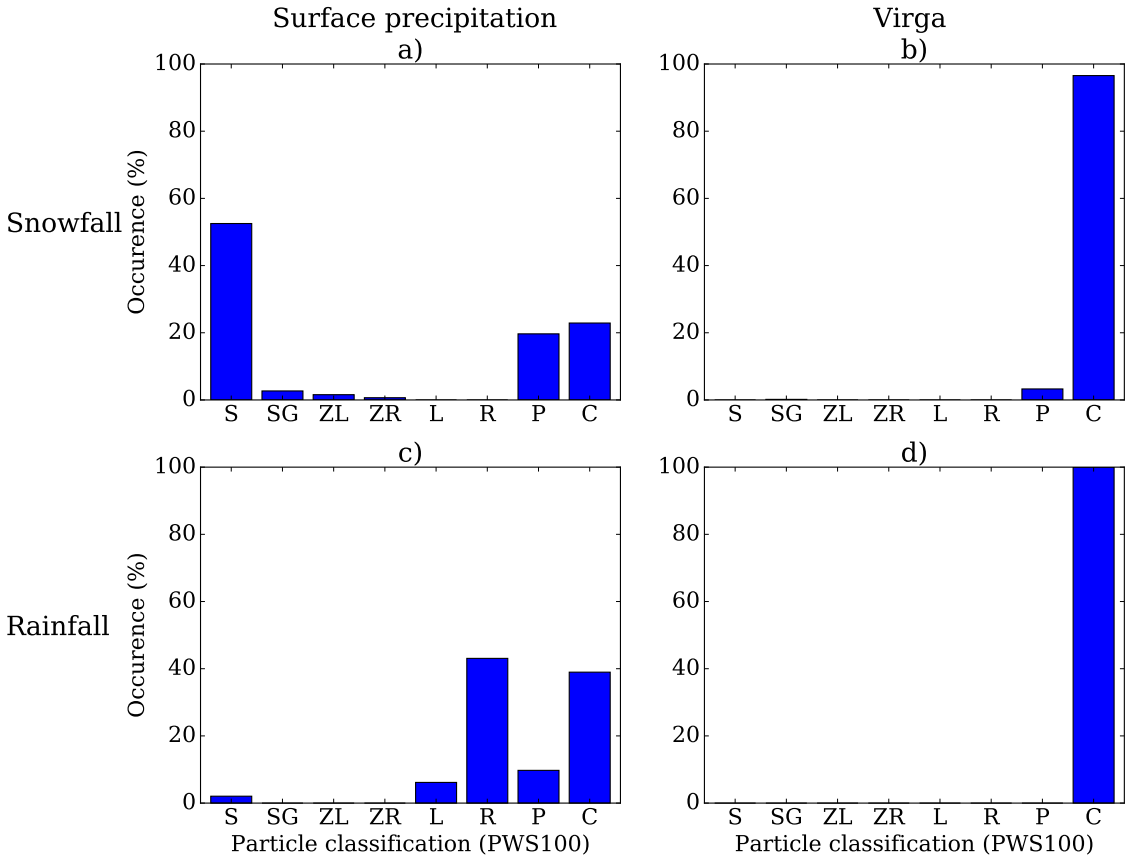

Figure 4.3: Distribution of Particle type derived from disdrometer (PWS100) information, separated by snowfall (a and b), rainfall (and d), virga (b and d) and surface precipitation (a and c). The classification is the following: S = snow; SG = snow grain; ZL = frozen drizzle; ZR = frozen rain; L = drizzle; R = rain; P = unclassified precipitation and C = clear sky.

of solid precipitation, however the results from liquid precipitation over the study period are also analyzed. For the case of rainfall, only 225 profiles were obtained during the two campaigns of observation, using the MRR. Although rainfall observations are shorter than snowfall observations and the signal can be strongly affected by attenuation, they are still useful to capture features that are only present during liquid precipitation.

4.3.2.1 Vertical profile of reflectivity

The vertical profile of reflectivity is an important radar output in the analysis of precipitation because it provides information related to the snow/rainfall intensity, since the relation between precipitation rate and Z_e can be expressed by a power law (see Section 1.2.5), and also because it reflects the dominant microphysical processes controlling precipitation.

During the period of observations, the profiles of radar reflectivity slightly increase towards the surface. In the case of rainfall reaching the surface (see Figure 4.4b), values of reflectivity are much higher than for snow. In the upper part of the profiles, the pattern remains steady toward the surface until 1 km height, and from there it increases rapidly towards the surface. This means that this is the average elevation of the melting layer, where solid particles start melting and become liquid, leading to a local increase in reflectivity (but not in rain rate).

4.3.2.2 Vertical velocity profiles

Vertical profile of vertical velocities during snowfall events show low variations with a slight positive trend toward the surface, low average values and narrow range of values as well. These features are clearly represented by the mean, median and quantiles (20 and 80%) profiles. Mean and median profiles present very similar patterns with a mean vertical velocity of 1.5 m s^{-1} near the surface (see Figure 4.4c).

Values of W are larger in the Alpine region, with a broader spectrum of values compared to the results observed in Antarctica (see Figure 3.3c and d). As for the vertical patterns, CDP shows a large difference with respect to DDU observations, due to the fact that on the Antarctic coast the vertical velocity profiles are strongly affected by the turbulence produced by the katabatic winds, whereas this does not occur with the same intensity and frequency in the Alpine station. In the case of Princess Elisabeth, as in CDP, both profiles are steady; however at Col de Porte there is no decrease in the vertical velocity towards the surface as at PE. This may

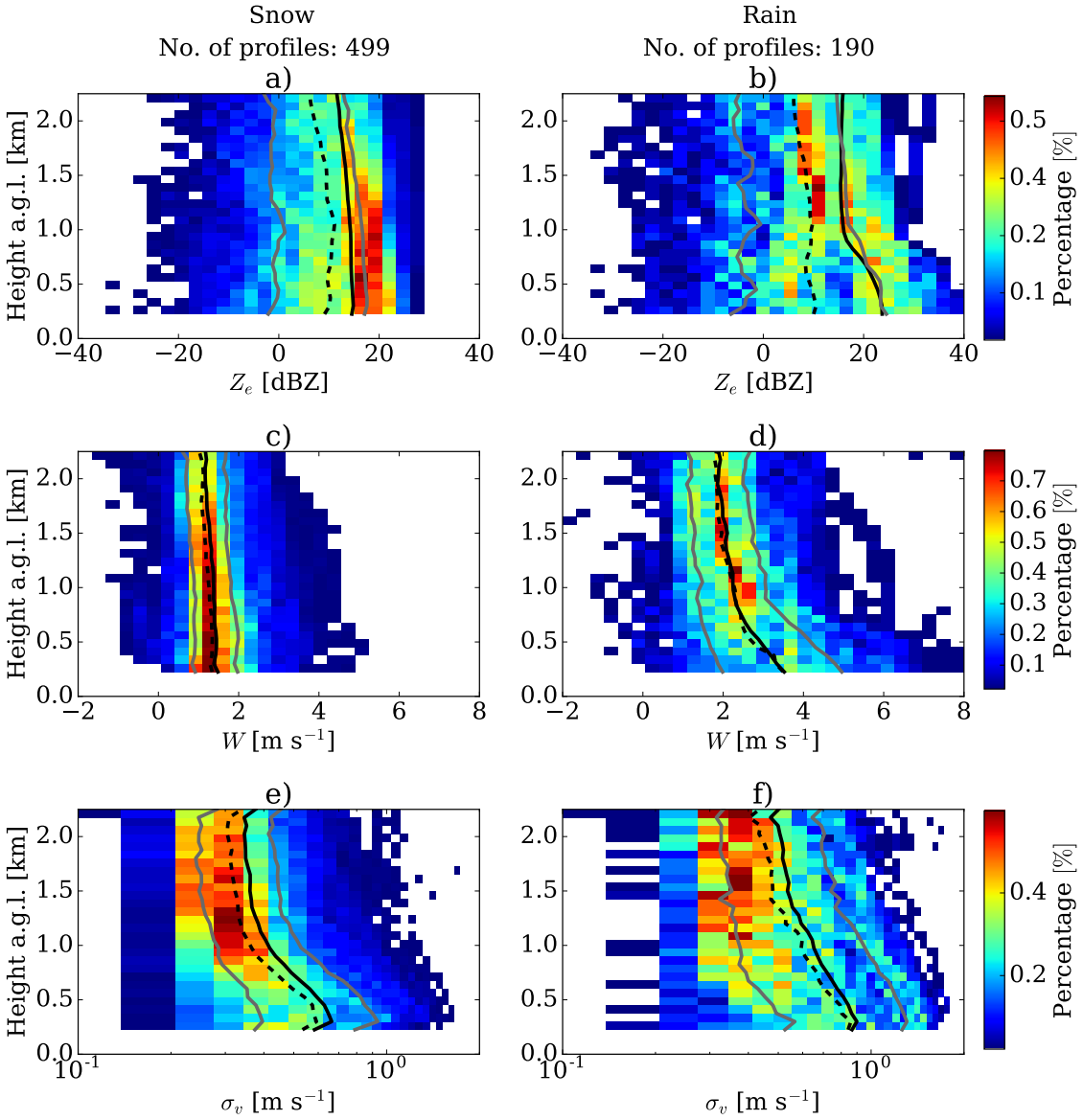

Figure 4.4: Frequency by altitude diagram for Z_e (a, b), W (c, d) and σ_v (e, f) values observed at CDP, separated by snowfall (a, c, e) and rainfall (b, d, f) reaching at surface. Solid-black and dashed-black lines represent the average and median vertical profiles of Z_e, W and σ_v respectively. Grey lines correspond to the 20 and 80% quantiles of the vertical profiles. σ_v values are plotted in log x-axis to highlight the variations for small values.

be because at CDP the increase of terminal velocities as the particles grow is more significant than the reduction on terminal velocity due to the small increase of air density, compared to PE. The observed higher and increasing velocities toward the surface are a signal of the process of particle aggregation in the Alps, because in warmer conditions this process is more frequent, considering that efficiency of aggregation is directly proportional to the temperature under subfreezing temperatures (Stewart et al., 1984).

Regarding liquid phase precipitation at the ground, vertical profiles show a completely different pattern compared to the ones observed during snowfall events (see Figure 4.4c). Below 1 km, average vertical velocities increase rapidly towards the surface, from 2 to 3 m s^{-1} , the double of the speed observed of snow particles. In this case, the range of values also increases, considerably. This behavior is consistent with the presence of a melting layer below 1 km, which produces a greater diversity of particle types and vertical speed in the radar contributing volume.

4.3.2.3 Vertical profile of spectral width

Spectral width is a useful radar variable to understand the effects of turbulence on the behavior of falling hydrometeors, because it provides a measure of the dispersion of the vertical velocities reported by the Doppler spectrum (Bohne, 1982), but is also associated with the variety of particle types and their respective terminal velocities.

In the case of Col de Porte observations, increasing spectral width toward the surface occurs in both snowfall and rainfall events (see Figure 4.4d). In the case of snowfall, spectral width increases mainly in the lower part of the profile, which may be associated with an increase in the diversity of particle sizes and types (e.g. due to particle aggregation processes as the temperature increases) that generate a wider velocity spectrum which means a larger spectral width. With respect to rainfall events, spectral width values increase more steadily, but from a higher altitude compared to the profile of snowfall events (see Figure 4.4e). Although the vertical structure of the equivalent reflectivity factor Z_e and the vertical velocity W suggest that the melting layer is located at an average height of 1 km, it may fluctuate in altitude, causing a larger variability of vertical speeds above 1 km, which would explain the spectral width increases towards the surface from high altitude. In fact, the occurrence of rainfall events with near surface temperatures greater than 10°C (see Figure 4.2) are an indication of a higher melting layer.

4.3.3 Surface precipitation and virga occurrence

The occurrence of precipitation according to whether the precipitation reaches the surface or if it sublimates/evaporates completely before being observed by the MRR at the lowest level available is discussed in this section.

During the two seasons of observations, a total of 499 profiles of surface snowfall were collected using the MRR observations. This corresponds to 85% of the total number of solid observations and means that 15% of the rest of the profiles (snow virga) does vanish before reaching the surface. The important presence of virga may have implications with respect to the remote sensing of precipitation from space, since most of the radar instruments on board of satellites (e.g. CloudSat) measure the precipitation aloft, and cannot see below the first kilometer, because the ground surface acts as a clutter that contaminate the microwave signal in the near-region, leading to an overestimation of the surface observations. In the case of spaceborne passive radiometers that are used to produce global precipitation maps (e.g. Global Precipitation Climatology Project (GPCP)), that measure radiance/brightness temperature at the top of the atmosphere to estimate precipitation may also misidentify virga profiles (Wang et al., 2018). On the other hand, the study of virga is an important subject for ground-based radar remote sensing, especially in mountainous regions, where the minimum elevation angle of 3D volumetric scanning radar system is restricted to avoid ground clutters, leading to a loss of observations near the surface as the distance to the radar increases.

In the case of rainfall, occurrence of virga presented similar frequency as during snowfall events, equivalent to 15% of the time. In general, the vertical patterns of virga and surface precipitation are similar to those observed in other regions, such as in Antarctica, however with a lower proportion of virga events equal to 15%, compared to 36% and 47% observed in the Antarctic coast and the interior of East Antarctica, respectively using the same type of radar (Durán-Alarcón et al., 2019). Wang et al. (2018) who studied the occurrence of virga at the global scale (excluding polar regions), using the radar instruments on board of CloudSat, the Tropical Rainfall Measurement Mission (TRMM) and the Global Precipitation Measuring (GPM), found that virga is detected over 50% of the time by CloudSat, while over 30% of TRMM and GPM profiles in arid zones (e.g. Sahara desert). The considerable higher sensitivity of CloudSat (-30 dBZ) compared to TRMM (17 dBZ) and GPM (12 dBZ), are the main explanation to the differences in virga occurrence observed between them. In the case of CloudSat, a threshold of -15 dBZ is used to

detect precipitation clouds (Haynes et al., 2009; Wang et al., 2018).

Finally, Figure 4.5 shows the vertical variability of the Doppler moments for virga separated by snow and rainfall. These patterns are characterized by a strong decrease of radar reflectivity towards the surface from an elevation of 1.5 km, while vertical profile of vertical wind and spectral width remains steady along the path, with high variability/dispersion because of the low number of observations. At this point, variations of the profiles are significantly different from those of surface precipitation. The low level variations of the vertical structure of the precipitation, in both phases, is certainly a feature that radars from space cannot fully capture, thus these observations provided from surface become a valuable input to assess the reliability of satellite precipitation products.

4.3.4 Temperature and relative humidity

Considering that we do not have data from radio soundings during the period of study at Col de Porte station, we analyzed the air temperature and relative humidity using in-situ weather data.

Results show negative mean temperature during snowfall events, with a slightly higher value for the period of virga profiles. Virga show lower relative humidity with respect to ice RH_i compared to surface precipitation. For the case of rainfall, temperature of virga and surface precipitation were similar, while virga also presented lower relative humidity (RH_w) compared to surface precipitation (see Table 4.2).

We performed the Mann-Whitney U (MWU) non-parametric statistical test to check if there are statistically significant differences between the two types of profiles, considering that time series of virga and surface precipitation are short and unpaired, and that MWU does not require any assumption about the distribution (Gooch, 2011). The test shows that the differences in temperature were not significant for snowfall and rainfall, with p-values (the probability of the hypothesis that no significant differences are observed between the datasets) equal to 0.98 and 0.43, respectively. For the case of relative humidity, only differences between snow virga and surface snowfall are significant, with a p-value equal to 0.0001, while for the case of rainfall it is 0.89.

Using these values as a proxy for the conditions of the atmosphere during the precipitation events, we can say that humidity is an important parameter for the occurrence of virga in solid form, however longer period of data are necessary to obtain more robust statistics. The high relative humidity observed in this station, may

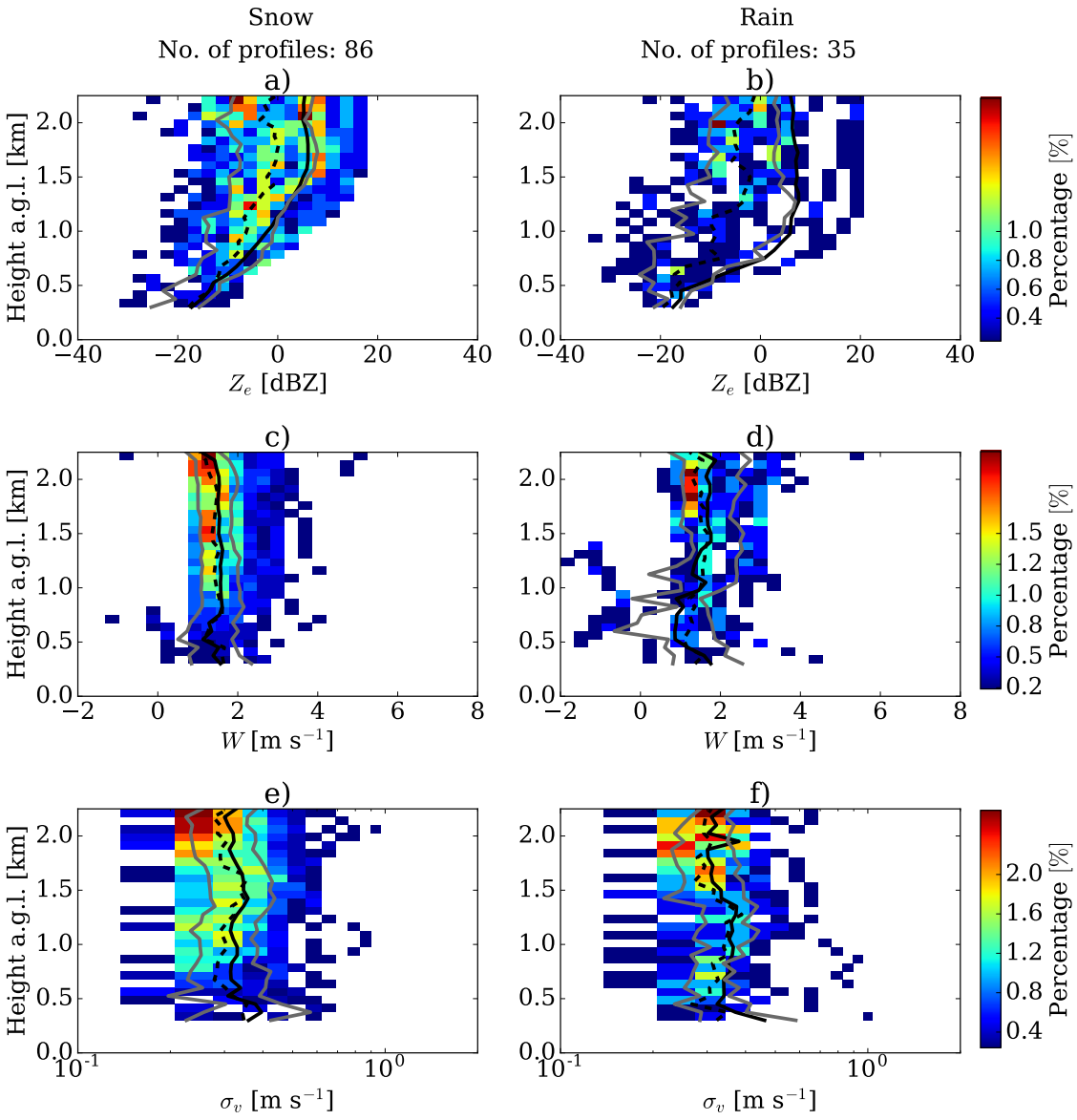

Figure 4.5: Same as Figure 4.4, but only for virga precipitation.

Table 4.2: Air temperature and relative humidity at 2 m, during virga and surface precipitation, separated by snowfall and rainfall events. Relative humidity for snowfall events corresponds to RH_i and for rainfall events to RH_w (see Appendix B).

Phase	Type	Air temperature (std) [°C]	Relative humidity (std) [%]
Snowfall	Surface	-2.4 (1.0)	97 (2.5)
	Virga	-2.3 (1.3)	92 (5.0)
Rainfall	Surface	2.0 (0.5)	88 (10.0)
	Virga	2.0 (2.0)	87 (6.1)

be an important reason for the lower occurrence of virga precipitation, compared with those observations carried out in dryer regions (e.g. Durán-Alarcón et al., 2019; Wang et al., 2018).

To evaluate the influence of the near surface temperature on the vertical distribution of the Doppler moments of snowfall events, a sensitivity analysis of the upper threshold of temperature is carried out. The mean vertical profiles of Z_e, W and σ_v and the respective 20 and 80% quantiles were computed for surface snow and snow virga considering different temperature thresholds (see Figure 4.6). In addition to the original threshold used to classify snowfall, two other values were tested equal to -1 and -2°C. These two extra values of temperature include 451 and 263 profiles, respectively. For threshold values lower than -2°C, the number of profiles decreases considerably, but some examples can be found in Appendix E. Figure 4.6 shows that Z_e and W both decrease as temperature decreases. This behavior illustrate that temperature is important in processes such as the aggregation of particles that lead to an increase of the vertical velocity and reflectivity observed by the radar. In the case of virga events, variations on the temperature threshold seems to not affect significantly the vertical distribution of Z_e and W.

In the case of spectral width, in none of the cases (snow or rain) it is possible to observe a clear relationship between the vertical profile and the temperature threshold.

4.4 Summary and conclusions

In the present work, the vertical structure of winter precipitation at Col de Porte in the French Alpine was analyzed using a ground-based vertical-profiling micro rain radar and in-situ weather observations. Ground-based precipitation classification

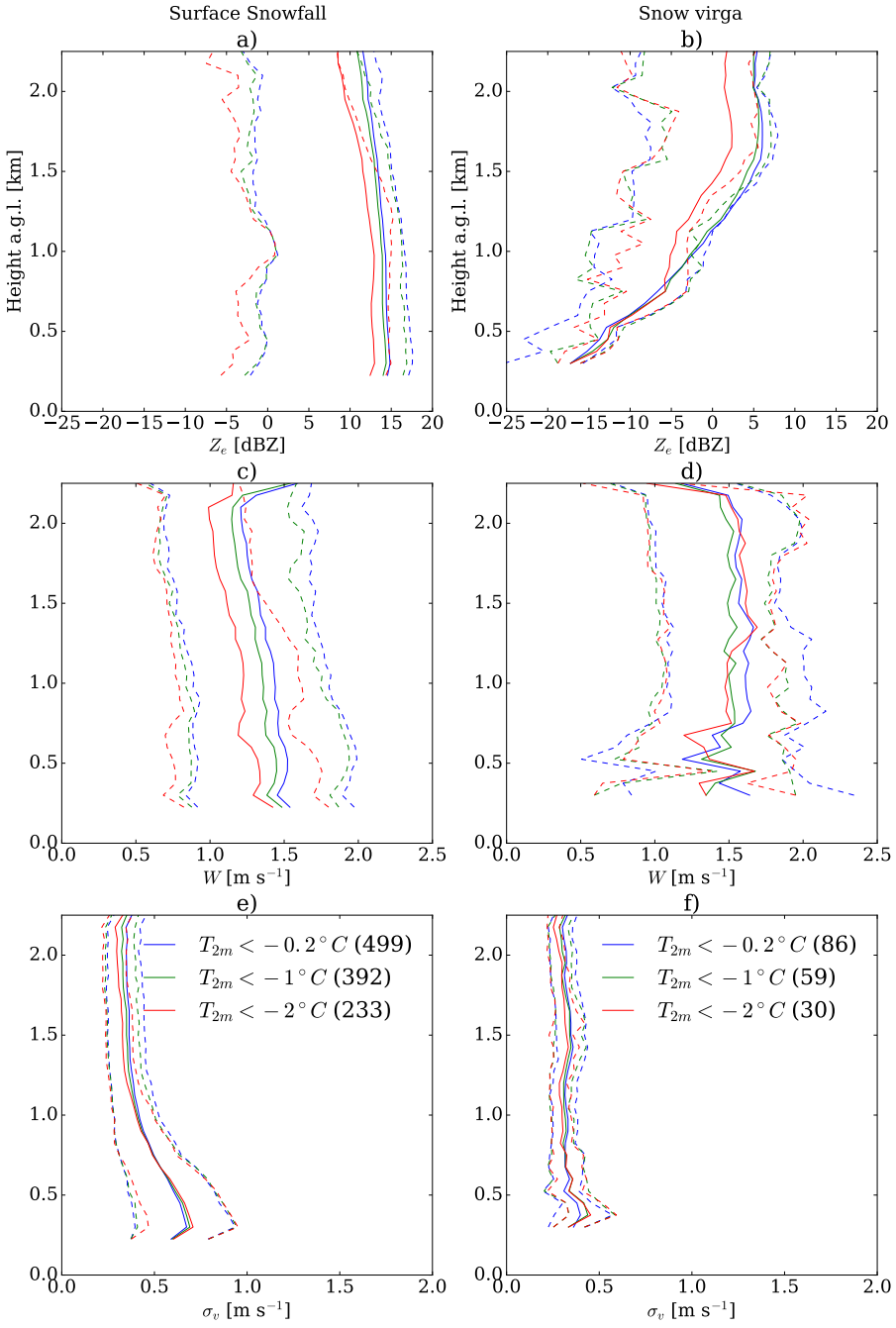

Figure 4.6: Vertical profiles of Doppler moments using different thresholds on the temperature: <-0.2, <-1 and <-2°C. a and b correspond to Z_e, c and d to vertical velocity and e and f represent σ_v. In the legend, the number inside the parentheses indicates the total of snow or virga profiles for the given threshold.

and near surface temperature were used to discriminate between the solid and liquid phase of precipitation at ground level. The lowest available radar signal was used to determine whether the hydrometeors reach the surface or not, separating the profiles in surface precipitation and virga.

Using the independent hydrometeor classification derived from the disdrometer PWS100 during the SPICE experiment, the method to separate snow and rain and the classification of virga and surface precipitation were evaluated. Results showed that the classification presents a high performance discriminating solid from liquid particles and detecting virga episodes. Because precipitation below the lowest MRR reliable gate can still experience sublimation, some limitations may lead to the potential underestimation of virga events.

The main patterns of vertical profiles of snowfall reaching the surface level show a slight increase of radar reflectivity towards the ground with a steady but increasing profile of vertical velocity, with an average W equal to 1.5 m s^{-1} at the lowest available altitude, higher than the approximated 1 m s^{-1} observed in the Antarctic region. These signatures are consistent with the presence of a more efficient aggregation process that leads to an increase of size and terminal velocity of the solid hydrometeors, which would be expected in more temperated climates as mid-latitude regions. A higher variability of the vertical velocities is also observed in the vertical profiles of spectral width, which describes a strong increase near the surface. The vertical patterns of Doppler moments during rainfall events show larger values of reflectivity and vertical velocity, typical of liquid precipitation particles. The average elevation of the melting layer is observed at 1 km from the ground level, where W experiences a significant increase towards the surface. The vertical variability of the spectral with and the near surface temperatures observed at Col de Porte during winter rainfall events, suggest the presence of few warmer precipitation events with highest melting layer elevation leads to larger values of σ_v in the upper part of the profiles.

The analysis of the vertical profiles of virga shows that most virga events sublimate completely below 1.5 km, showing a fast decrease of the Z_e signal. Both snow and rain profiles show a virga occurrence equal to 15%. These results are lower to those observed in dryer regions as the case of Antarctica (36% and 47% observed in the Antarctic coast and the interior of East Antarctica, respectively), or in the Sahara desert (over 50% with CloudSat observations). Unsaturated conditions are key for the occurrence of virga.

This work is a contribution to the study of important atmospheric phenomena

that affect the variability of the vertical structure of precipitation near the surface. The analyses carried out in this work, are useful for a better understanding of the products of precipitation satellites in the Alpine region. In addition, detailed informations near the surface are fundamental to evaluate ground-based radar products in mountainous regions, where configurations with high elevations angles lead to a lack of low level observations as the distance to the antenna increases.

Conclusions and perspectives

Conclusions

Antarctica and Alps are two regions of the planet that present significantly different climates and geographies. However, both have a distinctive element in common: the occurrence solid precipitation. This component of the hydrological cycle is of great importance both on a global and regional scale. In Antarctica, it is the main positive term in the surface mass balance equation, hence it plays an important role on the variations of the average long-term global sea-level rise; whereas in the case of the Alps, the solid precipitation is stored in the form of snow cover or mountain glaciers, allowing economic activities and ensuring fresh water during the summer months, favoring the development of ecosystems and society.

The study of solid precipitation presents complex challenges due to the difficulty of monitoring and quantification. Traditional methods to measure precipitation are strongly affected by wind conditions, which reduce the efficiency of capture by snow gauges, while on the other hand it also produce an increase in false measures by the incorporation of drifting/blowing snow from the surface. These difficulties, coupled with the limited access in remote areas such as Antarctica and high altitude regions such as the Alps, generate scarce observations and understanding of precipitation in these environments. That leads to a great uncertainty in the characterization of precipitation in models. In a scenario of global change, both global temperatures and precipitations are expected to increase, according to most CMIP5 models, but with large discrepancies between projections.

Active remote sensing (radar and lidar) from space offers a great potential for the monitoring of precipitation in regions with limited access, allowing to capture its spatial variability and also to observe and characterize the clouds, which are key in the precipitation formation. However, data from these tools presents limitations regarding to temporal resolution and lack of observations in the lowest height levels, due to ground clutter contamination (e.g. CPR radar) and strong signal attenuation

(e.g. CALIOP Lidar). Ground-based remote sensing, on the other hand, is a useful tool, which allows to monitor precipitation and clouds in the lowest troposphere, and provides information to validate satellite observations and numerical models. Because of that, the aim of this dissertation corresponds to the monitoring of precipitation at the near surface level, using both radar and lidar techniques, separating it into two specific objectives: 1) the characterization of hydrometeors in clouds and precipitation at Dumont d'Urville Antarctic station using a depolarization lidar, 2) the study the vertical variability of precipitation using micro rain radars on the coast and in the interior of Antarctica, and also in the Alpine region, at the Col de Porte station, located in the French Alps.

For Antarctica, information from two observatories of clouds and precipitation were used in this study, the APRES3 at Dumont d'Urville (DDU), on the coast of Adélie Land, and AEROCLOUD at Princess Elisabeth (PE), in the interior of Dronning Maud Land. For Alps, observations during two winter seasons in the framework of the WMO-SPICE project were collected in Col de Porte (CDP) station. The three observational datasets had in common the vertically-pointing K-band micro rain radar (MRR), among other weather data. In particular, a new 532-nm elastic depolarization lidar was deployed on the Antarctic coast to monitor the tropospheric clouds and precipitation.

With respect to the first objective of this work, innovative lidar techniques for detection and classification of clouds as well as precipitation hydrometeors were proposed at DDU. A background correction approach for profiles with strong remaining lidar signal in the far-range also was developed. The method of hydrometeor detection was based on the algorithm proposed by Gong et al. (2011), which uses a signal simplification approach and a series of criteria with respect to the slope and the relative maximum values of the signal to define cloud layers. The new approach includes information from MRR at the lowest available level to detect precipitation as well. A new development for hydrometeor classification based on the approach proposed by Yoshida et al. (2010) was presented, which takes advantage of the information from depolarization ratio, attenuated backscattering and the k-means cluster analysis algorithm to classify supercooled liquid water, 2-D (planar/oriented) and 3-D (randomly oriented) ice particles. This new approach was applied to almost one year of observations at DDU, identifying cloud and precipitation particles and their respective variability in the vertical profile. Cloud presented constant occurrence along the year, with the vertical distribution of clouds and SLW dominant between 1500 and 2500 m, and mainly constituted by 3D-ice. Concerning the profiles of pre-

cipitation reaching at surface level, 2D-ice was detected at all altitudes while most of 3D-ice particles were observed in the lowest elevations. The general vertical patterns SLW from a satellite-derived classification (DARDAR product) was quite consistent with the patterns observed with the lidar at DDU. This new classification technique using single wavelength elastic lidar provides useful information for the evaluation of satellite products. However there are still challenges regarding the method of comparison between vertical profiles from the surface and multiple profiles in the satellite track, in order to carry out an optimal quantitative comparison.

Regarding to the second objective, the vertical structure of precipitation was characterized using vertical profiles of reflectivity Z_e, vertical velocity W and spectral width σ_v derived from micro rain radars located at the Antarctic and Alpine stations. In the case of Antarctica, the vertical patterns of the Doppler moments exhibit strong relation with the different local climates that determine precipitation at both stations: the relatively warmer and moister conditions at the Antarctic coast (DDU), compared to the lower relative humidity at a higher altitude inland (PE). The long term analysis of the vertical profiles of reflectivity used as a proxy for precipitation intensity, shows that in DDU the occurrence of intense precipitation events are more frequent compared to PE. In the case of the vertical profiles of the Doppler moments at the Alpine station, despite the fact that they correspond to a shorter period of observations, averaged profiles of Z_e and W show characteristically higher values than those observed in Antarctica, explained by the presence of larger particles with faster falling speed.

Frequent and strong katabatic winds in the coast significantly affect the reflectivity profiles due to the sublimation of the particles as they approach the surface. This process is not observed in the PE, which is protected by the topography and neither in the Alpine station. In the same way, W and σ_v profiles are strongly affected by the presence of katabatic winds at DDU station.

From the analysis of the vertical profiles of W and σ_v, it is possible to ascertain that microphysical processes concerning ice particles play an important role in the near surface precipitation structure. The Antarctic snowfall particles are characterized by small size, but the relatively warmer and moister conditions at DDU favor the occurrence of aggregation and riming of crystals, increasing the mean vertical velocity toward the surface. These processes are limited at PE, because the colder and dryer the conditions. For the Alpine station, a strong dependence of the reflectivity and vertical velocity profiles on the temperature ranges at surface level was observed, suggesting that Z_e and W are affected by the efficiency of ice particle

aggregation, which depends directly on temperature for under-freezing conditions.

The analysis of virga occurrence in Antarctica revels that 36% and 47% of all precipitation profiles sublimate completely before reaching the ground at DDU and PE, respectively. In the case of CDP, this percentage corresponds to 15%, during the two winters of micro rain radar acquisitions. These results demonstrated that virga is a frequent phenomenon in the Antarctic stations, with occurrence that are close to those observed in extremely arid zones of the Earth (such as the Sahara Desert) with over 50% of virga events derived from CloudSat observations.This process of sublimation occurs mainly below 1 km of height for the Antarctic stations, while in the Alpine station was observed dominant below 1.5 km, corresponding approximated to the elevation of the CloudSat blind zone.

The present work explored unique datasets in a region where observations are scarce an scattered. It takes advantage of the combination of micro rain radar and lidar information to investigate the cloud and precipitation composition in the low level troposphere in Antarctica. It also analyzed the vertical structure of precipitation using Doppler moments and extends the analysis to the Alps, a region where solid precipitation is crucial, but still not completely understood. The results are useful for the calibration and the evaluation of precipitation satellite products, specially because of their limitations near the ground level. In the Alpine region, the results are useful to validate volumetric scanning ground-based radar products, often obtained with high elevation angles to avoid ground clutter, but making the observations near the surface more scarce (especially if the distance to the radar increases).

Perspectives

The work presented in this dissertation has obtained relevant information for the understanding of precipitation and its vertical structure derived from radar data. These information are useful as input for calibration and validation of satellite precipitation data and models. Moreover, there are other important investigations that have recently devoted their efforts in the research of the solid precipitation in the Antarctic region for the evaluation of models and satellite products (e.g. Tang et al., 2018; Souverijns et al., 2018b; Lemonnier et al., 2019). Nevertheless, the lack of in-situ observations, in the case of Antarctica, is still a major problem in this region. Thus, additional high-quality observations distributed in different locations are necessary (e.g. at the Plateau, Antarctic Peninsula, etc.) in order to characterize a

broad range of climatological patterns of Antarctic precipitation. An example of this type of observations is the precipitation at the Antarctic Plateau, where extreme cold and dry conditions determine the presence of very small ice particles, reduced amount of precipitation and the occurrence of processes such as diamond dust. In order to carry out this type of measurements, it will be necessary that collaborations between the different research groups that take part in the study of precipitation and Antarctic climate. The investment in technologies capable of detecting that type of particles (e.g. cloud radar) and at the same time to withstand the inclement conditions in Antarctic will be also crucial.

Appendix A

Variable noise threshold in MK12

The MK12 post-processing (version 0.101) analyses the variance of a given average spectrum to discriminate pure noise from signal that contains a real peak (see Equation 5 in MK12). The minimum threshold is:

$$V_T = 0.6/\sqrt{\Delta t}, \tag{A.1}$$

where V_T is the normalized standard deviation of a single average spectrum and Δt is the averaging time. When MRR collects less than the sampling rate, the noise of the signal increases, thus V_T also increase allowing some profiles not to be filtered correctly because the threshold is fixed. A new approach to avoid including noise data in the post-processing is to consider a variable threshold as function of the number of acquisition per minute. A new threshold for the normalized standard deviation was configured as:

$$V_T = 0.6/\sqrt{\Delta t \frac{n}{sr}}, \tag{A.2}$$

where n is the number of observation per minute, Δt is the averaging time equal to 60 seconds and sr is the mean sampling rate equal to 5.7 spectra per minute. This dynamic threshold allows to detect noise that increases its variability due to the decrease of number of observations.

Appendix B

Equations for saturation vapor pressure over water and ice

To derive the saturation vapor pressure over water e_{sw} and the saturation vapor pressure over ice e_{si} as function of the air temperature, we use the following equations from Goff (1957):

$$\begin{aligned} log(e_{sw}) = a_1 \cdot \left(1 - \frac{T_0}{T}\right) + a_2 \cdot log\left(\frac{T}{T_0}\right) \\ + a_3 \cdot 10^{-4} \cdot \left(1 - 10^{a_4 \cdot \left(\frac{T}{T_0} - 1\right)}\right) \\ + a_5 \cdot 10^{-3} \cdot (10^{a_6 \cdot \left(1 - \frac{T_0}{T}\right)} - 1) + a_7 \end{aligned} \tag{B.1}$$

and

$$log(e_{si}) = b1 \cdot \left(\frac{T_0}{T} - 1\right) + b_2 \cdot log\left(\frac{T_0}{T}\right) + b_3 \cdot \left(1 - \frac{T}{T_0}\right) + b_4 \tag{B.2}$$

where T is the air temperature in K, T_0 is the triple point of water (273.16 K), log is the logarithm with base 10 and the value for the constants are a_1 = 10.79574, a_2 = -5.02800, a_3 = 1.50475, a_4 = -8.2969, a_5 = 0.42873, a_6 = 4.76955, a_7 = -0.21386, b_1 = -9.096853, b_2 =-3.566506 and b_3 = 0.876812. b_4 = -0.21386. All the values of pressure are expressed in hPa.

Appendix C

Vertical profile of vertical velocity with respect to the altitude above sea level at DDU and PE

To better understand the differences in the Vertical profile of vertical velocity (VPV) at DDU and PE, we compared the VPV at both stations as a function of the height above sea level, instead of the height above ground level. This analysis allows to obtain a common region of altitude where the vertical velocities can be directly compared (see Fig. C.1). The left panel of the figure, shows the VPV (mean, median and quantiles) for surface precipitation and the right panel corresponds to virga. In the first case, although at DDU and PE similar values of W are observed at 3km of altitude, VPV at DDU increases rapidly going towards the surface, unlike at PE where a slight decrease is seen. These observed differences go in the same line as the results already discussed in the manuscript. Differences in the dominant microphysical processes (e.g. occurrence of riming and/or aggregation) at both stations play a significant role in the vertical profiles of mean Doppler velocity.

In the second case (virga), VPVs in the common region show very similar pattern for the both stations. An explanation for the similarities observed in the two regions is that the hydrometeors of virga profiles are mainly small size/pristine particles susceptible to be completely sublimated, thus the effect of the air density is similar at DDU and PE in the common region.

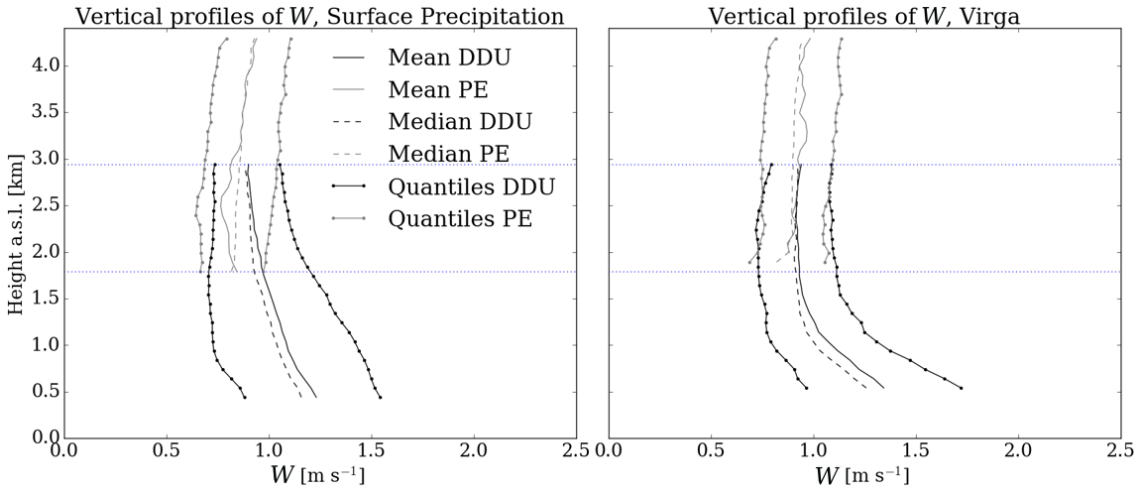

Figure C.1: Vertical profile of mean Doppler velocity at DDU (black lines) and PE (grey lines). Solid and dashed lines correspond to mean and median profiles, respectively. dotted-solid lines represent the 20 and 80% quantiles. The curves are equivalent to Figure 3.4 4e and f and Figure 3.5e and f, but height is expressed in altitude above mean sea level. Horizontal dotted-blue lines delimit the common height region of the profiles at both stations.

Appendix D

Temperature and Doppler moments

We have analyzed in more detail VPR as a function of temperature using radio sounding information at DDU and PE. Fig. D.1 displays the joint distribution for Ze and temperature, separated by surface precipitation (a) and virga (b). The results show a link between temperature and VPR for surface precipitation profiles at DDU. There is a positive correlation observed in the case of surface precipitation, that may be associated with the efficiency of the particle aggregation process with respect to the temperature. The spread observed for the lower values of Ze, may be linked with particles that are not involved in the aggregation process during surface precipitation.

In the case of virga, this relation is not observed, suggesting that ice particle growth is less significant during this type of events. In the case of PE, the few available radio soundings are not enough to observe a clear relation between both variables.

The analysis of VPV and VPS provides similar conclusion (see Fig. D.2 and Fig. D.3), but the correlation observed for surface precipitation cases is less evident, because these variables, especially spectral width, are affected by the turbulent katabatic winds at DDU.

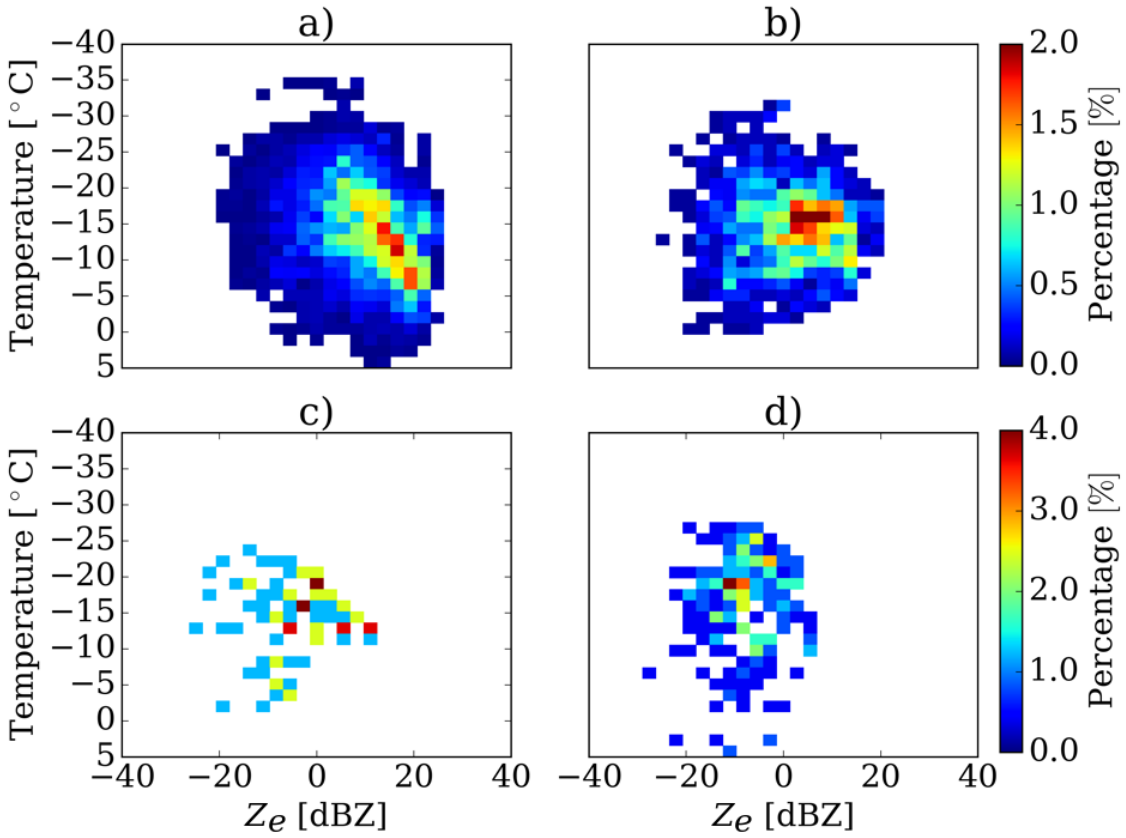

Figure D.1: Joint distribution for temperature and Ze using radio soundings separated by surface precipitation (a and c) and virga (b and d), for DDU (a and b) and PE (c and d).

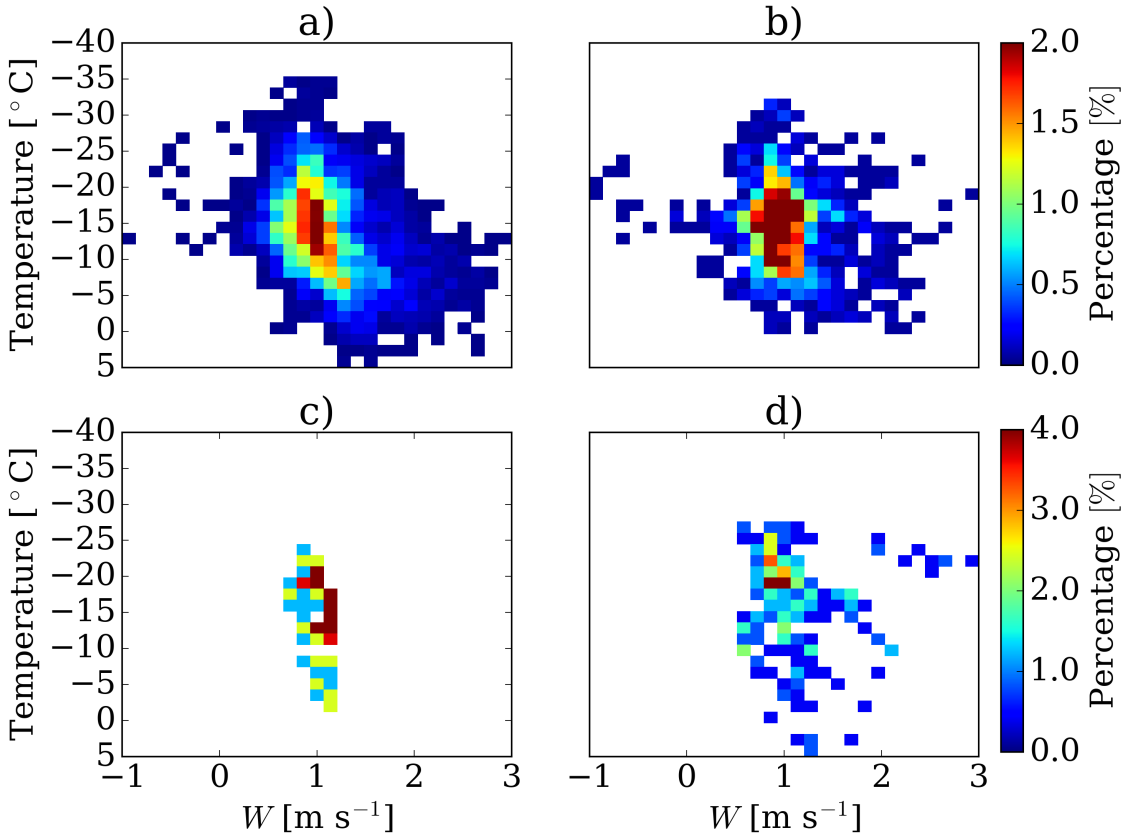

Figure D.2: Same as Fig. D.1, but for W.

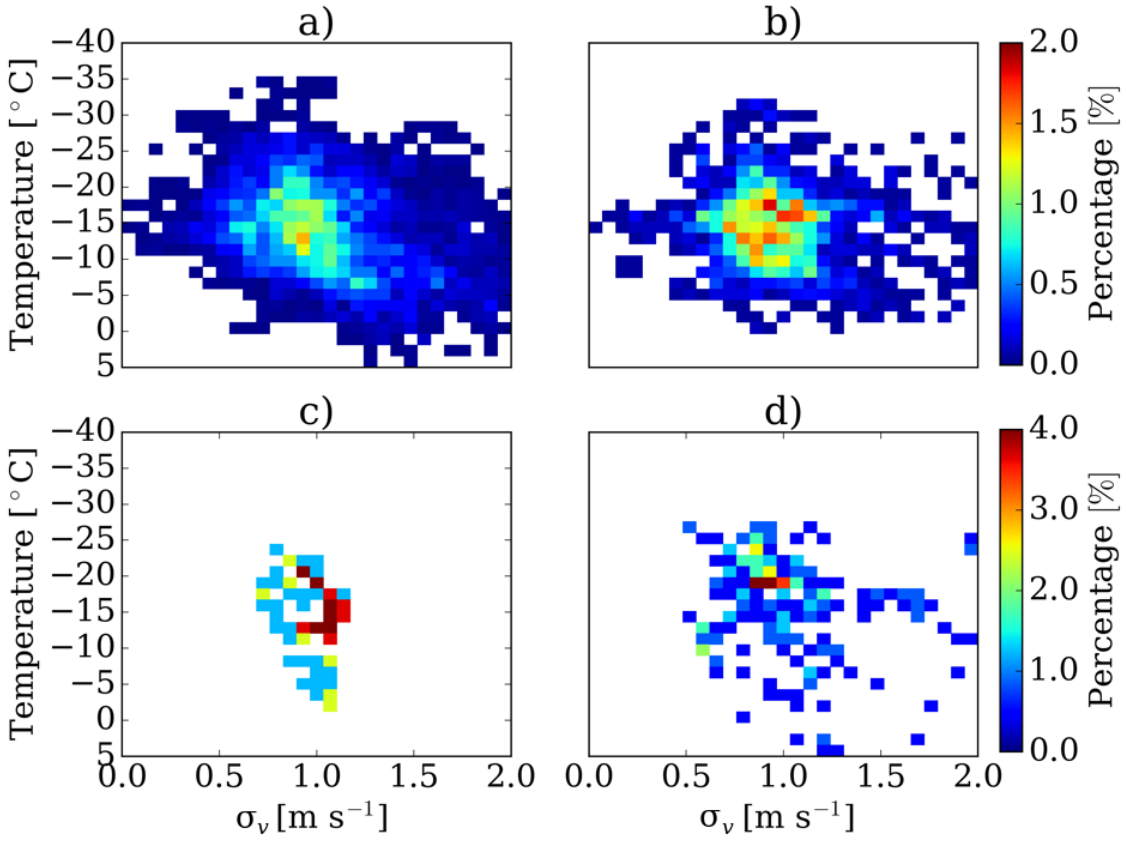

Figure D.3: Same as Fig. D.1, but for σ.

Appendix E

Profiles of Ze, W and σ_v at low temperatures at Col de Porte

The vertical profiles of radar reflectivity factor Z_e, vertical velocity W and spectral width σ_v for solid precipitation event at the Col de Porte station, in the French Alps, were analyzed for different threshold of temperatures (<-3, <-4 and <-5°C). Snowfall events are separated by surface precipitation and virga events. The patterns observed in these vertical profiles are similar to those in Figure 4.6, showing a dependency of Z_e and W on the near surface temperature threshold. This results, however, present a reduced number of observations (even no data for virga at temperature < -5°C) and are highly variables.

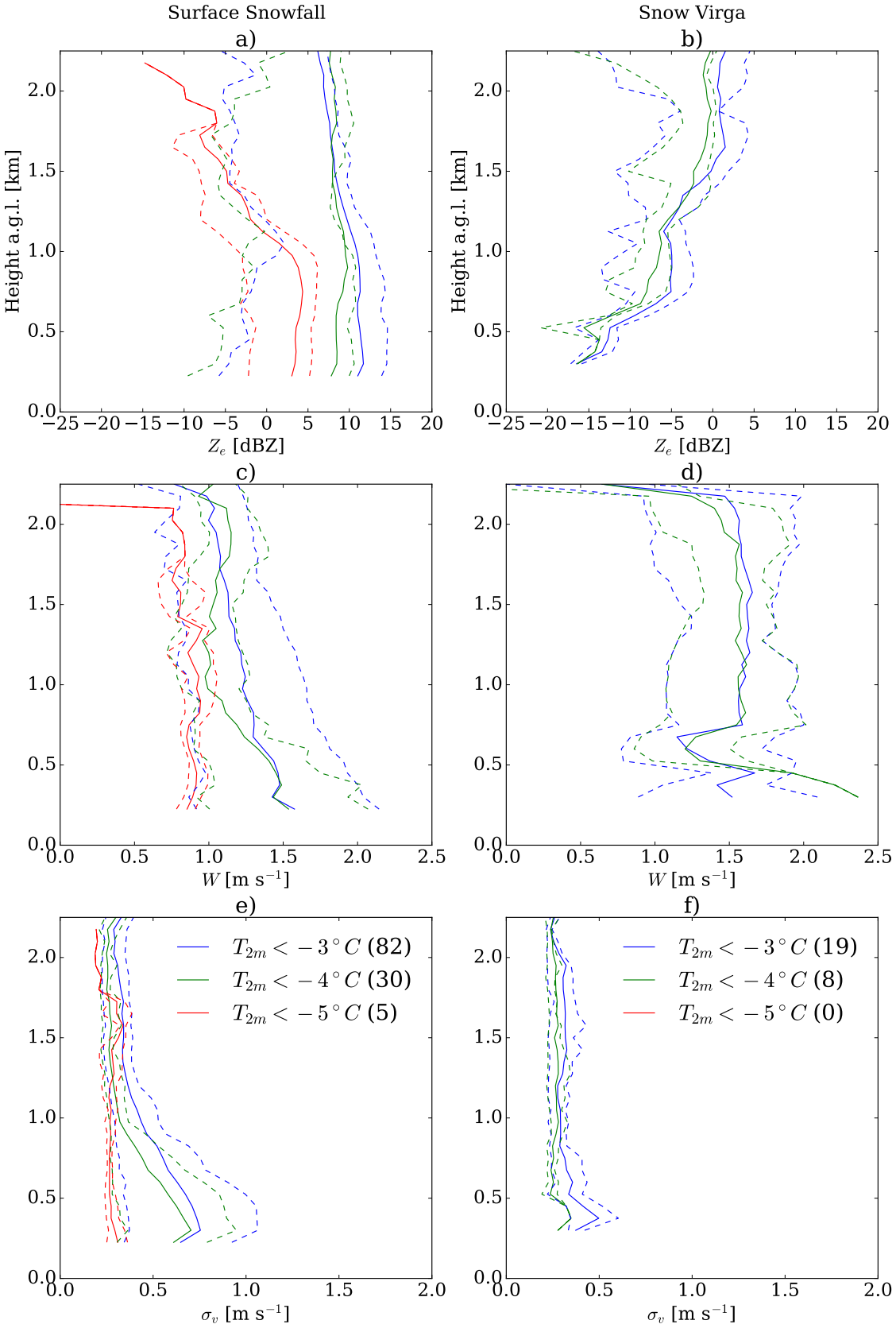

Figure E.1: Vertical profiles of Doppler moments using different thresholds on the temperature: <-3, <-4 and <-5°C. a and b correspond to Z_e, c and d to vertical velocity and e and f represent σ_v. In the legend, the number inside the parentheses indicates the total of snow or virga profiles for the given threshold.

Bibliography

Ackerman, T. P. and Stokes, G. M. (2003). The atmospheric radiation measurement program. *Physics Today*, 56(1):38–44. (Cited on page 38.)

Adler, R. F., Gu, G., and Huffman, G. J. (2012). Estimating climatological bias errors for the global precipitation climatology project (GPCP). *Journal of Applied Meteorology and Climatology*, 51(1):84–99. (Cited on pages 1 and 5.)

Amaya, C., García-Rubia, J.-M., Bouchard, P., and Nguyen, T. (2014). Experimental assessment of snow-induced attenuation on an Earth-space link operating at Ka-band. *Radio Science*, 49:933–944. (Cited on page 14.)

Andrews, T., Forster, P. M., and Gregory, J. M. (2009). A surface energy perspective on climate change. *Journal of Climate*, 22(10):2557–2570. (Cited on page 2.)

Andronache, C. (2014). *Remote sensing of clouds and precipitation*, volume 104. Springer Remote Sensing/Photogrammetry. (Cited on pages 11, 12, 13, and 14.)

Anghel, A., Member, S., Vasile, G., Cacoveanu, R., Ioana, C., and Ciochina, S. (2014). Short-Range Wideband FMCW Radar for Millimetric Displacement Measurements. *IEEE Transactions on Geoscience and Remote Sensing*, 52(9):5633–5642. (Cited on page 20.)

Arthur, D. and Vassilvitskii, S. (2007). k-means++: The Advantages of Careful Seeding. In *Proceedings of the Eighteenth Annual ACM-SIAM Symposium on Discrete Algorithms*, pages 1–11, Louisiana, USA. (Cited on page 50.)

Atlas, D. (1990). *Radar in meteorology*. American Meteorological Society, Boston, USA. (Cited on page 12.)

Atlas, D., Srivastava, R. C., and Sekhon, R. S. (1973). Doppler radar characteristics of precipitation at vertical incidence. (Cited on page 25.)

Baars, H., Seifert, P., Engelmann, R., and Wandinger, U. (2017). Target categorization of aerosol and clouds by continuous multiwavelength-polarization lidar measurements. *Atmospheric Measurement Techniques*, 10:3175–3201. (Cited on page 39.)

Baker, M. B. and Peter, T. (2008). Small-scale cloud processes and climate. *Nature*, 451(7176):299–300. (Cited on page 38.)

Balsamo, G., Albergel, C., Beljaars, A., Boussetta, S., Brun, E., Cloke, H., Dee, D., Dutra, E., Munõz-Sabater, J., Pappenberger, F., De Rosnay, P., Stockdale, T., and Vitart, F. (2015). ERA-Interim/Land: A global land surface reanalysis data set. *Hydrology and Earth System Sciences*, 19(1):389–407. (Cited on page 3.)

Bartolini, E., Claps, P., and D'Odorico, P. (2009). Interannual variability of winter precipitation in the European Alps: relations with the North Atlantic Oscillation. *Hydrology and Earth System Sciences*, 13:17–25. (Cited on page 86.)

Bechini, R., Baldini, L., and Chandrasekar, V. (2013). Polarimetric radar observations in the ice region of precipitating clouds at C-Band and X-Band radar frequencies. *Journal of Applied Meteorology and Climatology*, 52(5):1147–1169. (Cited on page 68.)

Behrangi, A., Christensen, M., Richardson, M., Lebsock, M., Stephens, G. L., Huffman, G. J., Bolvin, D. T., Adler, R. F., Gardner, A., Lambrigtsen, B. H., and Fetzer, E. (2016). Status of high-latitude precipitation estimates from observations and reanalyses. *Journal of Geophysical Research: Atmospheres*, 121:4468–4486. (Cited on pages 1 and 2.)

Behrangi, A., Lebsock, M., Wong, S., and Lambrigtsen, B. (2012). On the quantification of oceanic rainfall using spaceborne sensors. *Journal of Geophysical Research Atmospheres*, 117(20):1–14. (Cited on page 1.)

Behrangi, A., Tian, Y., Lambrigtsen, B. H., and Stephens, G. L. (2014). What does CloudSat reveal about global land precipitation detection by other spaceborne sensors? *Water Resources Research*, 50:4893–4905. (Cited on page 1.)

Beniston, M. and Stoffel, M. (2016). Rain-on-snow events, floods and climate change in the Alps: Events may increase with warming up to 4 °C and decrease thereafter. *Science of the Total Environment*, 571(May 1999):228–236. (Cited on page 2.)

Bodas-Salcedo, A., Hill, P. G., Furtado, K., Williams, K. D., Field, P. R., Manners, J. C., Hyder, P., and Kato, S. (2016). Large contribution of supercooled liquid clouds to the solar radiation budget of the Southern Ocean. *Journal of Climate*, 29(11):4213–4228. (Cited on page 6.)

Böhm, H. P. (1989). A General Equation for the Terminal Fall Speed of Solid Hydrometeors. (Cited on page 70.)

Bohne, A. R. (1982). Radar detection of turbulence on precipitation environments. *Journal of the Atmospheric Sciences*, 39:1819–1837. (Cited on page 95.)

Bony, S., Stevens, B., Frierson, D. M., Jakob, C., Kageyama, M., Pincus, R., Shepherd, T. G., Sherwood, S. C., Siebesma, A. P., Sobel, A. H., Watanabe, M., and Webb, M. J. (2015). Clouds, circulation and climate sensitivity. *Nature Geoscience*. (Cited on page 11.)

Braaten, D. A. (2000). Direct measurements of episodic snow accumulation on the Antarctic polar plateau. *Journal of Geophysical Research: Atmospheres*, 105(D8):10119–10128. (Cited on page 4.)

Bromwich, D. H., Otieno, F. O., Hines, K. M., Manning, K. W., and Shilo, E. (2013). Comprehensive evaluation of polar weather research and forecasting model performance in the antarctic. *Journal of Geophysical Research: Atmospheres*, 118(2):274–292. (Cited on page 6.)

Bromwich, D. H. and Stearns, C. R. (1993). *Antarctic Meteorology and Climatology: Studies Based on Automatic Weather Stations*, volume 61. American Geophysical Union, Washington DC, USA. (Cited on page 3.)

Bromwich, D. H., Steinhoff, D. F., Simmonds, I., Keay, K., and Fogt, R. L. (2011). Climatological aspects of cyclogenesis near Adélie Land Antarctica. *Tellus, Series A: Dynamic Meteorology and Oceanography*, 63A:921–938. (Cited on pages 4, 31, and 65.)

Bucholtz, A. (1995). Rayleigh-scattering, calculations for the terrestrial atmosphere. *Applied Optics*, 34(15):2765–2773. (Cited on page 41.)

Cairo, F., Donfrancesco, G. D., and Adriani, A. (1999). Comparison of various linear depolarization parameters measured by lidar. *Applied optics*, 38(21):4425–4432. (Cited on page 30.)

Cao, N., Zhu, C., Kai, Y., and Yan, P. (2013). A method of background noise reduction in lidar data. *Applied Physics B*, 113(1):115–123. (Cited on page 41.)

Cazenave, Q., Ceccaldi, M., Delanoë, J., Pelon, J., Groß, S., and Heymsfield, A. J. (2019). Evolution of DARDAR-CLOUD ice cloud retrievals: New parameters and impacts on the retrieved microphysical properties. *Atmospheric Measurement Techniques*, 12:2819–2835. (Cited on page 39.)

Ceccaldi, M., Delanoë, J., Hogan, R. J., Pounder, N. L., Protat, A., and Pelon, J. (2013). From CloudSat-CALIPSO to EarthCare: Evolution of the DARDAR cloud classification and its comparison to airborne radar-lidar observations. *Journal of Geophysical Research Atmospheres*, 118(14):7962–7981. (Cited on page 57.)

Cheng, Y., Cao, J., Hao, Q., Xiao, Y., Zhang, F., Xia, W., Zhang, K., and Yu, H. (2017). A novel de-noising method for improving the performance of full-waveform LiDAR using differential optical path. *Remote Sensing*, 9(11). (Cited on page 43.)

Clough, S. A. and Franks, R. A. (1991). The evaporation of frontal and other stratiform precipitation. *Quarterly Journal of the Royal Meteorological Society*, 117(501):1057–1080. (Cited on pages 67, 70, 72, 81, and 88.)

CS Inc. (2014). PWS100 Present Weather Sensor. Technical report. (Cited on pages 90 and 91.)

Del Guasta, M., Morandi, M., and Stefanutti, L. (1993). One year of cloud lidar data from Dumont d'Urville (Antarctica): 1. General overview of geometrical and optical properties. *Journal of Geophysical Research*, 98(D10):18575–18587. (Cited on page 39.)

Del Guasta, M., Vallar, E., Riviere, O., Castagnoli, F., Venturi, V., and Morandi, M. (2006). Use of polarimetric lidar for the study of oriented ice plates in clouds. *Applied Optics*, 45(20):4878–4887. (Cited on page 49.)

Delanoë, J. and Hogan, R. J. (2010). Combined CloudSat-CALIPSO-MODIS retrievals of the properties of ice clouds. *Journal of Geophysical Research: Atmospheres*, 115(D00H29):1–17. (Cited on pages 10, 39, and 57.)

Diaz, H. F., Eischeid, J. K., Duncan, C., and Bradley, R. S. (2003). Indicators , and Snow Cover for Selected High-Elevation and Continental Regions in the Last 50 Years. *Climatic Change*, 59:33–52. (Cited on page 2.)

Drewry, D. (1992). The response of large ice sheets to climatic change. *Philosophical Transactions of the Royal Society of London. Series B: Biological Sciences*, 338:235–242. (Cited on pages 2 and 3.)

Durán-Alarcón, C., Boudevillain, B., Genthon, C., Grazioli, J., Souverijns, N., Lipzig, N. P. M. V., Gorodetskaya, I. V., and Berne, A. (2019). The vertical structure of precipitation at two stations in East Antarctica derived from micro rain radars. *The Cryosphere*, 13:247–264. (Cited on pages 85, 89, 96, and 99.)

Dyurgerov, M. B. and Carter, C. L. (2006). Observational Evidence of Increases in Freshwater Inflow to the Arctic Ocean. *Arctic, Antarctic, and Alpine Research*, 36(1):117–122. (Cited on page 2.)

Evans, E., Stewart, R. E., Henson, W., and Saunders, K. (2011). On precipitation and virga over three locations during the 1999-2004 Canadian prairie drought. *Atmosphere - Ocean*, 49(4):366–379. (Cited on page 85.)

Fabry, F. and Szyrmer, W. (1999). Modeling of the Melting Layer. Part II: Electromagnetic. *Journal of the Atmospheric Sciences*, 56(20):3573–3592. (Cited on page 86.)

Fehlmann, M., Gascón, E., Rohrer, M., Schwarb, M., and Stoffel, M. (2018). Estimating the snowfall limit in alpine and pre-alpine valleys: A local evaluation of operational approaches. *Atmospheric Research*, 204(October 2017):136–148. (Cited on page 2.)

Frezzotti, M., Pourchet, M., Flora, O., Gandolfi, S., Gay, M., Urbini, S., Vincent, C., Becagli, S., Gragnani, R., Proposito, M., Severi, M., Traversi, R., Udisti, R., and Fily, M. (2004). New estimations of precipitation and surface sublimation in East Antarctica from snow accumulation measurements. *Climate Dynamics*, 23(7-8):803–813. (Cited on page 61.)

Frieler, K., Clark, P. U., He, F., Buizert, C., Reese, R., Ligtenberg, S. R. M., Van Den Broeke, M. R., Winkelmann, R., and Levermann, A. (2015). Consistent evidence of increasing Antarctic accumulation with warming. *Nature Climate Change*, 5(4):348–352. (Cited on page 61.)

Fuchs, T., Rapp, J., Rubel, F., and Rudolf, B. (2001). Correction of synoptic precipitation observations due to systematic measuring errors with special regard to precipitation phases. *Physics and Chemistry of the Earth, Part B: Hydrology, Oceans and Atmosphere*, 26(9):689–693. (Cited on page 2.)

Gangoiti, G., Cámara, E. S. D., Gómez-domenech, I., Alonso, L., Navazo, M., Iza, J., García, J. A., and Millán, M. M. (2015). Re-evaluation of moisture sources for the August 2002 extreme rainfall episode in central Europe : Evaporation from falling precipitation included in a mesoscale modeling system. *Journal of Hydrology*, 529(August 2002):696–710. (Cited on page 85.)

Garrett, T. J. and Yuter, S. E. (2014). Observed influence of riming, temperature, and turbulence on the fallspeed of solid precipitation. *Geophysical Research Letters*, 41(18):6515–6522. (Cited on page 71.)

Garrett, T. J., Yuter, S. E., Fallgatter, C., Shkurko, K., Rhodes, S. R., and Endries, J. L. (2015). Orientations and aspect ratios of falling snow. *Geophysical Research Letters*, 42(11):4617–4622. (Cited on page 71.)

Geerts, B. and Dejene, T. (2005). Regional and diurnal variability of the vertical structure of precipitation systems in Africa based on spaceborne radar data. *Journal of Climate*, 18(7):893–916. (Cited on page 85.)

Genthon, C., Berne, A., Grazioli, J., Durán-Alarcón, C., and Praz, C. (2018). Precipitation at Dumont d'Urville , Adélie Land , East Antarctica : the APRES3 field campaigns dataset. *Earth System Science Data*, 10:1605–1612. (Cited on pages 33 and 47.)

Genthon, C., Krinner, G., and Castebrunet, H. (2009). Antarctic precipitation and climate-change predictions: Horizontal resolution and margin vs plateau issues. *Annals of Glaciology*, 50(50):55–60. (Cited on page 4.)

Genthon, C., Krinner, G., and Sacchettini, M. (2003). Interannual Antarctic tropospheric circulation and precipitation variability. *Climate Dynamics*, 21(3-4):289–307. (Cited on pages 3 and 5.)

Germann, U., Galli, G., Boscacci, M., and Bolliger, M. (2006). Radar precipitation measurement in a mountainous region. *Quarterly Journal of the Royal Meteorological Society*, 132(618 A):1669–1692. (Cited on page 84.)

Giorgi, F., Coppola, E., and Raffaele, F. (2014). A consistent picture of the hydroclimatic response to global warming from multiple indices: Models and observations. *Journal of Geophysical Research: Atmospheres*, 119(1):1365–1382. (Cited on page 1.)

Giorgi, F., Raffaele, F., and Coppola, E. (2019). The response of precipitation characteristics to global warming from climate projections. *Earth System Dynamics*, 10:73–89. (Cited on pages 1 and 2.)

Gobbi, G. P. (1995). Lidar estimation of stratospheric aerosol properties: Surface, volume, and extinction to backscatter ratio. *Journal of Geophysical Research*, 100(D6):11219–11235. (Cited on pages 27 and 38.)

Goff, J. (1957). Saturation pressure of water on the new Kelvin scale. *Trans. Am. Soc. Heating Air-Cond. Eng.*, 63:347–357. (Cited on pages 64 and 109.)

Gong, W., Mao, F., and Song, S. (2011). Signal simplification and cloud detection with an improved Douglas-Peucker algorithm for single-channel lidar. *Meteorology and Atmospheric Physics*, 113:89–97. (Cited on pages 47, 58, and 104.)

Gooch, J. W. (2011). Mann-Whitney U Test. In *Encyclopedic Dictionary of Polymers*. (Cited on page 97.)

Goodison, B., Louie, P. Y. T., and Yang, D. (1998). WMO solid precipitation measurement intercomparison. Technical Report 67, World Meteorological Organization. (Cited on page 2.)

Gorodetskaya, I. V., Kneifel, S., Maahn, M., Thiery, W., Schween, J. H., Mangold, A., Crewell, S., and van Lipzig, N. P. (2015). Cloud and precipitation properties from ground-based remote-sensing instruments in East Antarctica. *Cryosphere*, 9(1):285–304. (Cited on pages 6, 7, 31, 33, 62, 67, 70, 71, 72, and 89.)

Gorodetskaya, I. V., van Lipzig, N. P., Van Den Broeke, M. R., Mangold, A., Boot, W., and Reijmer, C. H. (2013). Meteorological regimes and accumulation patterns at Utsteinen, Dronning Maud Land, East Antarctica: Analysis of two contrasting years. *Journal of Geophysical Research Atmospheres*, 118(4):1700–1715. (Cited on pages 31 and 70.)

Gossart, A., Souverijns, N., Gorodetskaya, I. V., Lhermitte, S., Lenaerts, J. T., Schween, J. H., Mangold, A., Laffineur, Q., and Van Lipzig, N. P. (2017). Blowing

snow detection from ground-based ceilometers: Application to East Antarctica. *Cryosphere*, 11(6):2755–2772. (Cited on page 31.)

Grazioli, J., Genthon, C., Boudevillain, B., Duran-Alarcon, C., Del Guasta, M., Madeleine, J.-B., and Berne, A. (2017a). Measurements of precipitation in Dumont d'Urville, Adélie Land, East Antarctica. *The Cryosphere*, 11(4):1797–1811. (Cited on pages 7, 24, 25, 31, 32, 33, 34, 62, 67, 68, 70, and 72.)

Grazioli, J., Madeleine, J.-B., Gallée, H., Forbes, R. M., Genthon, C., Krinner, G., and Berne, A. (2017b). Katabatic winds diminish precipitation contribution to the Antarctic ice mass balance. *Proceedings of the National Academy of Sciences*, page 201707633. (Cited on pages 31, 67, 70, 72, and 85.)

Hallikainen, M., Ulaby, F. T., and Abdelrazik, M. (1986). Dielectric properties of snow in the 3 to 37 GHz range. *IEEE Transactions on Antennas and Propagation*, AP-34(11):1329–1340. (Cited on page 14.)

Hantel, M. and Hirtl-Wielke, L.-M. (2007). Sensitivity of Alpine snow cover to European temperature. *International Journal of Climatology*, 27:1265–1275. (Cited on page 2.)

Hantel, M., Maurer, C., and Mayer, D. (2012). The snowline climate of the Alps 1961-2010. *Theoretical and Applied Climatology*, 110(4):517–537. (Cited on page 8.)

Hartmann, D. L., Ockert-Bell, M. E., and Michelsen, M. L. (1992). The effect of Cloud Type on the Earth's Energy Balance: Global Analysis. *American Meteorological Society*, 5:1281–1304. (Cited on page 11.)

Haynes, J. M., L'Ecuyer, T. S., Stephens, G. L., Miller, S. D., Mitrescu, C., Wood, N. B., and Tanelli, S. (2009). Rainfall retrieval over the ocean with spaceborne W-band radar. *Journal of Geophysical Research Atmospheres*, 114(8):1–18. (Cited on pages 5 and 97.)

Hélière, A., Lefebvre, A., Wehr, T., Bézy, J. L., and Durand, Y. (2007). The EarthCARE Mission: Mission concept and lidar instrument pre-development. *International Geoscience and Remote Sensing Symposium (IGARSS)*, pages 4975–4978. (Cited on page 6.)

Hélière, A., Wallace, K., Pereira Do Carmo, J., Lefebvre, A., Eisinger, M., and Wehr, T. (2016). Development status of the EarthCARE Mission and its atmospheric Lidar. In *Proc. SPIE, Earth Observing Systems XXI*, volume 9972, page 997215. (Cited on page 6.)

Heymsfield, A. J., Schmitt, C., and Bansemer, A. (2013). Ice Cloud Particle Size Distributions and Pressure-Dependent Terminal Velocities from In Situ Observations at Temperatures from 0° to -86°C. *Journal of the Atmospheric Sciences*, 70(12):4123–4154. (Cited on page 71.)

Heymsfield, A. J. and Westbrook, C. D. (2010). Advances in the Estimation of Ice Particle Fall Speeds Using Laboratory and Field Measurements. *Journal of the Atmospheric Sciences*, 67(8):2469–2482. (Cited on page 70.)

Hobbs, P. V., Chang, S., and Locatelli, J. D. (1974). The dimensions and aggregation of ice crystals in natural clouds. *Journal of Geophysical Research*, 79(15):2199–2206. (Cited on page 80.)

Hogan, R. J., Behera, M. D., O'Connor, E. J., and Illingworth, A. J. (2004). Estimate of the global distribution of stratiform supercooled liquid water clouds using the LITE lidar. *Geophysical Research Letters*, 31(L05106):1–4. (Cited on pages 27 and 39.)

Hosler, C. L. and Hallgren, R. E. (1960). THE AGGREGATION OF SMALL ICE CRYSTALS. *Discussions of the Faraday Society*, 30:200–207. (Cited on page 80.)

Houze, R. A. (2014). Chapter 3 - Cloud Microphysics. In *Cloud Dynamics*. (Cited on page 20.)

Hu, Y. (2007). Depolarization ratio-effective lidar ratio relation: Theoretical basis for space lidar cloud phase discrimination. *Geophysical Research Letters*, 34(11):6–9. (Cited on page 27.)

Hu, Y., Rodier, S., Xu, K. M., Sun, W., Huang, J., Lin, B., Zhai, P., and Josset, D. (2010). Occurrence, liquid water content, and fraction of supercooled water clouds from combined CALIOP/IIR/MODIS measurements. *Journal of Geophysical Research: Atmospheres*, 115(D00H34):1–13. (Cited on page 39.)

Hu, Y., Vaughan, M., Liu, Z., Lin, B., Yang, P., Flittner, D., Hunt, B., Kuehn, R., Huang, J., Wu, D., Rodier, S., Powell, K., Trepte, C., and Winker, D. (2007). The depolarization - attenuated backscatter relation: CALIPSO lidar measurements vs. theory. *Optics Express*, 15(9):5327. (Cited on page 27.)

IPCC (2007). Towards new scenarios for analysis of emissions, climate change, impacts, and response strategies. Technical report, Noordwijkerhout, The Netherlands. (Cited on page 1.)

IPCC (2013). *Climate change 2013 - The physical Science Basis*. Cambridge University Press, Cambridge, United Kingdom and New York, NY, USA. (Cited on pages 1, 2, 3, and 8.)

King, J. C., Anderson, P. S., Vaughan, D. G., Mann, G. W., Mobbs, S. D., and Vosper, S. B. (2004). Wind-borne redistribution of snow across an Antarctic ice rise. *Journal of Geophysical Research D: Atmospheres*, 109(11). (Cited on page 4.)

King, J. C., Gadian, A., Kirchgaessner, A., Kuipers Munneke, P., Lachlan-Cope, T. A., Orr, A., Reijmer, C., van den Broeke, M. R., van Wessem, J. M., and Weeks, M. (2015). Validation of the summertime surface energy budget of Larsen C Ice Shelf (Antarctica) as represented in three high-resolution atmospheric models. *Journal of Geophysical Research*, 120(4):1335–1347. (Cited on page 6.)

King, J. C. and Turner, J. (1997). *Antarctic Meteorology and Climatology*. Cambridge University Press, Cambridge, United Kingdom and New York. (Cited on page 3.)

Kneifel, S., Maahn, M., Peters, G., and Simmer, C. (2011). Observation of snowfall with a low-power FM-CW K-band radar (Micro Rain Radar). *Meteorology and Atmospheric Physics*, 113(1):75–87. (Cited on pages 25 and 26.)

Knowles, N., Dettinger, M. D., and Cayan, D. (2001). Trends in Snowfall Versus Rainfall for the Western United States, 1949-2001. *Energy*, 19(April 2007):4545–4559. (Cited on page 2.)

König-Langlo, G., King, J. C., and Pettré, P. (1998). Climatology of the three coastal Antarctic stations Dumont d'Urville, Neumayer, and Halley. *Journal of Geophysical Research: Atmospheres*, 103(D9):10935–10946. (Cited on page 31.)

Korokev, A., McFarquhar, G., Field, P. R., Franklin, C., Lawson, R. P., Wan, Z., Williams, E., Abel, S. J., Axisa, D., Borrmann, S., Crosier, J., Fugal, J., Kramer, M., Lohmann, U., Schlenczek, M., Schnaiter, M., and Wendisch, M. (2017). Chapter 5 Mixed-Phase Clouds : Progress and Challenges. In *AMS Monographs*, volume 58, pages 1–50. (Cited on page 39.)

Kovalev, V. a. and Eichinger, W. E. (2004). *Elastic Lidar: Theory, Practice, and Analysis Methods*. Wiley-Interscience, New Jersey. (Cited on pages 28, 29, 41, and 43.)

Krinner, G., Magand, O., Simmonds, I., Genthon, C., and Dufresne, J.-L. (2007). Simulated Antarctic precipitation and surface mass balance at the end of the twentieth and twenty-first centuries. *Climate Dynamics*, 28(2-3):215–230. (Cited on page 61.)

Lau, W. K., Wu, H. T., and Kim, K. M. (2013). A canonical response of precipitation characteristics to global warming from CMIP5 models. *Geophysical Research Letters*, 40(12):3163–3169. (Cited on page 1.)

Lawson, R. P. and Gettelman, A. (2014). Impact of Antarctic mixed-phase clouds on climate. *Proceedings of the National Academy of Sciences*, 111(51):18156–18161. (Cited on page 39.)

Lemonnier, F., Madeleine, J.-b., Claud, C., Genthon, C., Durán-Alarcón, C., Palerme, C., Berne, A., Souverijns, N., Lipzig, N. V., Gorodetskaya, I. V., Ecuyer, T. L., and Wood, N. (2019). Evaluation of CloudSat snowfall rate profiles by a comparison with in situ micro-rain radar observations in East Antarctica. *The Cryosphere*, 13:943–954. (Cited on pages 61 and 106.)

Lewis, J. R., Campbell, J. R., Welton, E. J., Stewart, S. A., and Haftings, P. C. (2016). Overview of MPLNET version 3 cloud detection. *Journal of Atmospheric and Oceanic Technology*, 33(10):2113–2134. (Cited on page 38.)

Ligtenberg, S. R. M., van de Berg, W. J., van den Broeke, M. R., Rae, J. G. L., and van Meijgaard, E. (2013). Future surface mass balance of the Antarctic ice sheet and its influence on sea level change, simulated by a regional atmospheric climate model. *Climate Dynamics*, 41(3-4):867–884. (Cited on page 61.)

Listowski, C., Delanoë, J., Kirchgaessner, A., Lachlan-Cope, T. A., and King, J. (2019). Antarctic clouds, supercooled liquid water and mixed phase, investigated

with DARDAR: Geographical and seasonal variations. *Atmospheric Chemistry and Physics*, 19:6771–6808. (Cited on pages 5, 6, 39, and 57.)

Listowski, C. and Lachlan-Cope, T. A. (2017). The microphysics of clouds over the Antarctic Peninsula - Part 2: Modelling aspects within Polar WRF. *Atmospheric Chemistry and Physics*, 17(17):10195–10221. (Cited on page 6.)

Liu, Y., Geerts, B., Miller, M., Daum, P., and McGraw, R. (2008). Threshold radar reflectivity for drizzling clouds. *Geophysical Research Letters*. (Cited on page 20.)

Liu, Z., Li, Z., Liu, B., and Li, R. (2009). Analysis of saturation signal correction of the troposphere lidar. *Chinese Optics Letters*, 7(11):1051–1054. (Cited on page 43.)

Lohmann, U., Lüönd, F., and Mahrt, F. (2016). *An introduction to clouds: From the microscale to climate*. (Cited on pages 12, 13, 20, and 38.)

Lubin, D., Bromwich, D. H., Vogelmann, A. M., Verlinde, J., and Russell, L. M. (2017). ARM West Antarctic Radiation Experiment (AWARE) Field Campaign Report. Technical Report September. (Cited on page 62.)

Maahn, M., Burgard, C., Crewell, S., Gorodetskaya, I. V., Kneifel, S., Lhermitte, S., Van Tricht, K., and van Lipzig, N. P. (2014). How does the spaceborne radar blind zone affect derived surface snowfall statistics in polar regions? *Journal of Geophysical Research*, 119(22):13604–13620. (Cited on pages 5, 6, 62, 67, 72, 81, 84, and 88.)

Maahn, M. and Kollias, P. (2012). Improved Micro Rain Radar snow measurements using Doppler spectra post-processing. *Atmospheric Measurement Techniques*, 5(11):2661–2673. (Cited on pages 26, 34, 63, and 71.)

Mace, G. G., Heymsfield, A. J., and Poellot, M. R. (2002). On retrieving the microphysical properties of cirrus clouds using the moments of the millimeter-wavelength Doppler spectrum. *Journal of Geophysical Research*, 107(D24):4815. (Cited on page 22.)

Mace, G. G. and Zhang, Q. (2014). The CloudSat radar-lidar geometrical profile product (RL-GeoProf): Updates, improvements, and selected results. *Journal of Geophysical Research: Atmospheres*, 119:9441–9462. (Cited on pages 6 and 7.)

Marchand, R., Mace, G. G., Ackerman, T. P., and Stephens, G. (2008). Hydrometeor detection using Cloudsat - An earth-orbiting 94-GHz cloud radar. *Journal of Atmospheric and Oceanic Technology*, 25(4):519–533. (Cited on page 6.)

Marshall, G. J. (2009). On the annual and semi-annual cycles of precipitation across Antarctica. *International Journal of Climatology*, 29:2298–2308. (Cited on page 79.)

Marty, C. (2008). Regime shift of snow days in Switzerland. *Geophysical Research Letters*, 35(12):1–5. (Cited on page 2.)

Matrosov, S. Y. (1992). Radar reflectivity in Snowfall. *IEEE Transactions on Geoscience and Remote Sensing*, 30(3):454–461. (Cited on page 24.)

Matrosov, S. Y., Campbell, C., Kingsmill, D., and Sukovich, E. (2009). Assessing snowfall rates from X-Band radar reflectivity measurements. *Journal of Atmospheric and Oceanic Technology*, 26(11):2324–2339. (Cited on pages 24 and 25.)

Mengel, M., Levermann, A., Frieler, K., Robinson, A., Marzeion, B., and Winkelmann, R. (2016). Future sea level rise constrained by observations and long-term commitment. *Proceedings of the National Academy of Sciences*, 113(10):2597–2602. (Cited on page 61.)

Mioche, G., Jourdan, O., Ceccaldi, M., and Delanoë, J. (2015). Variability of mixed-phase clouds in the Arctic with a focus on the Svalbard region: a study based on spaceborne active remote sensing. *Atmospheric Chemistry and Physics*, 15:2445–2461. (Cited on page 39.)

Mioche, G., Jourdan, O., Delanoë, J., Gourbeyre, C., Febvre, G., Dupuy, R., Monier, M., Szczap, F., Schwarzenboeck, A., and Gayet, J. F. (2017). Vertical distribution of microphysical properties of Arctic springtime low-level mixed-phase clouds over the Greenland and Norwegian seas. *Atmospheric Chemistry and Physics*, 17:12845–12869. (Cited on page 39.)

Mitchell, D. L. and Heymsfield, A. J. (2005). Refinements in the Treatment of Ice Particle Terminal Velocities, Highlighting Aggregates. *Journal of the Atmospheric Sciences*, 62:1637–1644. (Cited on page 70.)

Moisseev, D. N., Lautaportti, S., Tyynela, J., and Lim, S. (2015). Dual-polarization radar signatures in snowstorms: Role of snowflake aggregation. *Journal of Geophysical Research Atmospheres*, 120(12):1739–1758. (Cited on page 68.)

Moisseev, D. N., Saltikoff, E., and Leskinen, M. (2009). Dual-Polarization Weather Radar Observations of Snow Growth Processes. pages 2–6. (Cited on page 68.)

Molthan, A. L., Petersen, W. A., Nesbitt, S. W., and Hudak, D. (2010). Evaluating the Snow Crystal Size Distribution and Density Assumptions within a Single-Moment Microphysics Scheme. *Monthly Weather Review*, 138(11):4254–4267. (Cited on pages 70 and 71.)

Morin, S., Lejeune, Y., Panel, J.-M., Lesaffre, B., Pezard, L., Carmagnola, C., Dumont, M., Condom, T., Biron, R., Laurent, J.-P., Picard, G., Voisin, D., Arnaud, L., Genthon, C., Piard, L., Libois, Q., Carrier, P., and Gottardi, F. (2013). Long-Term (Climatological) to Short-Term (Intensive Campaigns) Field Investigations of Meteorological and Snow Conditions at the Experimental Site Col de Porte. *International Snow Science Workshop Grenoble – Chamonix Mont-Blanc - October 07-11, 2013*, pages 1402–1405. (Cited on pages 32 and 85.)

Mygard, T., Valkonen, T., and Vihma, T. (2013). Antarctic Low-Tropospheric Humidity Inversions: 10-Yr Climatology. *American Meteorological Society*, 26:5205–5219. (Cited on page 80.)

Nastrom, G. D. (1997). Doppler radar spectral width broadening due to beamwidth and wind shear. *Annales Geophysicae*, 15(6):786–796. (Cited on page 71.)

Nayak, M., Witkowski, M., Vane, D., Livermore, T., Rokey, M., Barthuli, M., Gravseth, I. J., Pieper, B., Rodzinak, A., Silva, S., and Woznick, P. (2012). CloudSat anomaly recovery and operational lessons learned. *SpaceOps 2012 Conference*. (Cited on page 7.)

Nitu, R., Roulet, Y., Wolff, M., Earle, M., Reverdin, A., Smith, C., Kochendorfer, J., Morin, S., Rasmussen, R., Wong, K., Alastrué, J., Arnold, L., Baker, B., Buisan, S., Collado, J. L., Colli, M., Collins, B., Gaydos, A., Hannula, H.-R., Hoover, J., Joe, P., Kontu, A., Laine, T., Lanza, L., Lanzinger, E., Lee, G. W., Lejeune, Y., Leppänen, L., Mekis, E., Panel, J., Poikonen, A., Ryu, S., Sabatini, F., Theriault, J., Yang, D., Genthon, C., van den Heuvel, F., Hirasawa, N., Konishi, H., Nishimura, K., and Senese, A. (2018). WMO Solid Precipitation Intercomparison Experiment (SPICE) (2012-2015). (131):1429. (Cited on page 9.)

Palerme, C., Claud, C., Dufour, A., Genthon, C., Wood, N. B., and L'Ecuyer, T. S. (2017a). Evaluation of Antarctic snowfall in global meteorological reanalyses. *Atmospheric Research*, 190:104–112. (Cited on pages 3 and 5.)

Palerme, C., Genthon, C., Claud, C., Kay, J. E., Wood, N. B., and L'Ecuyer, T. S. (2017b). Evaluation of current and projected Antarctic precipitation in CMIP5 models. *Climate Dynamics*, 48(1-2):225–239. (Cited on page 61.)

Palerme, C., Kay, J. E., Genthon, C., L'Ecuyer, T. S., Wood, N. B., and Claud, C. (2014). How much snow falls on the Antarctic ice sheet? *Cryosphere*, 8(4):1577–1587. (Cited on pages 5, 31, and 62.)

Palm, S. P., Kayetha, V., and Yang, Y. (2018a). Toward a Satellite-Derived Climatology of Blowing Snow Over Antarctica. *Journal of Geophysical Research: Atmospheres*, 123:10301–10313. (Cited on page 39.)

Palm, S. P., Yang, Y., Kayetha, V., and Nicolas, J. P. (2018b). Insight into the thermodynamic structure of blowing-snow layers in Antarctica from dropsonde and CALIPSO measurements. *Journal of Applied Meteorology and Climatology*, 57:2733–2748. (Cited on page 39.)

Pappalardo, G., Amodeo, A., Apituley, A., Comeron, A., Freudenthaler, V., Linné, H., Ansmann, A., Bösenberg, J., D'Amico, G., Mattis, I., Mona, L., Wandinger, U., Amiridis, V., Alados-Arboledas, L., Nicolae, D., and Wiegner, M. (2014). EARLINET: Towards an advanced sustainable European aerosol lidar network. *Atmospheric Measurement Techniques*, 7:2389–2409. (Cited on page 38.)

Parish, T. R., Pettré, P., and Wendler, G. (1993). The influence of large-scale forcing on the katabatic wind regime at Adélie Land, Antarctica. *Meteorology and Atmospheric Physics*, 51(3-4):165–176. (Cited on page 72.)

Paul, F., Kääb, A., and Haeberli, W. (2007). Recent glacier changes in the Alps observed by satellite: Consequences for future monitoring strategies. *Global and Planetary Change*, 56(1-2):111–122. (Cited on page 8.)

Peters, G., Fischer, B., and Andersson, T. (2002). Rain observations with a vertically looking Micro Rain Radar (MRR). *Boreal Environment Research*, 7(4):353–362. (Cited on page 25.)

Peters, G., Fischer, B., Münster, H., Clemens, M., and Wagner, A. (2005). Profiles of Raindrop Size Distributions as Retrieved by Microrain Radars. *Journal of Applied Meteorology*, 44(12):1930–1949. (Cited on pages 25 and 33.)

Pfitzenmaier, L., Unal, C. M. H., Dufournet, Y., and Russchenberg, H. W. J. (2018). Observing ice particle growth along fall streaks in mixed-phase clouds using spectral polarimetric radar data. *Atmos. Chem. Phys*, 185194(2016):7843–7862. (Cited on page 68.)

Pitts, M. C., Poole, L. R., and Gonzalez, R. (2018). Polar stratospheric cloud climatology based on CALIPSO spaceborne lidar measurements from 2006 to 2017. *Atmospheric Chemistry and Physics*, 18:10881–10913. (Cited on pages 27 and 38.)

Podgórski, J., Pętlicki, M., and Kinnard, C. (2018). Revealing recent calving activity of a tidewater glacier with terrestrial LiDAR reflection intensity. *Cold Regions Science and Technology*, 151:288–301. (Cited on page 39.)

Pope, A., Willis, I. C., Rees, W. G., Arnold, N. S., and Pálsson, F. (2013). Combining airborne lidar and Landsat ETM+ data with photoclinometry to produce a digital elevation model for Langjökull, Iceland. *International Journal of Remote Sensing*, 34(4):1005–1025. (Cited on page 39.)

Powell, K. A., Hostetler, C. A., Liu, Z., Vaughan, M. A., Kuehn, R. E., Hunt, W. H., Lee, K. P., Trepte, C. R., Rogers, R. R., Young, S. A., and Winker, D. M. (2009). Calipso lidar calibration algorithms. Part I: Nighttime 532-nm parallel channel and 532-nm perpendicular channel. *Journal of Atmospheric and Oceanic Technology*, 26(10):2015–2033. (Cited on pages 41 and 46.)

Probert-Jones, J. (1962). The radar equation in meteorology. (June). (Cited on page 17.)

Raghavan, S. (2003). *Radar Meteorology*. Springer Science. (Cited on pages 17 and 23.)

Rakovec, J. (1997). Vertical Radar Reflectivity Profiles in Slovenia. *Theoretical and Applied Climatology*, 47:35–47. (Cited on page 85.)

Rauber, R. M. and Nesbitt, S. W. (2014). *Radar Meteorology*. Wiley Blackwell, UK. (Cited on pages 15, 20, 21, and 23.)

Ravanel, L., Deline, P., Lambiel, C., and Vincent, C. (2013). Instability of a High Alpine Rock Ridge: The Lower Arête Des Cosmiques, Mont Blanc Massif, France. *Geografiska Annaler, Series A: Physical Geography*, 95(1):51–66. (Cited on page 7.)

Riahi, K., Rao, S., Krey, V., Cho, C., Chirkov, V., Fischer, G., Kindermann, G., Nakicenovic, N., and Rafaj, P. (2011). RCP 8.5-A scenario of comparatively high greenhouse gas emissions. *Climatic Change*, 109(1):33–57. (Cited on page 1.)

Sadiku, M. N. O. (1985). Refractive index of snow at microwave frequencies. *Appl. Opt.*, 24(4):572–575. (Cited on page 68.)

Sassen, K. (1977). Ice crystal habit discrimination with the optical backscatter depolarization technique.pdf. *Journal of Applied Meteorology*, 16:425–431. (Cited on page 6.)

Sassen, K. (1991). for Cloud Research : A Review. *American Meteorological Society*, 72(12):1848–1866. (Cited on pages 27 and 39.)

Sassen, K. (2003). Polarization in lidar: a review. *Proceedings of SPIE*, 5158:151–160. (Cited on page 30.)

Sassen, K., Wang, Z., and Liu, D. (2009). Global distribution of cirrus clouds from CloudSat/cloud-aerosol lidar and infrared pathfinder satellite observations (CALIPSO) measurements. *Journal of Geophysical Research Atmospheres*, 114(8):1–12. (Cited on page 7.)

Schär, C., Davies, T. D., Frei, C., Wanner, H., Widmann, M., Wild, M., and Davies, H. C. (1998). Current Alpine Climate. In Cebon, P., Dahinder, U., Davies, H. C., Imboden, D., and Jaeger, C. C., editors, *Views from the Alps: Regional Perspectives on Climate Change*, number 2, pages 21–170. The MIT press, Cambridge, Massachusetts, USA. (Cited on pages 7 and 8.)

Scherrer, S. C., Appenzeller, C., and Laternser, M. (2004). Trends in Swiss Alpine snow days: The role of local- and large-scale climate variability. *Geophysical Research Letters*, 31(13). (Cited on page 2.)

Schillinger, M., Morancais, D., Fabre, F., and Culoma, A. J. (2003). ALADIN: the lidar instrument for the AEOLUS mission. In *Proc. SPIE, Sensors, Systems, and Next-Generation Satellites VI*, volume 4881, page 40. (Cited on page 6.)

Schlosser, E. (1999). Effects of seasonal variability of accutnulation on yearly mean d180 values in Antarctic snow. *Journal of Glaciology*, 45(151):463–468. (Cited on page 79.)

Schneebeli, M., Dawes, N., Lehning, M., and Berne, A. (2013). High-resolution vertical profiles of X-band polarimetric radar observables during snowfall in the Swiss Alps. *Journal of Applied Meteorology and Climatology*, 52(2):378–394. (Cited on page 68.)

Serquet, G., Marty, C., Dulex, J. P., and Rebetez, M. (2011). Seasonal trends and temperature dependence of the snowfall/precipitation- day ratio in Switzerland. *Geophysical Research Letters*, 38(7):14–18. (Cited on page 2.)

She, C.-Y. (2007). Spectral structure of laser light scattering revisited: bandwidths of nonresonant scattering lidars. *Applied Optics*, 40(27):4875. (Cited on page 29.)

Smith, R. B., Jiang, Q., Fearon, M. G., Tabary, P., Dorninger, M., Doyle, J. D., and Benoit, R. (2003). Orographic precipitation and air mass transformation: An Alpine example. *Quarterly Journal of the Royal Meteorological Society*, 129(588 PART B):433–454. (Cited on pages 85 and 88.)

Snels, M., Cairo, F., Colao, F., and Di Donfrancesco, G. (2009). Calibration method for depolarization lidar measurements. *International Journal of Remote Sensing*, 30(21):5725–5736. (Cited on page 30.)

Snow, K., Seed, A., and Takacs, G. (2012). Determining the vertical profile of reflectivity using radar observations at long range. *IAHS-AISH Publication*, 351:69–74. (Cited on page 85.)

Solomon, S., Ivy, D. J., Kinnison, D., Mills, M. J., Neely III, R. R., and Schmidt, A. (2016). Emergence of healing in the Antarctic ozone layer. *Science*, 353(6296):269–274. (Cited on page 27.)

Souverijns, N., Gossart, A., Gorodetskaya, I. V., Lhermitte, S., Mangold, A., Laffineur, Q., Delcloo, A., and van Lipzig, N. P. (2018a). How does the ice sheet surface mass balance relate to snowfall? Insights from a ground-based precipitation radar in East Antarctica. *The Cryosphere*, 12:1987–2003. (Cited on pages 31 and 62.)

Souverijns, N., Gossart, A., Lhermitte, S., Gorodetskaya, I. V., Grazioli, J., Berne, A., Durán-Alarcón, C., Boudevillain, B., Genthon, C., Scarchilli, C., and van Lipzig, N. P. (2018b). Evaluation of the CloudSat surface snowfall product over Antarctica using ground-based precipitation radars. *The Cryosphere*, 12:3775–3789. (Cited on pages 7, 33, 62, and 106.)

Souverijns, N., Gossart, A., Lhermitte, S., Gorodetskaya, I. V., Kneifel, S., Maahn, M., Bliven, F. L., and van Lipzig, N. P. (2017). Estimating radar reflectivity - Snowfall rate relationships and their uncertainties over Antarctica by combining disdrometer and radar observations. *Atmospheric Research*, 196:211–223. (Cited on pages 24, 25, 31, 33, 67, 68, 71, and 89.)

SPICE (2019). Col de Porte Information. https://ral.ucar.edu/projects/SPICE/sites/col_de_porte/?u11o1cm6kvvjc4lp2 c1ahpk641. Last access: 30/07/2019. (Cited on page 33.)

Steger, C., Kotlarski, S., Jonas, T., and Schär, C. (2013). Alpine snow cover in a changing climate: A regional climate model perspective. *Climate Dynamics*, 41(3-4):735–754. (Cited on page 84.)

Stephens, G. L. and Ellis, T. D. (2008). Controls of Global-Mean Precipitation Increases in Global Warming. *American Meteorological Society*, 21:6141–6155. (Cited on page 1.)

Stephens, G. L., L'Ecuyer, T. S., Forbes, R., Gettlemen, A., Golaz, J. C., Bodas-Salcedo, A., Suzuki, K., Gabriel, P., and Haynes, J. (2010). Dreary state of precipitation in global models. *Journal of Geophysical Research Atmospheres*, 115(24):1–14. (Cited on page 1.)

Stephens, G. L., Li, J., Wild, M., Clayson, C. A., Loeb, N., Kato, S., L'Ecuyer, T. S., Stackhouse, P. W., Lebsock, M., and Andrews, T. (2012). An update on Earth's energy balance in light of the latest global observations. *Nature Geoscience*, 5(10):691–696. (Cited on page 2.)

Stephens, G. L., Vane, D. G., Boain, R. J., Mace, G. G., Sassen, K., Wang, Z., Illingworth, A. J., O'Connor, E. J., Rossow, W. B., Durden, S. L., Miller, S. D., Austin, R. T., Benedetti, A., and Mitrescu, C. (2002). The cloudsat mission and the A-Train: A new dimension of space-based observations of clouds and precipitation. *Bulletin of the American Meteorological Society*, 83(12):1771–1790. (Cited on pages 6 and 57.)

Stewart, R. E., Marwitz, J. D., and Pace, J. C. (1984). Characteristic through the Melting Layer of Stratiform Clouds. 41(22):3227–3237. (Cited on page 95.)

Stiles, W. and Ulaby, F. (1986). Dielectric Properties of Snow. *The Avalanche Book*, pages 49–71. (Cited on page 14.)

Surussavadee, C. and Staelin, D. H. (2011). Evaporation correction methods for microwave retrievals of surface precipitation rate. *IEEE Transactions on Geoscience and Remote Sensing*, 49(12 PART 1):4763–4770. (Cited on pages 84, 85, and 88.)

Tang, M. S., Chenoli, S. N., Samah, A. A., and Hai, O. S. (2018). An assessment of historical Antarctic precipitation and temperature trend using CMIP5 models and reanalysis datasets. *Polar Science*, 15(August 2017):1–12. (Cited on pages 5, 61, and 106.)

Tapiador, F. J. (2017). *Measuring Precipitation From Space*. Elsevier Inc. (Cited on page 5.)

Telling, J. W., Glennie, C., Fountain, A. G., and Finnegan, D. C. (2017). Analyzing glacier surface motion using LiDAR data. *Remote Sensing*, 9(3):9–12. (Cited on page 39.)

Thiery, W., Gorodetskaya, I. V., Bintanja, R., van Lipzig, N. P., Van Den Broeke, M. R., Reijmer, C. H., and Kuipers Munneke, P. (2012). Surface and snowdrift sublimation at Princess Elisabeth station, East Antarctica. *Cryosphere*, 6(4):841–857. (Cited on page 70.)

Tiuri, M., Sihvola, A., Nyfors, E., and Hallikaiken, M. (1984). The complex dielectric constant of snow at microwave frequencies. *IEEE Journal of Oceanic Engineering*, 9(5):377–382. (Cited on page 68.)

Trenberth, K. E., Dai Aiguo, Rasmussen, R. M., and Parsons David B. (2003). The Changing Character of Precipitation. *Bulletin of the American Meteorological Society*, 84(9):1205–1218. (Cited on page 1.)

Trenberth, K. E., Smith, L., Qian, T., Dai, A., and Fasullo, J. (2007). Estimates of the Global Water Budget and Its Annual Cycle Using Observational and Model Data. *Journal of Hydrometeorology*, 8(4):758–769. (Cited on pages 1 and 2.)

Turner, J., Leonard, S., Lachlan-Cope, T. A., and Marshall, G. J. (1998). Understanding Antarctic Peninsula precipitation distribution and variability using a

numerical weather prediction model. *Annals of Glaciology*, 27:591–596. (Cited on page 3.)

Valkenburg, M. E. V. and Middleton, W. M. (2001). *Reference Data for Engineers: Radio, Electronics, Computers and Communications*. (Cited on page 13.)

Van den Broeke, M. R., Reijmer, C. H., and Van de Wal, R. S. W. (2004). A study of the surface mass balance in Dronning Maud Land , Antarctica , using automatic weather station S. *Journal of Glaciology*, 50(171):565–582. (Cited on page 61.)

van Diedenhoven, B. (2017). Remote Sensing of Crystal Shapes in Ice Clouds. In *Light Scattering, Radiative Transfer and Remote Sensing*, pages 197–250. (Cited on page 49.)

van Lipzig, N. P., van Meijgaard, E., and Oerlemans, J. (2002). The spatial and temporal variability of the surface mass balance in Antarctica: results from a regional atmospheric climate model. *International Journal of Climatology*, 22(10):1197–1217. (Cited on page 79.)

van Wessem, J. M., Reijmer, C. H., Morlighem, M., Mouginot, J., Rignot, E., Medley, B., Joughin, I., Wouters, B., Depoorter, M. A., Bamber, J. L., Lenaerts, J. T., Van De Berg, W. J., Van Den Broeke, M. R., and Van Meijgaard, E. (2014). Improved representation of East Antarctic surface mass balance in a regional atmospheric climate model. *Journal of Glaciology*, 60(222):761–770. (Cited on pages 2 and 61.)

van Wessem, J. M., van de Berg, W. J., Noël, B. P. Y., van Meijgaard, E., Birnbaum, G., Jakobs, C. L., Krüger, K., Lenaerts, J. T. M., Lhermitte, S., Ligtenberg, S. R. M., Medley, B., Reijmer, C. H., van Tricht, K., Trusel, L. D., van Ulft, L. H., Wouters, B., Wuite, J., and van den Broeke, M. R. (2018). Modelling the climate and surface mass balance of polar ice sheets using RACMO2, part 2: Antarctica (1979-2016). *The Cryosphere*, 12:1479–1498. (Cited on pages 2 and 61.)

Vaughan, D. G., Bamber, J. L., Giovinetto, M., Russell, J., and Cooper, A. P. R. (1999). Reassessment of net surface mass balance in Antarctica. *Journal of Climate*, 12(4):933–946. (Cited on page 4.)

Vignal, B., Galli, G., Joss, J., and Germann, U. (2000). Three Methods to Determine Profiles of Reflectivity from Volumetric Radar Data to Correct Precipitation

Estimates. *Journal of Applied Meteorology*, 39(10):1715–1726. (Cited on page 85.)

Wandinger, U. (2005). Introduction to Lidar. In Weitkamp, C., editor, *Lidar*, page 18. Springer, New York, NY, springer s edition. (Cited on pages 11, 27, and 28.)

Wang, S., Zhang, M., Pepin, N. C., Li, Z., Sun, M., Huang, X., and Wang, Q. (2014). Recent changes in freezing level heights in High Asia and their impact on glacier changes. *Journal of Geophysical Research: Atmospheres*, 119:1753–1765. (Cited on page 2.)

Wang, Y., You, Y., and Mark, K. (2018). Global Virga Precipitation Distribution Derived From Three Spaceborne Radars and Its Contribution to the False Radiometer Precipitation Detection Global Virga Precipitation Distribution Derived From Three Spaceborne Radars and Its Contribution to the Fals. *Geophysical Research Letters*, 45. (Cited on pages 85, 96, 97, and 99.)

Welsh, D., Geerts, B., Jing, X., Bergmaier, P. T., Minder, J. R., Steenburgh, W. J., and Campbell, L. S. (2016). Understanding Heavy Lake-Effect Snowfall: The Vertical Structure of Radar Reflectivity in a Deep Snowband over and downwind of Lake Ontario. *Monthly Weather Review*, 144(11):4221–4244. (Cited on pages 65 and 85.)

Welton, E. J., Campbell, J. R., Spinhirne, J. D., and Scott III, V. S. (2001). Global monitoring of clouds and aerosols using a network of micropulse lidar systems. In *Global monitoring of clouds and aerosols using a network of micropulse lidar systems*, volume 4153, pages 150–158. (Cited on page 38.)

Wendisch, M., MacKe, A., Ehrlich, A., LüPkes, C., Mech, M., Chechin, D., Dethloff, K., Velasco, C. B., Bozem, H., BrüCkner, M., Clemen, H. C., Crewell, S., Donth, T., Dupuy, R., Ebell, K., Egerer, U., Engelmann, R., Engler, C., Eppers, O., Gehrmann, M., Gong, X., Gottschalk, M., Gourbeyre, C., Griesche, H., Hartmann, J., Hartmann, M., Heinold, B., Herber, A., Herrmann, H., Heygster, G., Hoor, P., Jafariserajehlou, S., JäKel, E., JäRvinen, E., Jourdan, O., KäStner, U., Kecorius, S., Knudsen, E. M., KöLlner, F., Kretzschmar, J., Lelli, L., Leroy, D., Maturilli, M., Mei, L., Mertes, S., Mioche, G., Neuber, R., Nicolaus, M., Nomokonova, T., Notholt, J., Palm, M., Van Pinxteren, M., Quaas, J., Richter, P., Ruiz-Donoso, E., SchäFer, M., Schmieder, K., Schnaiter, M., Schneider, J.,

SchwarzenböCk, A., Seifert, P., Shupe, M. D., Siebert, H., Spreen, G., Stapf, J., Stratmann, F., Vogl, T., Welti, A., Wex, H., Wiedensohler, A., Zanatta, M., Zeppenfeld, and Sebastian (2019). The arctic cloud puzzle using acloud/pascal multiplatform observations to unravel the role of clouds and aerosol particles in arctic amplification. *Bulletin of the American Meteorological Society*, 100:841–871. (Cited on page 39.)

Westbrook, C. D. (2008). The fall speeds of sub-100 µm ice crystals. *Quarterly Journal of the Royal Meteorological Society*, 134:1243–1251. (Cited on page 71.)

Williams, C. R., White, A. B., Gage, K. S., and Ralph, M. (2007). Vertical Structure of Precipitation and Related Microphysics Observed by NOAA Profilers and TRMM during NAME 2004. *American Meteorological Society*, 20:1693–1712. (Cited on page 22.)

Winker, D. M., Pelon, J., Coakley, J. A., Ackerman, S. A., Charlson, R. J., Colarco, P. R., Flamant, P., Fu, Q., Hoff, R. M., Kittaka, C., Kubar, T. L., Le Treut, H., McCormick, M. P., Mégie, G., Poole, L., Powell, K., Trepte, K., Vaughan, M. A., and Wielicki, B. A. (2010). The Calipso Mission: A Global 3D View of Aerosols and Clouds. *Bulletin of the American Meteorological Society*, 91(9):1211–1229. (Cited on pages 38 and 57.)

Winker, D. M., Vaughan, M. A., Omar, A., Hu, Y., Powell, K. A., Liu, Z., Hunt, W. H., and Young, S. A. (2009). Overview of the CALIPSO mission and CALIOP data processing algorithms. *Journal of Atmospheric and Oceanic Technology*, 26(11):2310–2323. (Cited on page 57.)

Wolfe, J. P. and Snider, J. R. (2012). A relationship between reflectivity and snow rate for a high-altitude s-band radar. *Journal of Applied Meteorology and Climatology*, 51(6):1111–1128. (Cited on page 24.)

Wood, N. B. (2011). *Estimation of snow microphysical properties with application to millimiter-wavelenght radar retrievals for snowfall rate*. PhD thesis, Colorado State University. (Cited on page 5.)

Wood, N. B., L'Ecuyer, T. S., Vane, D. G., Stephens, G. L., and Partain, P. (2013). Level 2C snow profile process description and interface control document, version 0. Technical report, NASA Earth System Science Pathfinder Mission Level. (Cited on page 5.)

Wu, S., Liu, Z., and Liu, B. (2006). Enhancement of lidar backscatters signal-to-noise ratio using empirical mode decomposition method. *Optics Communications*, 267(1):137–144. (Cited on page 43.)

Würzer, S., Jonas, T., Wever, N., and Lehning, M. (2016). Influence of Initial Snowpack Properties on Runoff Formation during Rain-on-Snow Events. *Journal of Hydrometeorology*, 17(6):1801–1815. (Cited on page 2.)

Yang, D., Kane, D., Zhang, Z., Legates, D., and Goodison, B. (2005). Bias corrections of long-term (1973-2004) daily precipitation data over the northern regions. *Geophysical Research Letters*, 32(19):1–5. (Cited on page 2.)

Ye, H., Fetzer, E. J., Wong, S., Behrangi, A., Olsen, E. T., Cohen, J., Lambrigtsen, B. H., and Chen, L. (2014). Supporting Information for Skilful seasonal predictions of Summer European rainfall. *Geophysical Research Letters*, 3:2941–2947. (Cited on page 2.)

Yoshida, R., Okamoto, H., Hagihara, Y., and Ishimoto, H. (2010). Global analysis of cloud phase and ice crystal orientation from Cloud-Aerosol Lidar and Infrared Pathfinder Satellite Observation (CALIPSO) data using attenuated backscattering and depolarization ratio. *Journal of Geophysical Research*, 115:D00H32. (Cited on pages 39, 47, 58, and 104.)

Young, A. T. (1981). Rayleigh scattering. *Applied Optics*, 20(4):533–535. (Cited on page 46.)

List of publications

First-author publications

Durán-Alarcón, C., Boudevillain, B., Genthon, C., Grazioli, J., Souverijns, N., Van Lipzig, N. P. M., Gorodetskaya, I. V. and Berne, A.: The vertical structure of precipitation at two stations in East Antarctica derived from micro rain radars, Cryosphere, doi:10.5194/tc-13-247-2019, 2019.

Durán-Alarcón, C., Gevaert, C. M., Mattar, C., Jiménez-Muñoz, J. C., Pasapera-Gonzales, J. J., Sobrino, J. A., Silvia-Vidal, Y., Fashé-Raymundo, O., Chavez-Espiritu, T. W. and Santillan-Portilla, N.: Recent trends on glacier area retreat over the group of Nevados Caullaraju-Pastoruri (Cordillera Blanca, Peru) using Landsat imagery, J. South Am. Earth Sci., doi:10.1016/j.jsames.2015.01.006, 2015.

Durán-Alarcón, C., Santamaría-Artigas, A., Valenzuela, N. and Mattar, C.: RSR Calculator, a tool for the Calibration / Validation activities, Rev. Teledetec., (42), doi:10.4995/raet.2014.3230, 2014.

Durán-Alarcón, C., Boudevillain, B.,Listowski, C., Simeonov, V., Genthon, C., and Berne, A.: Cloud and precipitation particle classification using lidar, East Antarctica, Atmospheric Measurement Techniques, (To be submitted).

Co-author publications

Lemonnier, F., Madeleine, J. B., Claud, C., Genthon, C., **Durán-Alarcón, C.**, Palerme, C., Berne, A., Souverijns, N., Van Lipzig, N., Gorodetskaya, I. V., L'Ecuyer, T. and Wood, N.: Evaluation of CloudSat snowfall rate profiles by a comparison with in situ micro-rain radar observations in East Antarctica, Cryosphere,

doi:10.5194/tc-13-943-2019, 2019.

Retamales-Muñoz, G., **Durán-Alarcón, C.** and Mattar, C.: Recent land surface temperature patterns in Antarctica using satellite and reanalysis data, J. South Am. Earth Sci., doi:10.1016/j.jsames.2019.102304, 2019.

Souverijns, N., Gossart, A., Lhermitte, S., Gorodetskaya, I. V., Grazioli, J., Berne, A., **Durán-Alarcón, C.**, Boudevillain, B., Genthon, C., Scarchilli, C. and Van Lipzig, N. P. M.: Evaluation of the CloudSat surface snowfall product over Antarctica using ground-based precipitation radars, Cryosphere, doi:10.5194/tc-12-3775-2018, 2018.

Genthon, C., Berne, A., Grazioli, J., **Durán-Alarcón, C.**, Praz, C. and Boudevillain, B.: Precipitation at Dumont d'Urville, Adélie Land, East Antarctica: The APRES3 field campaigns dataset, Earth Syst. Sci. Data, doi:10.5194/essd-10-1605-2018, 2018.

Grazioli, J., Genthon, C., Boudevillain, B., **Durán-Alarcón, C.**, Del Guasta, M., Madeleine, J. and Berne, A.: Measurements of precipitation in Dumont d'Urville, Adélie Land, East Antarctica, Cryosphere, 11(4), 1797–1811, doi:10.5194/tc-11-1797-2017, 2017.

Rivera, C., Mattar, C. and **Durán-Alarcón, C.**: Trend in vegetational cover affected by fire in the Torres del Paine National Park, Rev. Teledetec., 2017(50), doi:10.4995/raet.2017.7422, 2017.

Olivera-Guerra, L., Mattar, C., Merlin, O., **Durán-Alarcón, C.**, Santamaría-Artigas, A. and Fuster, R.: An operational method for the disaggregation of land surface temperature to estimate actual evapotranspiration in the arid region of Chile, ISPRS J. Photogramm. Remote Sens., doi:10.1016/j.isprsjprs.2017.03.014, 2017.

Mattar, C., Santamaría-Artigas, A., **Durán-Alarcón, C.**, Olivera-Guerra, L., Fuster, R. and Borvarán, D.: The LAB-Net Soil Moisture Network: Application to Thermal Remote Sensing and Surface Energy Balance, Data, doi:10.3390/data1010006, 2016.

Mattar, C., **Durán-Alarcón, C.**, Jiménez-Muñoz, J. C., Santamaría-Artigas, A., Olivera-Guerra, L. and Sobrino, J. A.: Global Atmospheric Profiles from Reanalysis Information (GAPRI): a new database for Earth surface temperature retrieval, Int.

J. Remote Sens., 36(19–20), 5045–5060, doi:10.1080/01431161.2015.1054965, 2015.

Mattar, C., Hernández, J., Santamaría-Artigas, A., **Durán-Alarcón, C.**, Olivera-Guerra, L., Inzunza, M., Tapia, D. and Escobar-lavín, E.: A first in-flight absolute calibration of the Chilean Earth Observation Satellite, ISPRS J. Photogramm. Remote Sens., doi:10.1016/j.isprsjprs.2014.02.017, 2014.

Santamaría-Artigas, A., Mattar, C., **Durán-Alarcón, C.**, Olivera, L., Inzunza, M., Tapia, D. and Escobar-Lavín, E.: First application of FASAT-Charlie Imagery for the assessment of semiarid prairies in Chile, Rev. Teledetec., (40), 2013.

Mattar, C., Santamaría-Artigas, A. and **Durán-Alarcón, C.**: Estimating the burned area of the Torres del Paine National Park using remote sensing data, Rev. Teledetec., (38), 2012.

Datasets

Durán-Alarcón, C., Boudevillain, B., Genthon, C., Grazioli, J.; Berne, A.: Effective reflectivity, vertical velocity, spectral width and snowfall rate estimates derived from a micro rain radar (MRR) at the Dumont d'Urville station, Adelie Land, East Antarctica. PANGAEA, https://doi.org/10.1594/PANGAEA.897614, 2019.

Mattar, C., Santamaría-Artigas, A., **Durán-Alarcón, C.**, Olivera-Guerra, L and Fuster, R.: LAB-net the First Chilean soil moisture network for Remote Sensing Applications. International Soil Moisture Network (ISMN), https://ismn.geo.tuwien.ac.at/en/sites/networks/LAB-net/, 2014.